Energy Efficient Driving and Charging Decisions in a Connected and Automated Plug-In Hybrid Electric Vehicle

Thesis

Presented in Partial Fulfillment of the Requirements for the Degree Master of Science in the Graduate School of The Ohio State University

By

Karinne Rose Bernanke

Graduate Program in Mechanical Engineering

The Ohio State University

2023

Thesis Committee

Dr. Stephanie Stockar, Advisor

Dr. Marcello Canova

Abstract

Global vehicle emission regulations along with a growing consumer demand is a driving force in shifting the automotive industry towards a cleaner future. This shift requires significant automotive advancements in energy efficiency. Powertrain electrification and connected and autonomous vehicle (CAV) technology are key innovations that can reduce energy consumption and emissions.

This thesis aims to improve the energy efficiency of a vehicle under varying conditions and determine the effect of charging on energy consumption. The vehicle model is established and utilized in the formulation of an optimal control problem in order to minimize energy consumption. The developed method to solve the optimization problem is applied in a large-scale study, culminating in an analysis of the effects of varying charging behavior on the energy consumption of the vehicle.

The vehicle model is developed and validated over 25 real-world cycles resulting in an average fuel consumption, battery energy consumption, and total energy consumption errors of 2.2%, 2.9%, and 2.8%, respectively. The velocity dynamics and powertrain of the modeled vehicle are co-optimized to improve a weighted cost between energy consumption and travel time. The optimization results in an average decrease of 10% in fuel consumption, 8% in battery energy consumption, and 19% in total energy consumption. Lastly, the large-scale study reveals a correlation between charging behavior and both the effect of charging event placement and the presence of look-ahead information on energy efficiency. The resulting trends in charging behavior give context for energy efficient trip planning.

To my sister

Acknowledgments

I would like to express my sincere gratitude to my advisor, Dr. Stephanie Stockar for her guidance and motivation to develop the work in this thesis. Her constant encouragement has played a key role in my professional growth as a researcher. I am also grateful to Dr. Marcello Canova who has provided many insights into my research and has greatly contributed to this work. Additionally, thank you to Dr. Giorgio Rizzoni, director of the Center for Automotive Research (CAR), for his support throughout my master’s program.

I am fortunate to have been mentored by Dr. Shobhit Gupta who has taught me so much in the field of modeling and controls. I will forever be grateful for his unwavering confidence in me and his ability to make me feel heard and valued. I would additionally like to thank the NEXTCAR team for their assistance and expertise in completing this thesis. In particular, thank you to Stefano D’Alessandro whose collaboration made this thesis possible. His kindness and thoughtfulness were incredibly appreciated throughout my time in this program.

Finally, I would like to thank my friends and family for being my biggest supporters through my highs and lows while conducting this research. I have leaned heavily on my

support system during this time, and I cannot express how thankful I am for their love, encouragement, and assurance.

Vita

June 24, 1999…………………………………	Born in Charlotte, North Carolina, United States
2021………………………………………..	B.S. Mechanical Engineering, Georgia Institute of Technology, Atlanta, Georgia, United States

Fields of Study

Major Field: Mechanical Engineering

Table of Contents

Abstract ii

Acknowledgments v

Vita vii

Table of Contents viii

List of Tables xii

List of Figures xiii

Chapter 1 Introduction 1

1.1 Motivation 1

1.1.1 The ARPA-E NEXTCAR Program 5

1.2 Optimization of Plug-In Hybrid Electric Vehicles 7

1.2.1 Vehicle Dynamics and Powertrain Optimization of a PHEV 7

1.2.2 Optimal Control Problem (OCP) Formulation and Solution Methods 8

1.2.3 Dynamic Programming 10

1.3 Availability of Charging 11

1.4 Contributions of this Work 13

Chapter 2 Vehicle Model Development Validation 15

2.1 Overview of the Vehicle 15

2.2 Vehicle Energy Simulation Model 18

2.2.1 Overview of the Model 18

2.2.2 Engine 19

2.2.3 Battery Pack 20

2.2.4 Electric Machines 21

2.2.5 Transmission and Final Drive 23

2.2.6 Longitudinal Vehicle Dynamics 26

2.3 Experimental Testing and Data Analysis 28

2.3.1 Vehicle Instrumentation 28

2.3.2 Data Acquisition 28

2.3.3 Vehicle Testing 29

2.3.4 Experimental Results 32

2.4 Model Calibration / Validation 37

2.4.1 Power Limitations 37

        2.4.2 Engine 51
    2.5 Vehicle Simulator Validation 55
    2.6 Conclusion 64
Chapter 3 Vehicle Dynamics and Powertrain Optimization for a Plug-In HEV 66
    3.1 Optimal Control Problem... 66
        3.1.1 Problem Formulation 66
        3.1.2 Discrete State Dynamics 68
    3.2 Solution Approach 73
    3.3 Route Results 74
    3.4 Conclusion 88
Chapter 4 Effect of Charging Behavior on Energy Consumption Study.......................... 89
    4.1 Introduction.. 89
    4.2 Study Framework... 90
        4.2.1 Representative Route Creation 91
        4.2.2 Charging Variation Approach.. 97
    4.3 Simulation Setup and Outputs 100
    4.4 Preliminary Simulation Results 101
Chapter 5 . Evaluating the Effect of Charging Behavior on Energy Consumption........ 107

5.1 Definition of Metrics 107

5.2 Case Study 108

5.3 Results 109

Chapter 6 Conclusion and Future Work 130

6.1 Conclusion 130

6.2 Future Work 131

Bibliography 133

Appendix A: Simulation Campaign Results 149

Appendix B: Large Scale Extended Study Results 154

List of Tables

Table 2.1: Summary of Vehicle Operation Modes 17

Table 2.2: Metrics for Regulatory Drive Cycles... 35

Table 2.3: Metrics for Real-World Drive Cycles.. 36

Table 2.4: Vehicle Simulator Validation for All Experimental Real-World Routes........ 63

Table 3.1. Summary of the cumulative cost for the three different SoCs analyzed for three different weighting factors. 85

Table 3.2: Comparison of DP Solution vs Experimental.. 87

Table 4.1: Representative Weekly Driving Schedule 92

Table 4.2: Probability of Charging Events per Location 98

Table 4.3: Sample Week Results Summary.. 106

Table A.1: Variation 83 Summary.. 151

Table A.2: Variation 22 Summary.. 153

List of Figures

Figure 1.1 US Emissions Statistics for the Transportation Sector in the US, 2020 [6] 2

Figure 1.2: Final Footprint – Based CO2 Equivalent Standards for Cars [10] 3

Figure 1.3 Planned and Operational Connected Vehicle Deployments [26] 5

Figure 1.4: Share of charging events by location and vehicle usage for PHEVs [60] 12

Figure 2.1: 2017 Chrysler Pacifica PHEV 15

Figure 2.2: Chrysler Pacifica Powertrain Model 17

Figure 2.3: Block Diagram of the Powertrain and Vehicle Dynamics Model 19

Figure 2.4: Engine Fuel Consumption Map as a Function of Engine Speed and Torque. 20

Figure 2.5: Zeroth Order Equivalent Circuit Model 20

Figure 2.6: Battery Model Input/Output Structure 21

Figure 2.7: Electric Machines Model Input/Output Structure 22

Figure 2.8: (a) Transmission and Final Drive Model Input/Output Structure, (b) Planetary Gear Set Model [74] 23

Figure 2.9: Longitudinal Vehicle Dynamics Model Input/Output Structure 27

Figure 2.10: Installation of the MABX-III connection to CAN 28

Figure 2.11: Instrumentation Setup with MABX-III used for Data Acquisition 29

Figure 2.12: Regulatory Drive Cycles: (a) FTP Cycle, (b) Modified MCT Cycle 30

Figure 2.13: Speed Limit of Real-World Routes: (a) Route 19, (b) Mixed Route 1, (c) Mixed Route 4 31

Figure 2.14: Evolution of vehicle velocity, requested torque, pedal positions, and SoC over the modified MCT Cycle 34

Figure 2.15: Experimental Inputs into the Vehicle Simulator for Calibration using the MCT Cycle: (a) Motor Torques, (b) Engine Speed, (c) Brake Force, (d) Auxiliary Power 38

Figure 2.16: Comparison of Actual vs Predicted SoC: (a) Comparison of the Signals, (b) Correlation of the Signals, (c) Error Distribution 39

Figure 2.17: Comparison of Actual vs Predicted Battery Current: (a) Comparison of the Signals, (b) Correlation of the Signals, (c) Error Distribution 40

Figure 2.18: Comparison of Actual vs Predicted Battery Voltage: (a) Comparison of the Signals, (b) Correlation of the Signals, (c) Error Distribution 41

Figure 2.19: Comparison of Actual vs Predicted Electrical Power Demands 42

Figure 2.20: Comparison of Actual vs Predicted Motor Power: (a) MGA Electrical Power Demanded (b) MGB Electrical Power Demanded 43

Figure 2.21: Comparison of Actual vs Calibrated Battery SoC: (a) Comparison of the Signals, (b) Correlation of the Signals, (c) Error Distribution 45

Figure 2.22: Comparison of Actual vs Calibrated Battery Current: (a) Comparison of the Signals, (b) Correlation of the Signals, (c) Error Distribution 46

Figure 2.23: Comparison of Actual vs Calibrated Battery Voltage: (a) Comparison of the Signals, (b) Correlation of the Signals, (c) Error Distribution 47

Figure 2.24: Experimental Inputs into the Vehicle Simulator for Validation using the Mixed Route 4 Cycle: (a) Motor Torques, (b) Engine Speed, (c) Brake Force, (d) Auxiliary Power 48

Figure 2.25: Comparison of Actual vs Calibrated Battery SoC for Validation: (a) Comparison of the Signals, (b) Correlation of the Signals, (c) Error Distribution 49

Figure 2.26: Comparison of Actual vs Calibrated Battery Current for Validation: (a) Comparison of the Signals, (b) Correlation of the Signals, (c) Error Distribution 50

Figure 2.27: Comparison of Actual vs Calibrated Battery Voltage for Validation: (a) Comparison of the Signals, (b) Correlation of the Signals, (c) Error Distribution 51

Figure 2.28: Comparison of Actual vs Predicted Fuel Consumption: (a) Comparison of the Signals, (b) Correlation of the Signals, (c) Error Distribution, (d) Comparison of Cumulative Consumption 52

Figure 2.29: Comparison of Actual vs Calibrated Fuel Consumption: (a) Comparison of the Signals, (b) Correlation of the Signals, (c) Error Distribution, (d) Comparison of Cumulative Consumption 53

Figure 2.30: Comparison of Actual vs Calibrated Fuel Consumption for Validation on the MCT Cycle: (a) Comparison of the Signals, (b) Correlation of the Signals, (c) Error Distribution, (d) Comparison of Cumulative Consumption 54

Figure 2.31: Updated Vehicle Simulator Block Diagram 55

Figure 2.32: Experimental Inputs into the Vehicle Simulator for Validation using the Route 19 Cycle: (a) Motor Torques, (b) Engine Speed, (c) Brake Force, (d) Auxiliary Power 56

Figure 2.33: Comparison of Actual vs Modeled Battery SoC for Validation: (a) Comparison of the Signals, (b) Correlation of the Signals, (c) Error Distribution 57

Figure 2.34: Comparison of Actual vs Modeled Battery Current for Validation: (a) Comparison of the Signals, (b) Correlation of the Signals, (c) Error Distribution 58

Figure 2.35: Comparison of Actual vs Modeled Battery Voltage for Validation: (a) Comparison of the Signals, (b) Correlation of the Signals, (c) Error Distribution 59

Figure 2.36: Comparison of Actual vs Modeled Fuel Consumption for Validation: (a) Comparison of the Signals, (b) Correlation of the Signals, (c) Error Distribution, (d) Comparison of Cumulative Consumption 60

Figure 2.37: Comparison of Actual vs Modeled Vehicle Velocity for Validation: (a) Comparison of the Signals, (b) Correlation of the Signals, (c) Error Distribution 61

Figure 3.1: Engine OOL Illustration on the Engine Fuel Consumption Map 71

Figure 3.2: The Optimal MGA Torque Map 72

Figure 3.3: Battery State of Charge and Vehicle Velocity in Charge Depleting Strategy for an Aggressive, Normal, and Relaxed Driver. 75

Figure 3.4: MGA conditions for an aggressive, normal, and relaxed driver for charge depleting conditions (a) MGA speed and torque plots (b) MGA operational points on the efficiency map 76

Figure 3.5: MGB conditions for an aggressive, normal, and relaxed driver for charge depleting conditions (a) MGB speed and torque plots (b) MGB operational points on the efficiency map. 76

Figure 3.6: ICE conditions for an aggressive, normal, and relaxed driver for charge depleting conditions (a) ICE speed and torque plots (b) ICE operational points on the efficiency map. 77

Figure 3.7: Pareto front of the DP results comparing the travel time vs energy consumed for weighting factors $\gamma = 0.1$ to 0.9 for four different initial SoC's in CD strategy 78

Figure 3.8: Battery State of Charge and Vehicle Velocity in CD-CS Strategy for an Aggressive, Normal, and Relaxed Driver. 79

Figure 3.9: MGA conditions for an aggressive, normal, and relaxed driver for CD-CS conditions (a) MGA speed and torque plots (b) MGA operational points on the efficiency map. 79

Figure 3.10: MGB conditions for an aggressive, normal, and relaxed driver for CD-CS conditions (a) MGB speed and torque plots (b) MGB operational points on the efficiency map. 80

Figure 3.11: ICE conditions for an aggressive, normal, and relaxed driver for CD-CS conditions (a) ICE speed and torque plots (b) ICE operational points on the efficiency map. 80

Figure 3.12: Pareto front of the DP results comparing the travel time vs energy consumed for weighting factors $\gamma = 0.1$ to 0.9 for three different initial SoC's in CD-CS strategy. 81

Figure 3.13: Battery State of Charge and Vehicle Velocity in CS Strategy for an Aggressive, Normal, and Relaxed Driver. 82

Figure 3.14: MGA conditions for an aggressive, normal, and relaxed driver for CS conditions (a) MGA speed and torque plots (b) MGA operational points on the efficiency map. 82

Figure 3.15: MGB conditions for an aggressive, normal, and relaxed driver for CS conditions (a) MGB speed and torque plots (b) MGB operational points on the efficiency map. 83

Figure 3.16: ICE conditions for an aggressive, normal, and relaxed driver for CS conditions (a) ICE speed and torque plots (b) ICE operational points on the efficiency map. 83

Figure 3.17: Pareto front of the DP results comparing the travel time vs fuel consumed for weighting factors $\gamma = 0.1$ to 0.9 for four different initial SoC's spanning all strategies. 84

Figure 4.1: Representative Driving Schedule 90

Figure 4.2: Map of Weekly Routes: (a) Home to Work, (b) Home to Hardware Store, (c) Home to Event, (d) Work to Lunch, (e) Work to Physical Therapy, (f) Home to Gym, (g) Home to Park, (h) Home to Grocery Store, (i) Home to Pharmacy [88] 93

Figure 4.3: Home to Work Route Features 97

Figure 4.4: Sample Week Results Plot 102

Figure 4.5: Enlarged Portion of Sample Results 104

Figure 5.1: Weekly Energy Consumption 111

Figure 5.2: Weekly Energy Savings 112

Figure 5.3: Weekly Battery Energy Consumption 113

Figure 5.4: Weekly Fuel Consumption 114

Figure 5.5: MPG of the Week Variations 116

Figure 5.6: MPGe of the Week Variations 117

Figure 5.7: Extended Weekly Energy Consumption 119

Figure 5.8: Extended Weekly Energy Savings 120

Figure 5.9: Extended Weekly MPGe 122

Figure 5.10: Extended MPGe Gain 123

Figure 5.11: Distance Between Charges with MPGe 124

Figure 5.12: Utility Factor 126

Figure 5.13: Effect of Charging Allocation on the Utility Factor 127

Figure A.1: Variation 83 Results 150

Figure A.2: Variation 22 Results 152

Figure B.1: Weekly Battery Energy Consumption 155

Figure B.2: Weekly Fuel Consumption 156

Figure B.3: Effect of Charging Allocation on the Utility Factor 158

Chapter 1 Introduction

1.1 Motivation

The transportation sector generates the largest share of greenhouse gases (GHG) accounting for approximately one quarter of global greenhouse gas emissions [1]-[3]. According to the United States (US) Environmental Protection Agency (EPA), over half of transportation emissions come from light duty vehicles (LDV), such as passenger cars, light trucks, and motorcycles (57% as of 2020 shown in Figure 1.1). Ownership of LDVs is expected to double in the next few decades due to an increased demand for mobility related to population growth and changes in demographics [4]. An increase in mobility can be positively correlated with the combined number of miles driven and fuel consumed which can, in turn, lead to increased GHG emissions [4]. This is true historically as the transportation sector experienced the highest increase in GHG emissions than any other sector from 1990-2020 when mobility demand increased drastically [5]. To meet this demand, the need for more fuel-efficient mobility solutions to lessen GHG emissions in the transportation sector is increasingly important [4].

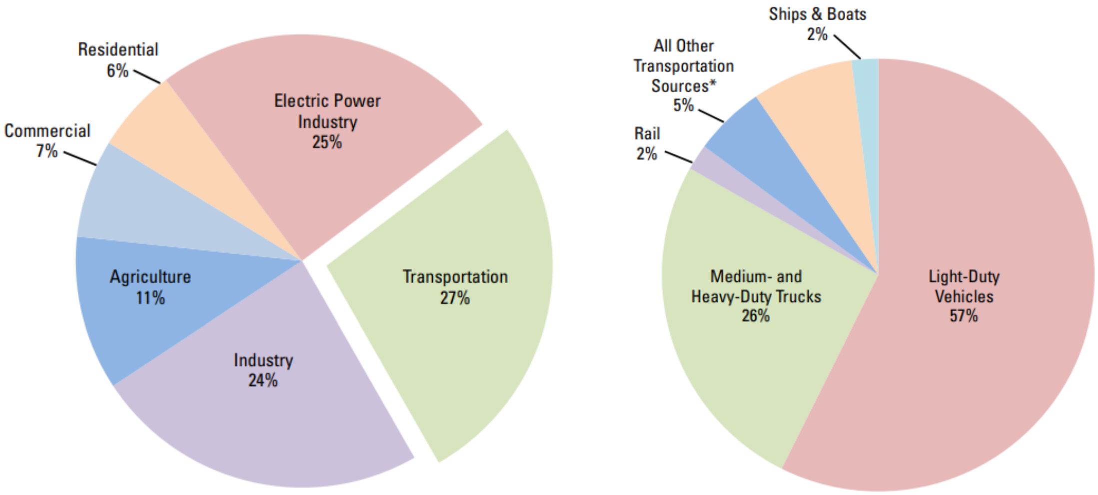

(a) Share of US GHG Emissions by Economic Sector

(b) Share of US Transportation Sector GHG Emissions by Source

Figure 1.1 US Emissions Statistics for the Transportation Sector in the US, 2020 [6]

In order to limit the effect of the transportation sector on climate change, the Corporate Average Fuel Economy (CAFE) standards were established in 1975 [7]. These standards require automakers to achieve a yearly guideline average fuel economy aimed at reducing fuel consumption, promoting technological advancements in the automotive and energy sectors, and lowering GHG emissions [7].

Regulated by the EPA and the National Highway Traffic and Safety Administration (NHTSA), the most recent CAFE standard finalized on March 31, 2022, requires a fleet average of approximately 49 miles per gallon (MPG) by 2026, which mandates a 26% increase in fuel efficiency in the next three years (Figure 1.2) [8]. In 2021, President Biden set a goal for zero emission vehicles (ZEVs) to comprise 50% of all new LDV sales in the US by 2030 [9]. This goal was part of his executive order titled "Strengthening American Leadership in Clean Cars and Trucks" and defined ZEVs as battery electric vehicles (BEVs), plug-in hybrid electric vehicles (PHEVs), or fuel cell electric vehicles (FCEVs) [9]. These policies promote technological advancements in the automotive industry primarily related to the vehicle powertrain, focusing on improving the performance of the internal combustion engine and moving toward the development of increased levels of electrification.

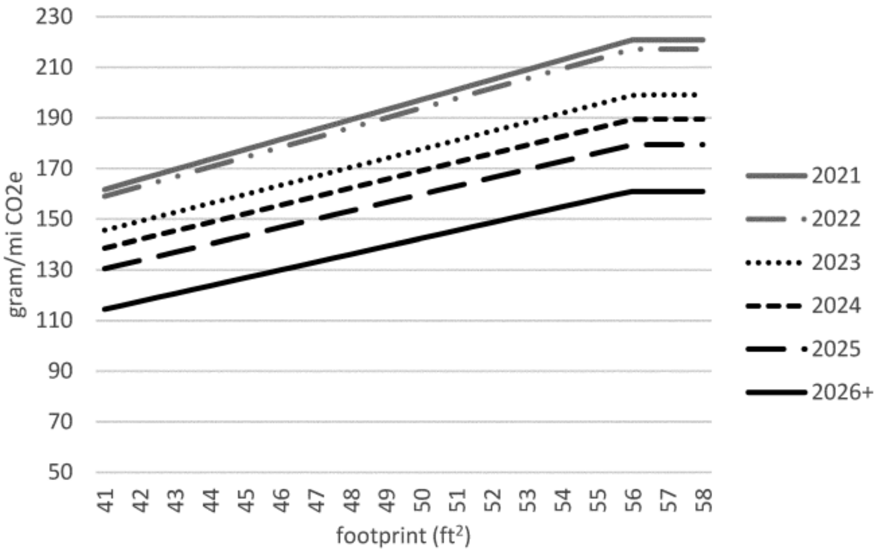

Figure 1.2: Final Footprint – Based CO2 Equivalent Standards for Cars [10]

To meet the stringent regulations, automotive industries are improving the energy efficiency of future automobiles by developing technologies such as hybrid and electric powertrain development, and vehicle connectivity and automation [11]-[13]. Powertrain electrification is a key enabler in reducing GHG emissions and shifting away from a reliance on fuel as the sole energy source used to power a vehicle [14]. The incorporation of a battery in the powertrain provides electrical energy to contribute to the vehicle operation, enabling a downsizing of the engine [15]. A decreased power demanded from the engine leads to a reduction in fuel consumption and GHG emissions as compared to a conventional vehicle [11].

Connected vehicles use communication technologies to exchange information with other vehicles (V2V), infrastructure (V2I), or both (V2X) [16]. Autonomous vehicles can range from the implementation of driver assistance technologies where the vehicle can control either speed or steering (Level 1) to a vehicle that can drive itself in any condition (Level 5) [17]. Fully automated vehicles can control the vehicle movement and view immediate surroundings while connectivity provides information about the future. Together, CAVs can reduce traffic congestion through V2V coordination and controlling the vehicle speed [13]. Moreover, V2I coordination provides traffic light information so an automated vehicle may correct the vehicle speed to avoid red lights [13]. Reducing traffic congestion and time at a stop light are two examples that decrease vehicle idling, which emits GHG and increases an individual vehicle’s fuel consumption [18]. Other benefits of CAV technology include an increase in road safety, a smoother riding experience, and increased accessibility for people not able to drive [18]-[20].

Some automotive companies have already integrated partially connected and autonomous technologies on their products such as assistive parking, cruise control, emergency braking, and sensor usage [21], [22]. Specifically, the implementation of electronic stability control (ESC) has been required by the NHTSA since 2012 and more regulations on connected technologies are expected in the coming years [23]. It is predicted that Level 5 autonomous vehicles will become available in the 2030s and will comprise around 50% of all vehicle sales by the 2050s [24]. Research around CAVs is growing with many ongoing studies of CAVs conducted on the roads today, shown in Figure 1.3 [25].

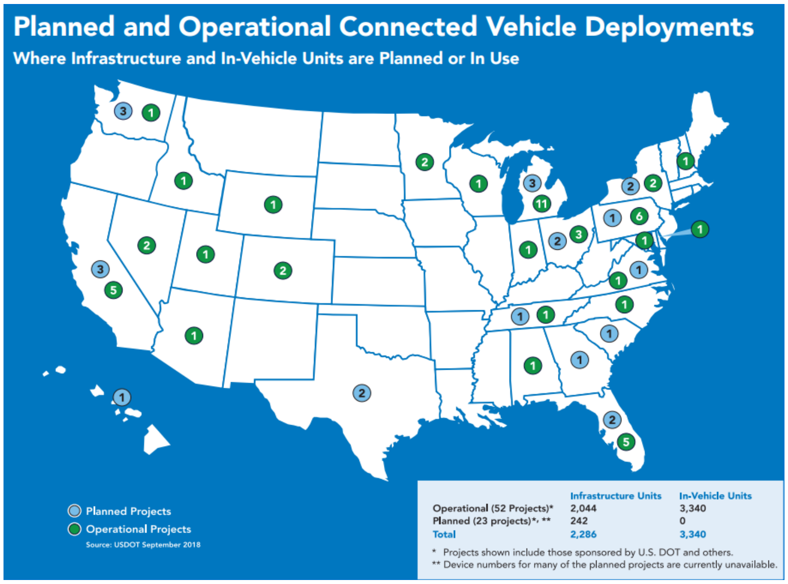

	Infrastructure Units	In-Vehicle Units
Operational (52 Projects)*	2,044	3,340
Planned (23 projects)*, **	242	0
Total	2,286	3,340

* Projects shown include those sponsored by U.S. DOT and others.
** Device numbers for many of the planned projects are currently unavailable.

Figure 1.3 Planned and Operational Connected Vehicle Deployments [26]

1.1.1 The ARPA-E NEXTCAR Program

To contribute to the research in CAV technology, the Next Generation Energy Technologies for Connected and Automated On-Road Vehicles (NEXTCAR) project was initiated in 2016 by ARPA-E (Advanced Research Projects Agency – Energy) [27]. The aim of the NEXTCAR program is to enable the development of vehicle dynamics and powertrain control (VD&PT) technologies by leveraging emerging CAV innovations to improve the energy efficiency of vehicles in real world driving conditions. Phase I of the NEXTCAR program ran from 2016 – 2020 with the goal of reducing the energy consumption of a Level 1 vehicle by 20%. Phase II of the NEXTCAR program spans 2021 – 2024 with the goal of reducing energy consumption of a Level 4 (able to drive itself under most conditions) light duty vehicle by 30% against a Level 0 (no automation) baseline.

The NEXTCAR program is one of the first to consider energy efficiency in CAV applications, focusing on technology that can reduce emissions across the transportation sector [28]. The work done in this thesis provides a baseline model of the vehicle and a preliminary technique to contribute to the 30% energy efficiency improvement. The baseline model predicts the operation of the commercial vehicle and outlines the interconnections within the powertrain. Understanding the vehicle model aids in the development of an algorithm to solve for the optimal vehicle operation over a deterministic route to maximize energy efficiency. The solutions to this algorithm provide a foundation upon which to continue improving the energy efficiency with stochastic routes in real-time. Further, the relationship between energy efficiency and charging behavior is analyzed to identify trends that can decrease energy consumption.

1.2 Optimization of Plug-In Hybrid Electric Vehicles

Connectivity advancements have enabled vehicles to receive information about future driving conditions, like traffic light patterns, speed limits, road grade, and potential upcoming hazards [29]. This situational awareness combined with the ability to control the vehicle using vehicle automation enables CAVs to act upon and predict upcoming events with higher probability than if a human driver were in control [30].

1.2.1 Vehicle Dynamics and Powertrain Optimization of a PHEV

PHEVs utilize one or more electric machines in combination with an on-board internal combustion engine (ICE) to propel the vehicle. The ability to charge from an external power source allows the PHEV to have an all-electric capability similar to an EV and to use the ICE as a range extender. With multiple energy reserves stored in the vehicle, the controller determines how much power is provided from each source, called the power split. The power split determines the speed and torque of the ICE and electric machines. The co-optimization of VD&PT optimizes both the velocity trajectory and the power split of the vehicle and has become the focus of some recent works [31]-[35]. Powertrain optimization refers to finding an optimal power flow for the vehicle to operate over a deterministic velocity trajectory [36]. Vehicle dynamics optimization refers to finding an optimal vehicle velocity trajectory given route characteristics such as the speed limit [36]. VD&PT optimization is unique in that it harnesses the additional levels of control that connectivity, automation, and electrification provide in the controller. Considering these variables introduces a higher computation complexity, therefore the formulation of the optimal control problem to suitably co-optimize the vehicle velocity and torque split is crucial [37].

1.2.2 Optimal Control Problem (OCP) Formulation and Solution Methods

The VD&PT OCP for a PHEV is most commonly formulated as a sequential trajectory optimization problem to minimize energy usage [38]. This means the problem is formulated in stages, first solving the velocity dynamics optimization problem then the powertrain optimization problem in a hierarchical structure [39], [40]. As the vehicle dynamics optimization is solved first, the powertrain dynamics are not explicitly considered in the resulting velocity trajectory [41]. Therefore, the velocity trajectory produced in a decentralized method may not result in the lowest energy consumption [41]. Though less common, a centralized solution that solves VD&PT at the same level has been shown to enhance the controls performance in terms of robustness and system-wide efficiency that is comparable to a decentralized method [36], [41]. A study performed in [42] compared both centralized and decentralized methods, reporting that the centralized method used less energy than the decentralized method by 0.19% - 21.62%, depending on the characteristics of the route tested. An instance of when the centralized method is beneficial is if the energy consumption objective for the powertrain controls can be minimized by operating in EV mode. With the incentive to deplete the battery, using the centralized method can result in a more relaxed driving style with less acceleration in order to use less fuel [36]. Thus, this thesis utilizes the centralized method to formulate the problem as a multi-objective trajectory optimization OCP.

There are various methodologies available to solve the OCP for a specific vehicle architecture. Some of these methodologies include dynamic programming (DP) [39], Pontryagin's minimum principle (PMP) [42], equivalent consumption minimization strategy (ECMS) [43], rule-based strategy (RB) [44], model predictive control (MPC) [45], and particle swarm optimization (PSO) [38]. Each methodology has its own advantages and disadvantages, and the choice of methodology depends on the specific requirements and constraints of the problem. For example, DP is computationally intensive but provides an optimal solution, while PMP is less computationally intensive but provides a suboptimal solution. The selection of the methodology should be made based on the trade-off between computational cost and solution quality. Optimization-based methods (i.e. DP, PMP, ECMS) are rooted in optimal control theory and show improved energy savings and flexibility for model extension as compared to heuristic methods [46]. DP is a frequently used tool in literature known for its versatility and robustness against nonlinearity [46]. DP is guaranteed to find the global optimal solution yet is computationally expensive [47]. PMP finds a solution based on a set of conditions of optimality. This method is less expensive than DP yet does not guarantee a global optimal solution [47]. ECMS also uses optimality conditions and has been shown to be intrinsically equivalent to PMP [47]. In this thesis, DP is utilized to find a global optimal numerical solution to the centralized VD&PT co-optimization problem.

1.2.3 Dynamic Programming

DP is an optimization algorithm developed by Dr. Richard Bellman in the 1950s based on Bellman's Principle of Optimality. This principle considers a problem framed as a Markov Decision Process (MDP) which models a decision maker navigating through a dynamic system [48], [49]. At each point in time, the decision maker chooses an action from a set of available actions to take. The decision maker then moves to the next state determined by the chosen action, and receives an immediate cost associated with performing that action. The objective is for the decision maker to choose the optimal sequence of actions, called the optimal policy, to minimize the total cost [50].

Considering an MDP, Bellman's Principle of Optimality can be described:

> Suppose the optimal solution for a problem passes through an intermediate point (x_1, t_1), then the optimal solution to the same problem starting at (x_1, t_1) must be the continuation of the same path [51].

Namely, if an optimal solution from point A to point C goes through point B, the optimal solution starting at point B to point C will follow the same path.

Leveraging this concept, DP solves the MDP by starting at the end of the problem horizon and proceeding backwards [49], [52]-[54]. At each step, the best action to perform is selected from a set of available actions for each state of the system [55]. The technique operates with the assumption that the current state of the system is always known and can accurately predict the next state of the system based on the action taken in the current state. The backwards recursive nature of DP requires a priori knowledge of the MDP, which ensures the algorithm finds the global optimum [56], [57].

1.3 Availability of Charging

The optimal power split and vehicle velocity trajectory solution to the VD&PT problem for PHEVs is reliant upon the AER of the vehicle which can vary based on the battery state of charge (SoC). The initial battery SoC depends on whether the vehicle was charged before the route, indicative of charging behavior. Hence for a similar route and driving behavior, a fully charged battery has more energy stored than a partially charged battery and can therefore use less fuel in the route [58]. It can thus be extrapolated that charging behavior affects the energy consumption of a vehicle, yet this connection has not been explored in literature. In this thesis, different charging behaviors are tested utilizing the OCP formulation for the VD&PT problem to determine the effect on energy consumption.

The charging behavior of an individual is linked to a tendency for PHEV drivers to willingly endure extra costs and time of charging to avoid using gasoline, defined as gas anxiety. Many factors contribute to gas anxiety such as the cost of gasoline, the size of the battery in the vehicle, and the AER that can be obtained by plugging in [59]-[62]. Further, large-scale studies have been conducted to collect general trends in charging behavior [63]-[69]. With the increased availability of charging infrastructure, home and work were found as the most dominant charging locations among all types of LDV ownership, shown in Figure 1.4.

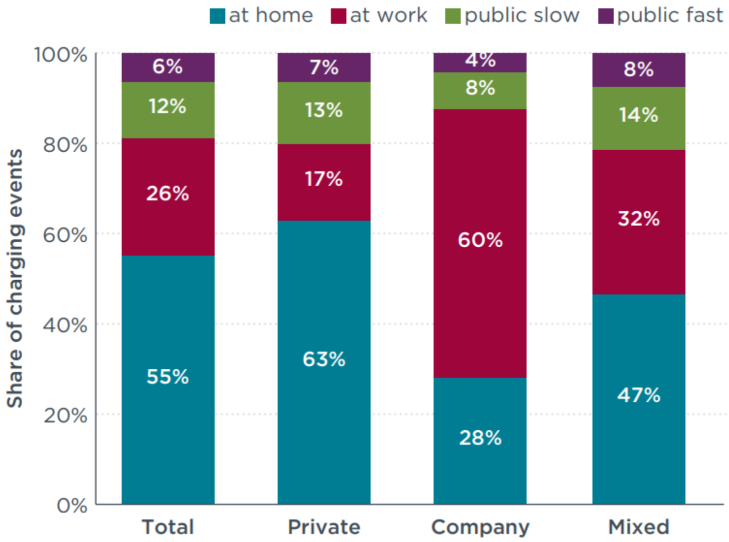

Figure 1.4: Share of charging events by location and vehicle usage for PHEVs [60]

In [64], a study of 166 PHEVs found that the number of charging events per day varies immensely for different models, heavily influenced by the size of the battery along with the factors affecting gas anxiety. As the behavior of the population can differ from frequent charging to rare charging, the number of daily charging events found in literature ranged from 0.14 to 1.43 events per day (1 to 10 charges per week) [63]-[67].

1.4 Contributions of this Work

Although there is a wide variety of literature devoted to energy management in PHEVs, the co-optimization of VD&PT in PHEVs still has much to be explored. The configuration of the PHEV and the chosen objective for minimization requires specific formulation of the OCP. Additionally, the effect of charging behavior on the optimal control solution has yet to be investigated. The intersection of behavior studies and optimal controls allows for the exploration of optimal behavior patterns and their effect on energy efficiency.

The contributions of this thesis are as follows:

- **The development of a model for a power split PHEV minivan:** An energy-based model of a power split PHEV architecture was developed and validated against experimental data. The modeling accuracy was found to be within a maximum of error of 5% for fuel consumption and 6% in battery energy consumption. This translates to an average fuel consumption error of 2.2% and an average battery energy consumption error of 2.9% over 25 routes.
- **Formulation and implementation of the optimal control problem to co-optimize vehicle dynamics and powertrain controls:** Assuming a priori knowledge of the route, a deterministic optimal control problem was formulated with the objective of minimizing the vehicle energy consumption, while keeping the same travel time. In this study, energy consumption is defined as a weighted

average between fuel and electricity allowing for a global minimization of total energy consumed by the vehicle.

- **The evaluation of charging behavior on energy consumption:** a large-scale study was performed to analyze the effects of different charging behaviors on the energy efficiency of a PHEV. Representative weekly routes have been constructed considering both urban and sub-urban routes, as well as the variability in signal phase and timing and the availability of charging. The effect of charging frequency and the knowledge of charge availability on the vehicle energy usage have been quantified by solving the optimal control problem for the representative routes. Overall, the study results reveal links between energy efficiency metrics and different charging behaviors that can be used as a guide for energy efficient trip planning.

Chapter 2 Vehicle Model Development Validation

In this chapter, the development of an open loop, forward-looking model of the vehicle for energy evaluation and control design is presented. Then, the experimental testing and data acquisition process is described, and the collected data is used to perform the vehicle calibration. Finally, the validation of the forward-looking PHEV vehicle simulator is shown.

2.1 Overview of the Vehicle

Figure 2.1: Chrysler Pacifica PHEV

The vehicle considered in this work is a 2017 Chrysler Pacifica PHEV minivan (Figure 2.1) equipped with a 3.6L Pentastar® engine and an eFlite® hybrid electric transmission [70]. The vehicle includes three power sources: two permanent magnet synchronous AC electric motors, motor generator A (MGA) and motor generator B (MGB), and a 24-valve Atkinson cycle V-6 ICE in a power-split configuration for a combined 260 HP [71]. The vehicle is equipped with a 16kWh liquid-cooled lithium-ion battery. A schematic of the system is shown in Figure 2.2.

The transmission includes a planetary gear set connected to the ICE and MGA, which is linked to MGB and the drive shaft through a transfer gear. This continuously variable automatic transmission allows both electric motors to perform charging and traction operations in combination with the engine. The AER of the vehicle is 33 miles, and the vehicle is rated 28 MPG when using both gasoline and electricity [72]. Given the power-split hybrid configuration shown, the vehicle can operate in five different modes, as summarized in Table 2.1.

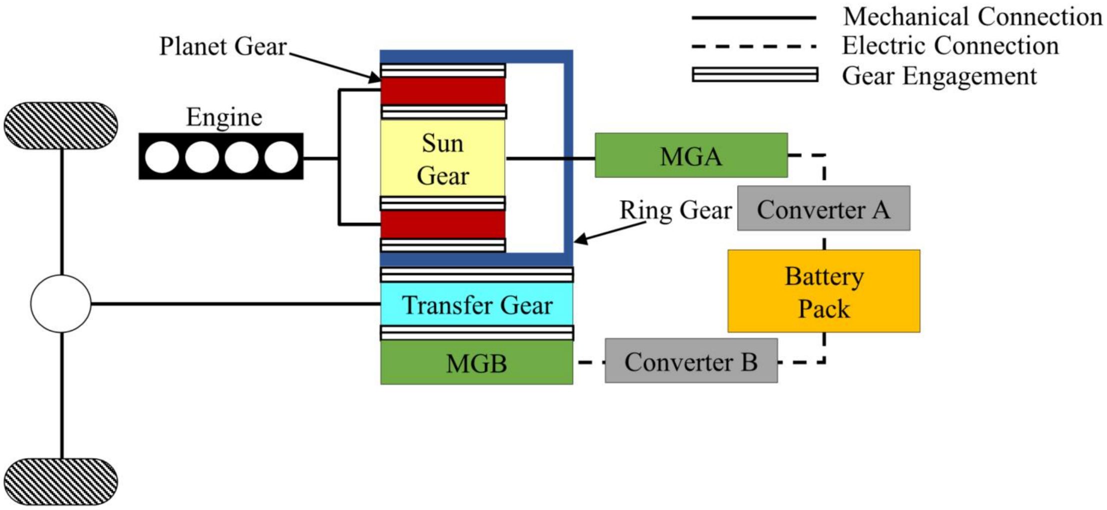

Figure 2.2: Chrysler Pacifica Powertrain Model

Table 2.1: Summary of Vehicle Operation Modes

Operation Mode	Engine Power	MGA Power	MGB Power
EV – MGB	0	0	+
EV – MGA/MGB	0	+	+
Regen	0	-/0	-
HEV	+	-	+
HEV Boost	+	+	+/-

In EV mode, either MGB supplies all the necessary traction, or works in combination with MGA to propel the vehicle; meanwhile, the engine is held static with a one-way clutch when MGA is in traction [47]. Regeneration is performed by MGB or a combination of MGA and MGB when the negative power is large. When the vehicle operates in HEV mode, the traction power is provided by a combination of the ICE and the two electric motors, indicating a charge sustaining operation. Finally, in cases demanding a large torque, MGA, MGB, and the ICE can all provide torque to the wheels in the HEV Boost mode.

2.2 Vehicle Energy Simulation Model

2.2.1 Overview of the Model

The model developed is a forward-looking simulator that predicts the energy consumption of the vehicle. A block diagram of the open-loop vehicle model is shown in Figure 2.3, where the main components, namely the transmission, ICE, electric machines, battery, and longitudinal vehicle dynamics are highlighted. The model inputs are the engine speed $\omega_{ICE}(t)$, and the mechanical torques provided by the two electric motors $T_{MGA}(t)$ and $T_{MGB}(t)$, respectively. In addition, the model requires the power demand from the auxiliaries $P_{AUX}(t)$, the road grade $\alpha(t)$, and the brake force applied $F_{BRAKE}(t)$. The model has two states: the battery state of charge $SoC(t)$ and the vehicle speed $v(t)$.

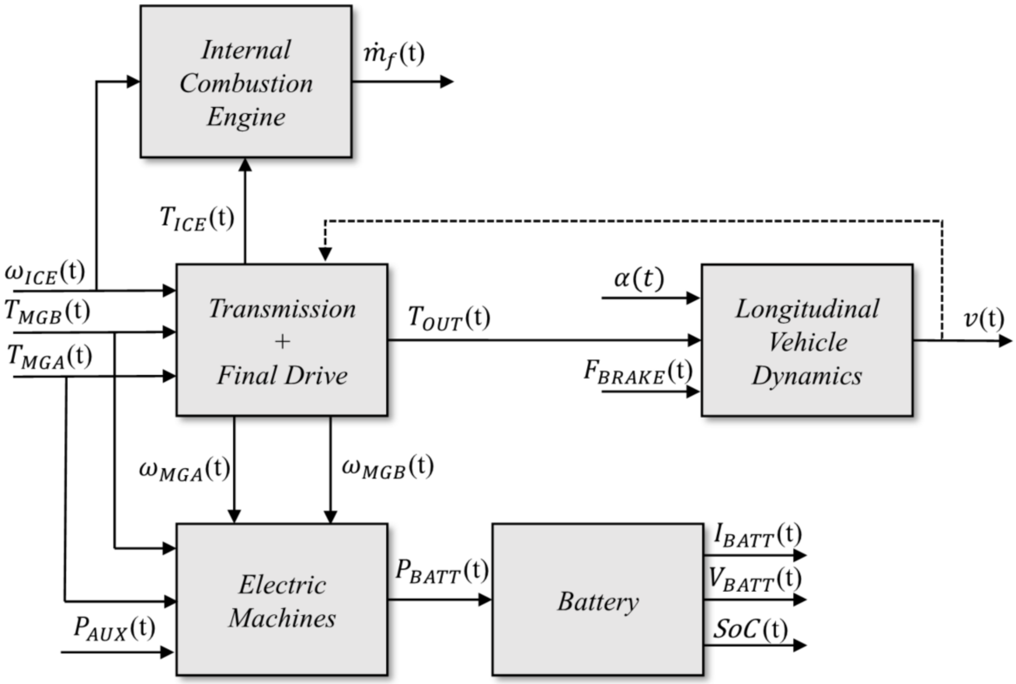

Figure 2.3: Block Diagram of the Powertrain and Vehicle Dynamics Model

2.2.2 Engine

The fuel consumption of the 3.6L Pentastar® engine is modeled as a function of engine speed and torque using the static fueling map provided by the OEM and shown in Figure 2.4:

$$\dot{m}_f\,(t) = \psi\big(\omega_{ICE}(t), T_{ICE}(t)\big) \tag{2.1}$$

The idle speed of the engine is 1100 rpm and the maximum engine speed is 5792 rpm shown in Figure 2.4. The engine torque is limited below the maximum torque line shown in black.

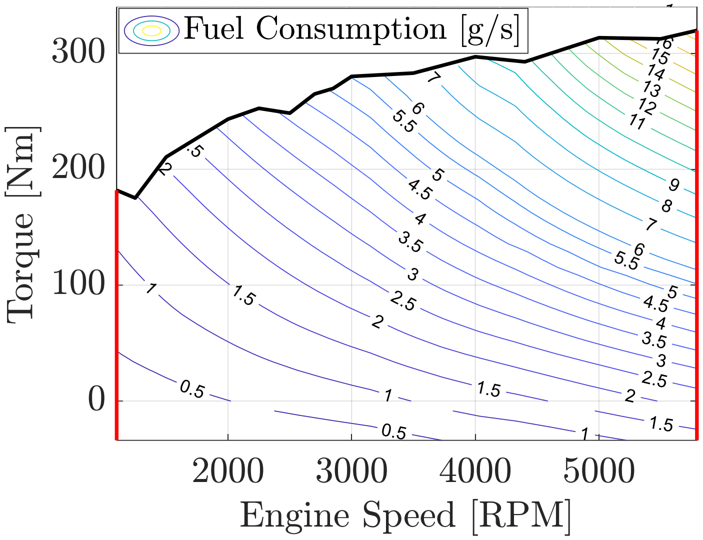

Figure 2.4: Engine Fuel Consumption Map as a Function of Engine Speed and Torque

2.2.3 Battery Pack

The 16kWh, 47.7 Ah lithium-ion battery pack is modeled using a zeroth order equivalent circuit [46], as shown in Figure 2.5, while its I/O structure is shown in Figure 2.6.

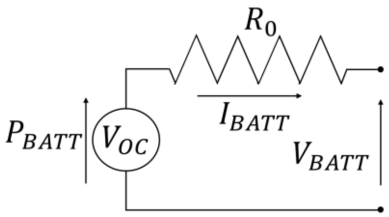

Figure 2.5: Zeroth Order Equivalent Circuit Model

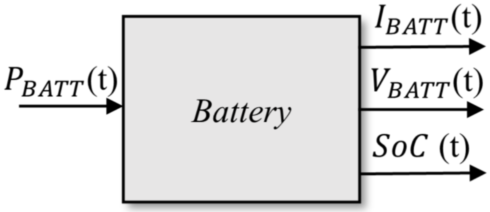

Figure 2.6: Battery Model Input/Output Structure

The governing equations that determine the battery current $I_{BATT}(t)$, state of charge $SoC(t)$, and battery voltage $V_{BATT}(t)$ are:

$$I_{BATT}(t) = \frac{V_{oc}\big(SoC(t)\big) - \sqrt{V_{oc}\big(SoC(t)\big)^2 - 4 \cdot P_{BATT}(t) \cdot R_0\big(SoC(t)\big)}}{2 \cdot R_0\big(SoC(t)\big)} \tag{2.2}$$

$$\frac{dSoC(t)}{dt} = -\frac{1}{C_{nom}} \cdot I_{BATT}(t) \tag{2.3}$$

$$V_{BATT}(t) = V_{oc}\big(SoC(t)\big) - I_{BATT}(t) \cdot R_0\big(SoC(t)\big) \tag{2.4}$$

where $P_{BATT}(t)$ is the battery power demand, C_{nom} is the nominal capacity of the battery, V_{oc} is the open circuit voltage, and R_0 is the internal resistance. Both open circuit voltage and internal resistance are functions of the state of charge.

2.2.4 Electric Machines

To determine the battery power demand $P_{BATT}(t)$, a static model of the two electric machines is developed to compute their power through efficiency maps. The block diagram is shown in Figure 2.7. The dynamic response is assumed to be much faster compared to the relevant dynamics of the vehicle model and is therefore neglected [73]. The battery power is determined using the following power balance:

$$P_{BATT}(t) = P_{MGA}(t) + P_{MGB}(t) + P_{AUX}(t) \tag{2.5}$$

where P_{AUX}(t) includes, among others, the engine cooling fan, HVAC, and lighting. The electrical power from the two machines is calculated using a power balance at the shaft [46]:

$$P_{MGA}(t) = \omega_{MGA}(t) \cdot T_{MGA}(t) + \ Ploss_{MGA}\big(\omega_{MGA}(t), T_{MGA}(t)\big) \tag{2.6}$$

$$P_{MGB}(t) = \omega_{MGB}(t) \cdot T_{MGB}(t) + \ Ploss_{MGB}\big(\omega_{MGB}(t), T_{MGB}(t)\big) \tag{2.7}$$

where $T_{MGA}(t)$ is the torque provided by MGA, $T_{MGB}(t)$ is the torque provided by MGB, $\omega_{MGA}(t)$ is the speed of MGA, and $\omega_{MGB}(t)$ is the speed of MGB. The MGA and MGB power loss maps ($Ploss_{MGA}$ and $Ploss_{MGB}$) are supplied by the OEM and dependent on motor speed and torque.

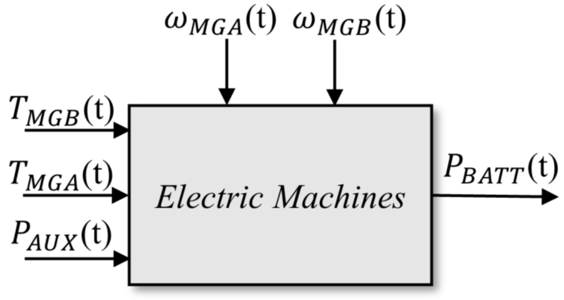

Figure 2.7: Electric Machines Model Input/Output Structure

2.2.5 Transmission and Final Drive

The transmission and final drive subsystem includes the gearbox, differential, and final drive shaft. Figure 2.8a shows the input/output structure of this subsystem, with the speed of the engine and the torques of the two electric machines, together with the vehicle speed as inputs. The outputs are the torque of the engine, the total output torque, and the speed of both electric machines.

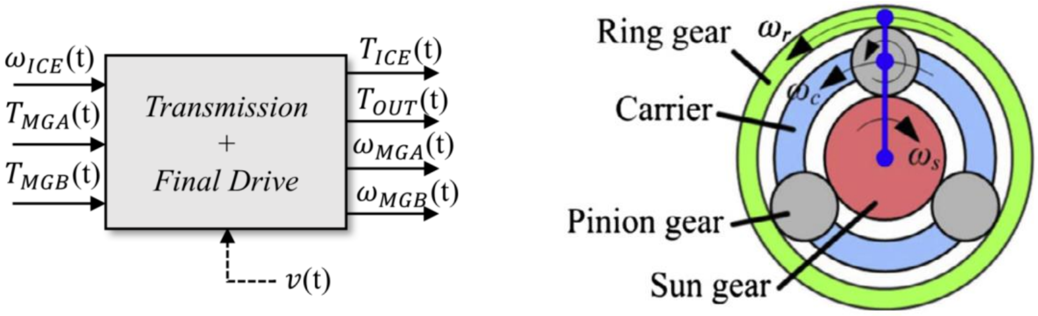

(a) (b)

Figure 2.8: (a) Transmission and Final Drive Model Input/Output Structure, (b) Planetary Gear Set Model [74]

The gearbox includes a planetary gear set (PGS) that connects the engine and electric machines to the vehicle drive axle. A planetary gear set, shown in Figure 2.8b, consists of a sun gear, planetary carrier, and ring gear. The static speed and torque relationships between the three components in a planetary gear set is described by the speed and torque balance [75]:

$$\omega_S = \omega_C \frac{n_S + n_R}{n_S} - \omega_R \frac{n_R}{n_S} \tag{2.8}$$

$$T_S = -T_C \frac{n_S}{n_S + n_R} = -T_R \frac{n_S}{n_R} \tag{2.9}$$

where ω, T, and n are the speed, torque, and number of teeth, while the subscripts $S, R,$ and C indicate the sun, the ring, and the carrier respectively. The governing speed equations for the transmission and final drive are derived from simple gear ratios and from Eq. (2.8) [47]:

$$\omega_{wheel}(t) = \frac{v(t)}{R_{wheel}} \tag{2.10}$$

$$\omega_{MGB}(t) = \frac{n_T}{n_B} \tau_{FD} \omega_{wheel}(t) \tag{2.11}$$

$$\omega_{MGA}(t) = \frac{n_S + n_R}{n_S} \omega_{ICE}(t) - \frac{n_R n_T}{n_S n_{\bar{R}}} \tau_{FD} \omega_{wheel}(t) \tag{2.12}$$

where ω_{wheel} is the wheel speed, R_{wheel} is the wheel radius, and ω_{MGA} and ω_{MGB} represent the speed of MGA and MGB, respectively. The number of teeth on the transfer gear is n_T, n_B is the number of teeth on the gear connected to MGB, n_S is the number of teeth on the gear connected to MGA (sun), and τ_{FD} is the final drive ratio. The number of teeth on the outer circumference of the ring gear that meshes with the transfer gear is denoted by $n_{\bar{R}}$, and n_R is the number of teeth on the inner circumference of the ring gear that meshes with the pinion gears.

The relationship between the ICE and MGA torque is derived from the PGS Eq. (2.9) as the sun gear is connected to MGA and the planetary carrier is connected to the ICE:

$$T_{ICE}(t) = \begin{cases} -\dfrac{n_R + n_S}{n_S} T_{MGA}(t) & if(\omega_{ICE}(t) > 0.1) \\ 0 & if(\omega_{ICE}(t) \leq 0.1) \end{cases} \tag{2.13}$$

where $T_{ICE}(t)$ is the torque of the engine and $T_{MGA}(t)$ is the torque of MGA. Under the assumption that the transmission losses are negligible, the ideal output torque at the wheel is given by:

$$T_{OUT_{IDEAL}}(t) = \tau_{FD}\left(T_{MGB}(t)\frac{n_T}{n_B} - \frac{n_R}{n_S}\frac{n_T}{n_{\bar{R}}}T_{MGA}(t)\right) \tag{2.14}$$

and the associated ideal output power by:

$$P_{OUT_{IDEAL}}(t) = T_{OUT_{IDEAL}}(t)\omega_{wheel}(t) \tag{2.15}$$

To determine the actual torque output, two types of power losses are considered in the system: mesh losses and spin losses. Mesh losses are mechanical power losses caused by friction at the gear and bearing surface contact and are load dependent, while spin losses are caused by gears in the system spinning without transmitting torque [76]. In this transmission model, it is assumed that the mesh losses are a function of the ideal output power (Eq. (2.15)) and wheel speed, and the spin losses are a function of the wheel speed and engine speed. The load distribution and the friction at each contact point are the primary contributors of mesh losses. Hence to model the mesh losses, the load is characterized by the output power and the friction is characterized by the output speed [77]. The spin losses of a simple gear are a function of the gear speed. The PGS uses centrifugal force to deliver oil through the lubrication channels and therefore needs the speed of the carrier to characterize the losses due to the lubrication [77]. The transmission power losses are given by:

$$P_{losses}(t) = P_{meshlosses}\left(P_{OUT_{IDEAL}}(t), \omega_{wheel}(t)\right) + P_{spinlosses}\left(\omega_{wheel}(t), \omega_{ICE}(t)\right) \tag{2.16}$$

which can be converted into an equivalent torque at the output shaft under the assumption that the gears rotate with the previously specified gear rotation speed; therefore, the net effect of the losses from the load distribution and lubrication can be fully captured by the torque [78]:

$$T_{losses}(t) = \frac{P_{losses}(t)}{\omega_{wheel}(t)} \tag{2.17}$$

Finally, the actual output torque is calculated by subtracting the losses from the ideal output torque:

$$T_{OUT}(t) = T_{OUT_{IDEAL}}(t) - T_{losses}(t) \tag{2.18}$$

2.2.6 Longitudinal Vehicle Dynamics

The vehicle speed is described using the road load equation [47]:

$$M_{eq} \cdot \frac{dv(t)}{dt} = \frac{T_{OUT}(t)}{R_{wheel}} - F_{brake}(t) - F_{RL}\big(v(t)\big) \tag{2.19}$$

where $F_{brake}(t)$ is the mechanical brake force, M_{eq} is the equivalent mass of the vehicle, and $F_{RL}(t)$ is the resistive force acting on the vehicle. The equivalent mass of the vehicle accounts for the inertia of rotating powertrain components inside the vehicle as well as its measured mass [79]:

$$M_{eq} = M + 4 \cdot \frac{I_{wheel}}{R_{wheel}^2} + \frac{I_{ICE}}{R_{wheel}^2} \cdot \left(\frac{n_T}{n_R + n_S} \cdot \tau_{FD}\right)^2 + \frac{I_{MGA}}{R_{wheel}^2} \cdot \left(\frac{n_T}{n_S} \cdot \tau_{FD}\right)^2 + \frac{I_{MGB}}{R_{wheel}^2} \cdot \left(\frac{n_T}{n_B} \cdot \tau_{FD}\right)^2 \tag{2.20}$$

where M is the vehicle mass, and $I_{wheel}, I_{ICE}, I_{MGA}, I_{MGB}$ are the rotational inertias of the wheels, ICE, MGA, and MGB. The road load force acts on a vehicle driving at a steady speed over a smooth surface. Road load force accounts for aerodynamic drag, rolling resistance force, and the force applied by gravity due to the road grade [80]:

$$F_{RL}(t) = F_{aero}(t) + F_{roll}(t) + F_{grade}(t) \tag{2.21}$$

The road grade element of the road load equation is given by:

$$F_{grade}(t) = M_{eq} \cdot g \cdot sin(\alpha(t)) \tag{2.22}$$

where g is the acceleration due to gravity, and $\alpha(t)$ is the road grade. The sum of rolling resistance force and aerodynamic drag force can be expressed using road load coefficients A, B, and C, provided by Stellantis:

$$F_{aero}(t) + F_{roll}(t) = C \cdot v(t)^2 + B \cdot v(t) + A \tag{2.23}$$

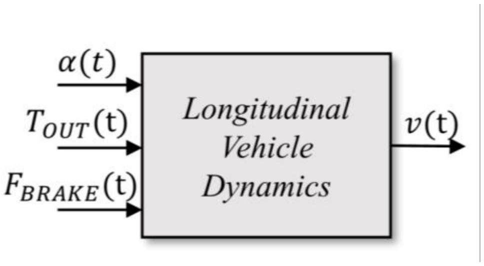

Figure 2.9: Longitudinal Vehicle Dynamics Model Input/Output Structure

2.3 Experimental Testing and Data Analysis

2.3.1 Vehicle Instrumentation

The Chrysler Pacifica PHEV was instrumented to collect experimental data for model calibration and to evaluate the baseline energy efficiency. The vehicle’s Controller Area Network (CAN) is connected to a dSPACE MicroAutoBox-III (MABX – III), a rapid prototyping system that provides an environment for data logging during vehicle operation, shown in Figure 2.10.

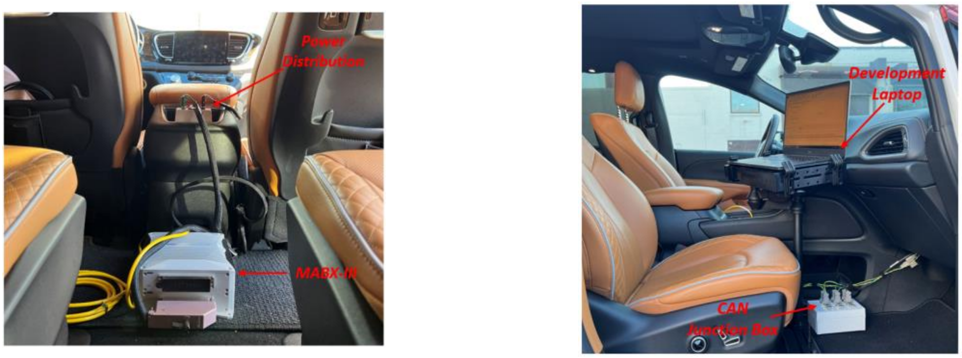

Figure 2.10: Installation of the MABX-III connection to CAN

2.3.2 Data Acquisition

Figure 2.11 shows the implementation of the MABX-III for data collection from the vehicle CAN.

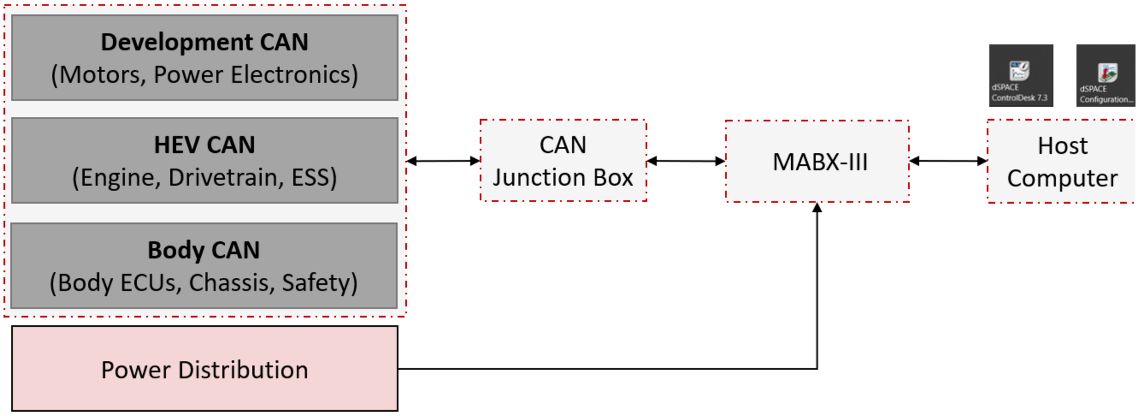

Figure 2.11: Instrumentation Setup with MABX-III used for Data Acquisition

The MABX-III collects the following signals necessary for model calibration and baseline energy analysis over many drive cycles:

- Engine torque, speed, and fuel flow measurements
- Electric machine torques and speeds
- Inverter currents and voltages
- Energy storage system measurements
- Auxiliary load voltages, currents, and power losses
- Mechanical and regeneration braking

2.3.3 Vehicle Testing

The vehicle is driven over multiple drive cycles to generate data for model calibration. Tests were performed by a human driver and run multiple times for each drive cycle for the purpose of eliminating the variability of a human driver. Two regulatory drive cycles were chosen:

- **Federal Test Procedure (FTP)** – A cycle representative of an urban route with many stop-and-go conditions (Figure 2.12a).
- **Multi-Cycle Test (MCT)** – A modified version of the regulatory MCT drive cycle, an EPA cycle for range evaluation of electric vehicles. The route is comprised of both urban and highway conditions (Figure 2.12b).

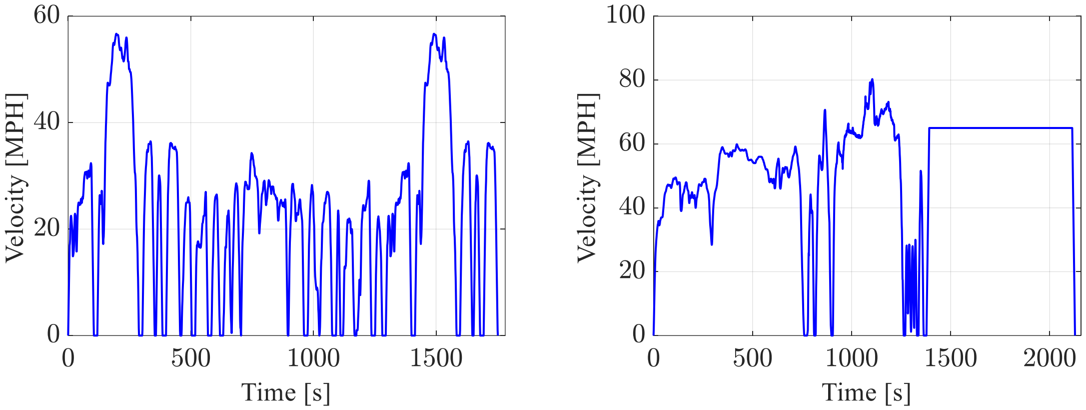

(a) (b)

Figure 2.12: Regulatory Drive Cycles: (a) FTP Cycle, (b) Modified MCT Cycle

In addition to the two regulatory drive cycles, three real-world routes in the central Ohio region routes were chosen to represent different driving conditions and provide additional datasets:

- **Route 19** – represents mixed-urban driving.

- **Mixed Route 1** – represents urban driving with multiple stops.
- **Mixed Route 4** – represents urban driving.

Figure 2.13 is collected using the TOMTOM mapping API and shows the speed limits associated with the three real-world routes.

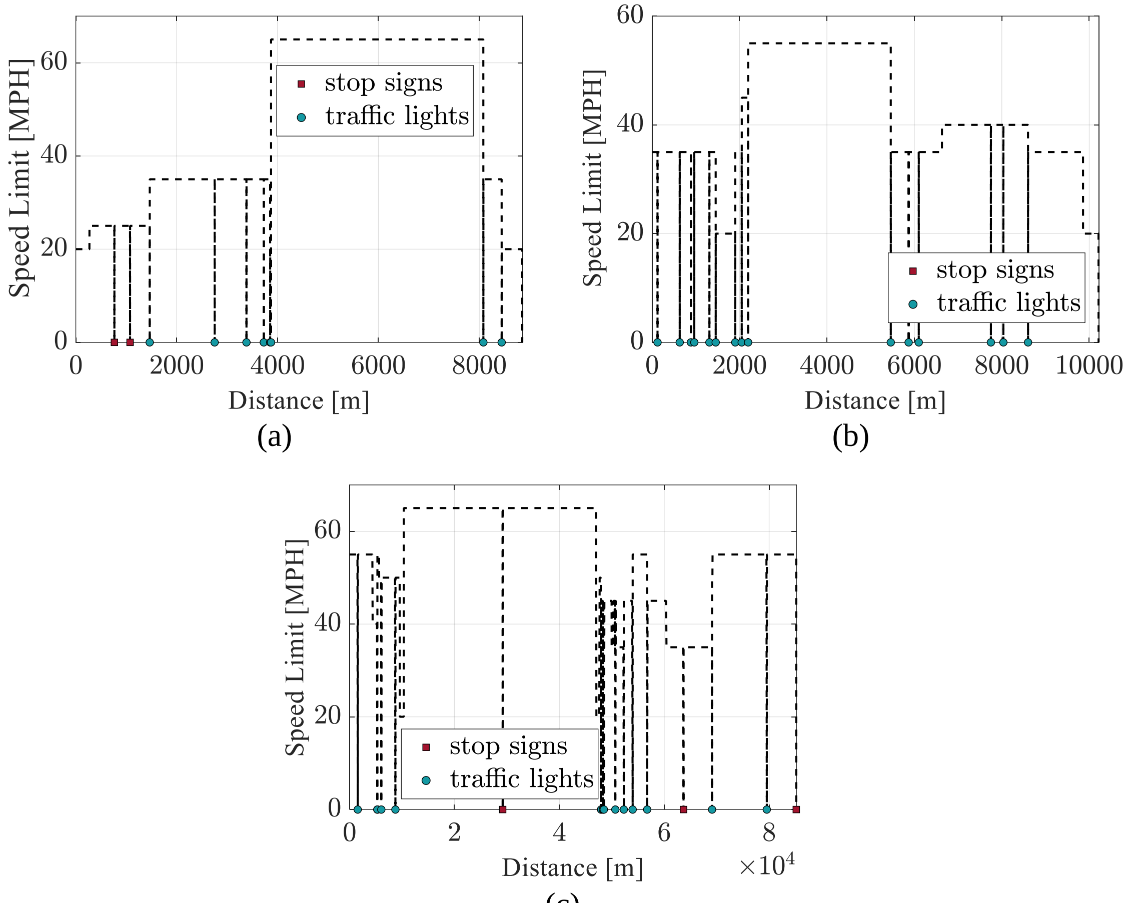

(c)

Figure 2.13: Speed Limit of Real-World Routes: (a) Route 19, (b) Mixed Route 1, (c) Mixed Route 4

To create realistic velocity profiles for aggressive, normal, and relaxed drivers, an Enhanced Driver Model (EDM) was used as a reference velocity predictor [81]. This model is a deterministic tunable driver model and is exercised under the assumption that traffic lights are treated as stop signs and the road is completely flat with free-flow conditions.

Testing was performed in a controlled manner where the vehicle weight was kept at a constant 5730lb, and all controllable accessory loads were turned off. Hence, the electrical auxiliary loads came from the thermal management system, the powertrain, and the MABX-III, which required a constant power draw of approximately 35 W.

2.3.4 Experimental Results

The Chrysler Pacifica production energy management strategy utilizes a Charge Depleting (CD) – Charge Sustaining (CS) approach. The torque demanded by the driver is satisfied by the electric motors until the battery is depleted to a certain setpoint, then hybrid mode completes the route. Due to the CD-CS production strategy, multiple routes were run for each cycle with varying initial states of charge (SoC_0) for three different energy management categories:

- Charge Depleting Only: The route is run using energy solely from the electric motors. The engine may turn on to satisfy a torque request above the electric motor limits.

- Charge Depleting and Charge Sustaining: The cycle begins with an initial state of charge above the CS setpoint and ends in CS mode, maintaining the setpoint state of charge.
- Charge Sustaining Only: The cycle begins with a depleted battery and sustains the setpoint state of charge for the entire route.

Figure 2.14 is an example of an MCT test following the CD-CS energy management strategy. The engine turns on briefly around 20s, 300s, and between 800-1000s even though the CD strategy is active because the torque demanded at those instances exceed the electric motor limits.

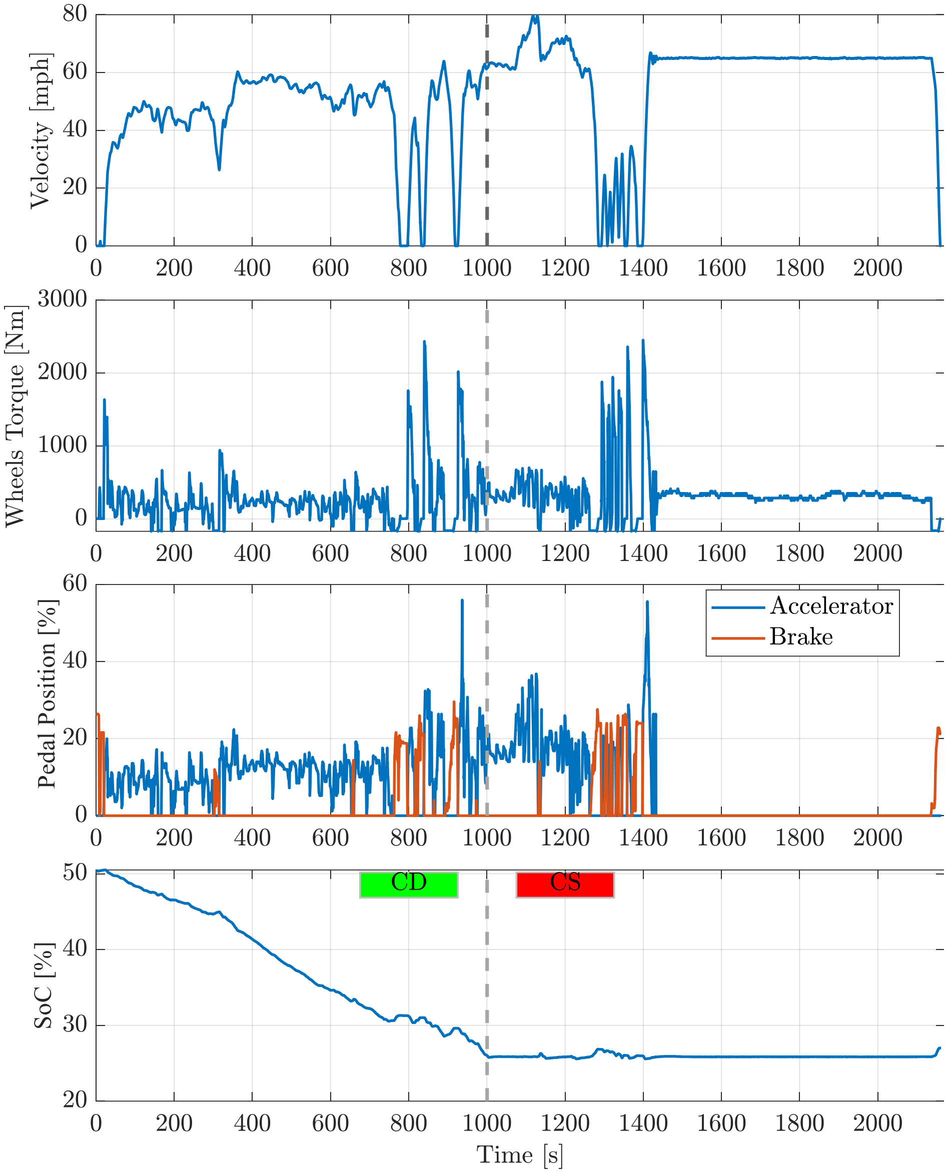

Figure 2.14: Evolution of vehicle velocity, requested torque, pedal positions, and SoC over the modified MCT Cycle

The results for the runs in which the initial state of charge is varied are summarized in Table 2.2 and Table 2.3. Table 2.2 covers the metrics for the regulatory drive cycles, while Table 2.3 covers the real-world route metrics with varying velocity profiles for each route based on driver aggressiveness.

Table 2.2: Metrics for Regulatory Drive Cycles

Cycle	**EMS Strategy**	$\boldsymbol{SoC_0}$[%]	$\boldsymbol{SoC_N}$[%]	**Fuel Consumed [g]**	**Net Battery Energy Consumed [kWh]**	**Travel Time [s]**
FTP	CD	85.79	67.67	0	2.90	1760
		61.68	41.68	0	3.20	1757
	CD-CS	34.46	25.66	508.05	1.41	1756
MCT	CS	26.43	27.03	3032.1	-0.10	2149
	CD-CS	50.30	27.01	2053.4	3.73	2162
		86.35	26.98	513.78	9.50	2149

Table 2.3: Metrics for Real-World Drive Cycles

Cycle	**EMS Strategy**	**Driver**	$\boldsymbol{SoC_0}$[%]	$\boldsymbol{SoC_N}$[%]	**Fuel Consumed [g]**	**Net Battery Energy Consumed [kWh]**	**Travel Time [s]**
Route 19	CD	Aggressive	61.34	51.23	127.37	1.62	725
			51.21	44.64	257.79	1.05	726
		Normal	86.74	77.41	0	1.49	749
			69.82	58.36	25.14	1.83	748
			38.34	28.23	149.58	1.62	748
		Relaxed	82.84	72.82	0	1.60	773
			71.87	61.64	0	1.64	774
	CS	Normal	26.52	26.69	524.76	-0.03	749
			26.25	25.96	481.65	0.05	749
		Relaxed	26.86	26.25	416.47	0.10	775
			26.30	26.01	454.63	-0.05	774
Mixed Route 1	CD	Aggressive	86.74	76.53	129.46	1.63	928
			75.36	63.03	14.63	1.97	928
			63.05	50.67	36.14	1.98	929
		Normal	85.74	74.02	0	1.88	960
			71.92	62.12	157.15	1.57	962
			60.00	46.64	55.89	1.98	959
		Relaxed	59.34	46.45	0	2.06	988
			45.54	33.89	29.95	1.86	988
	CS	Aggressive	27.91	25.40	464.37	0.40	929
			25.06	24.88	577.72	0.03	929
		Normal	26.42	24.49	517.27	0.31	959
			25.42	24.35	561.39	0.17	960
		Relaxed	25.62	24.71	486.74	0.15	991
			25.32	24.52	501.28	0.13	990
Mixed Route 4	CS	Aggressive	26.69	26.72	4451.3	-0.01	4261
		Normal	27.15	26.57	4404.5	0.09	4367
		Relaxed	26.64	26.59	4250.4	0.01	4477

The net battery energy consumption is the product of the difference between the initial and final state of charge and the total battery energy; therefore, charge sustaining routes have very low battery energy consumption. The final state of charge SoC_N for routes in charge depleting mode varies between 24 – 27 % SoC which defines the setpoint state of charge in the production energy management strategy.

2.4 Model Calibration / Validation

The model calibration and validation of the energy-based PHEV model is performed first at the component level, and then again at the complete vehicle level. This approach enables component-wise calibration, while ensuring that the vehicle model provides good agreement with the experimental data.

2.4.1 Power Limitations

By imposing the signals collected as part of the experimental campaign, such as electric motor torques, engine speed, brake force and auxiliary power, as inputs to the energy-based model, a preliminary verification of the complete vehicle model is performed. The inputs of the vehicle simulator are shown in Figure 2.15 for one of the CD-CS MCT routes.

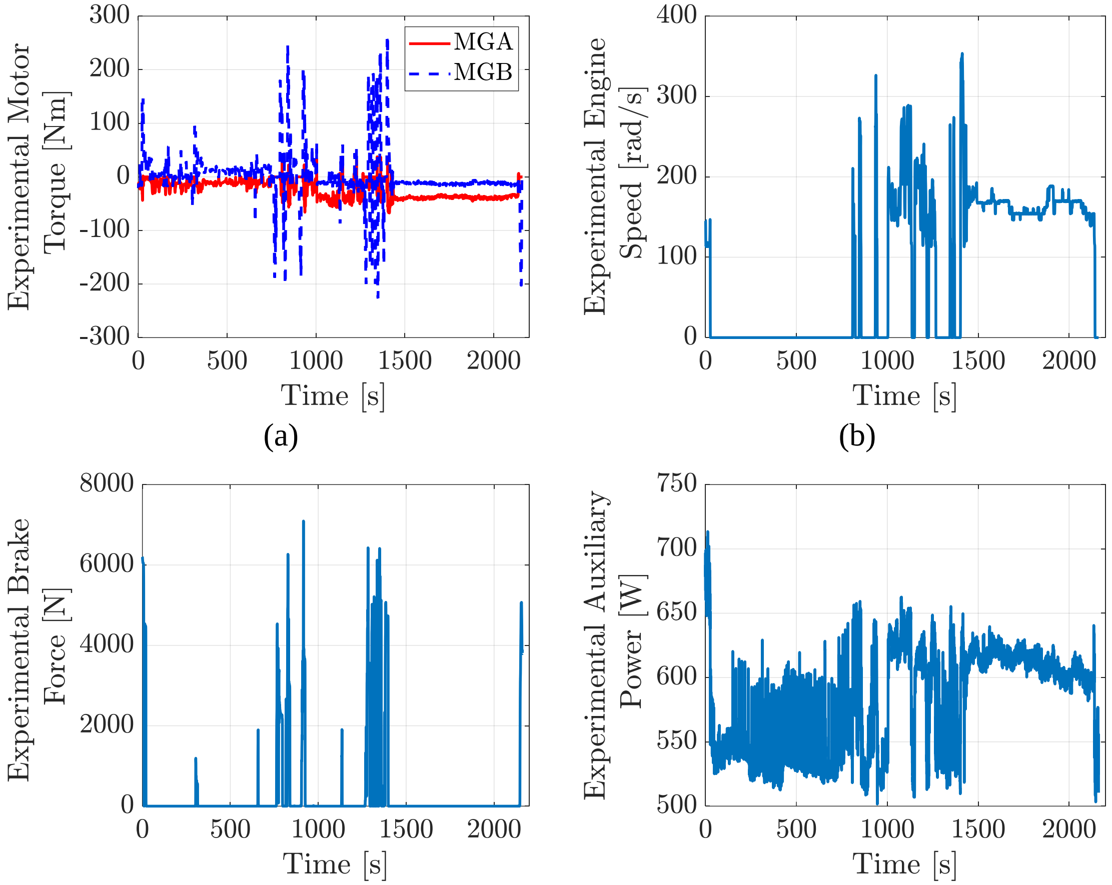

(a) (b)

(c) (d)

Figure 2.15: Experimental Inputs into the Vehicle Simulator for Calibration using the MCT Cycle: (a) Motor Torques, (b) Engine Speed, (c) Brake Force, (d) Auxiliary Power

The comparison between the predicted SoC against the in-vehicle data is shown in Figure 2.16, while the battery current is shown in Figure 2.17, and the battery voltage is shown in Figure 2.18. The error between the model prediction and the experimental data is computed by dividing the difference by the maximum absolute value among both model and data:

$$Error = \frac{data - model}{max(|data|, |model|)} \cdot 100 \qquad (2.24)$$

Overall, the model predicts the trend well during the CD section of the cycle but shows poor agreement during CS operations. Particularly, the model appears not to capture the transition between charge depleting and charge sustaining operations occurring at around 1000s, as shown in Figure 2.16.

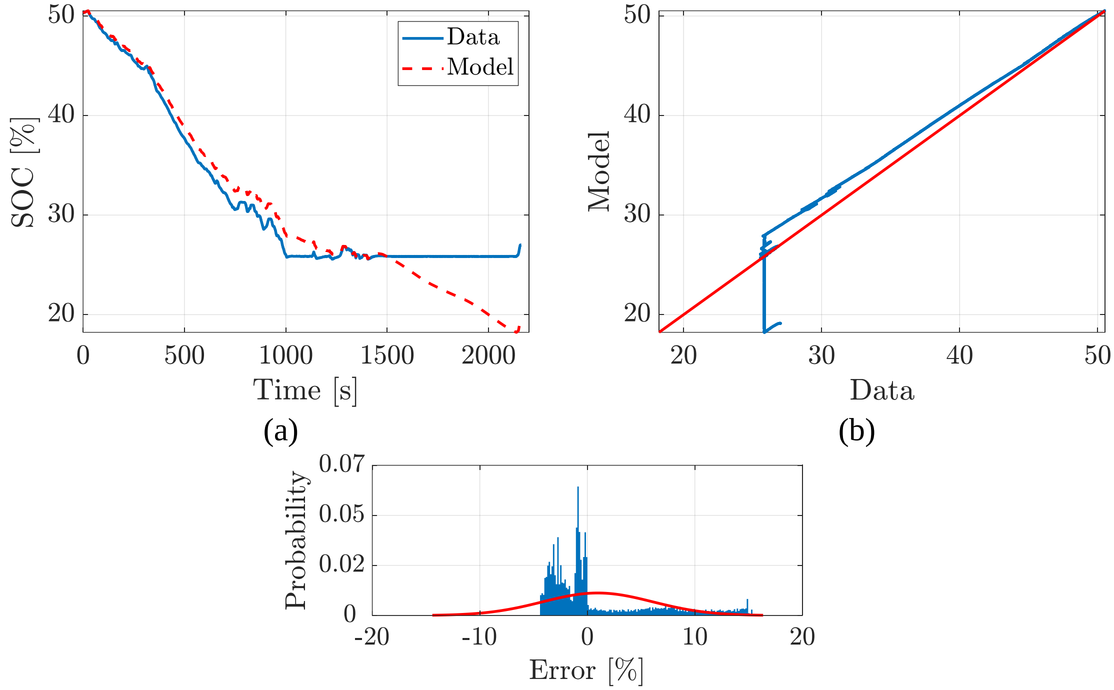

(a)

(b)

(c)

Figure 2.16: Comparison of Actual vs Predicted SoC: (a) Comparison of the Signals, (b) Correlation of the Signals, (c) Error Distribution

The deviation in SoC is due to the mismatch in the current shown in Figure 2.17. The model consistently predicts higher discharging currents. This is particularly evident in the last portion of the cycle where there is an offset between the data and the simulated value. The bimodal error distribution shown in Figure 2.17c is attributed to the behavior during charge depleting and the overestimation during the last portion of the cycle.

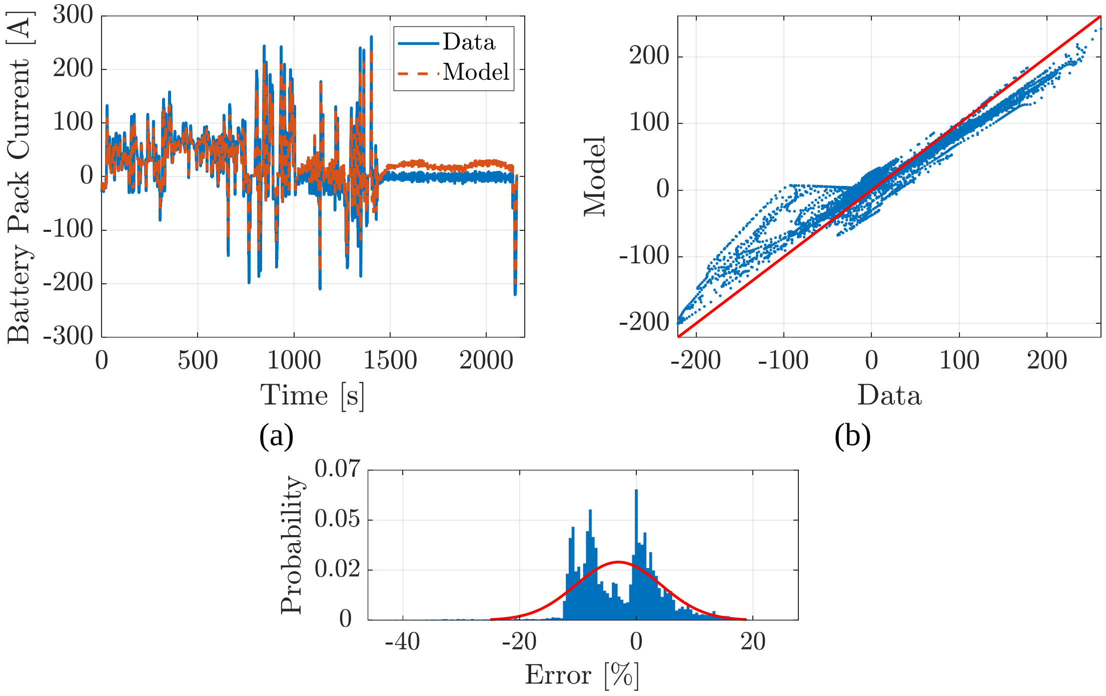

(a) (b)

(c)

Figure 2.17: Comparison of Actual vs Predicted Battery Current: (a) Comparison of the Signals, (b) Correlation of the Signals, (c) Error Distribution

Similar to the SoC and current, the voltage prediction in Figure 2.18 diverges from the data between 1500 – 2000s. The range of the error distribution is quite small because the deviation in the model prediction is a small ratio of the total voltage.

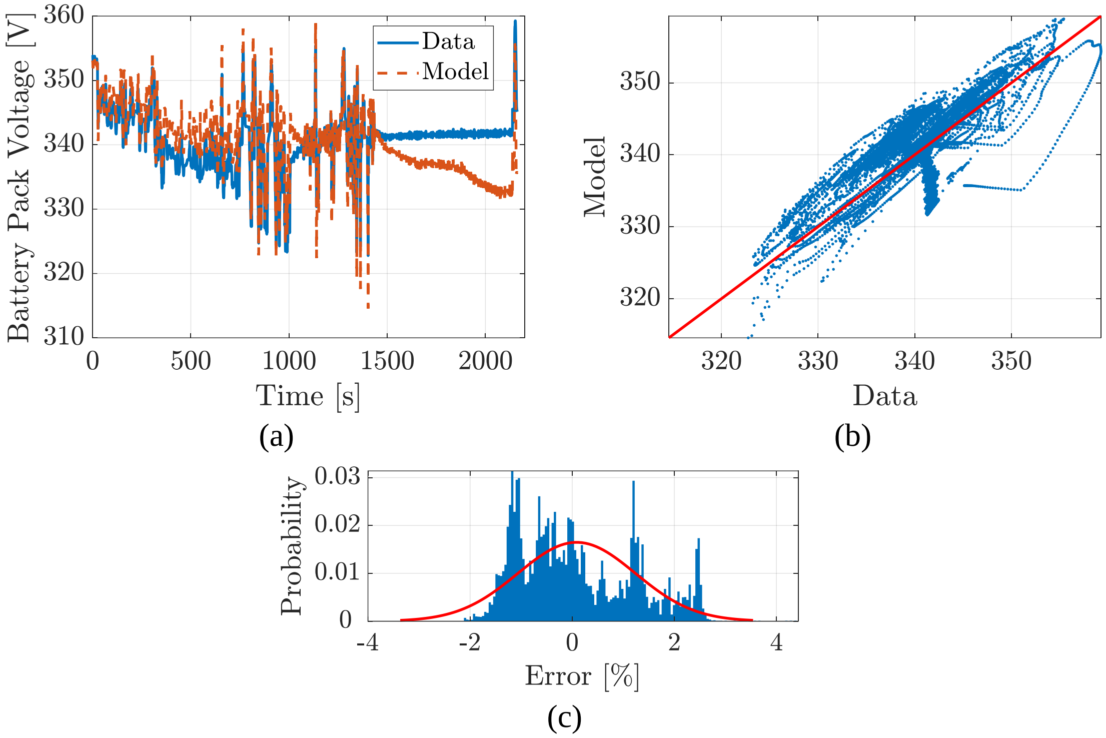

Figure 2.18: Comparison of Actual vs Predicted Battery Voltage: (a) Comparison of the Signals, (b) Correlation of the Signals, (c) Error Distribution

The source of the error is investigated by analyzing the battery power. Figure 2.19 shows a comparison of the power demands calculated in the model (purple) against the battery power demand in the data (yellow). Between 1500-2000s, the power demand predicted by the model maintains a positive value higher than the data, which oscillates around zero kW.

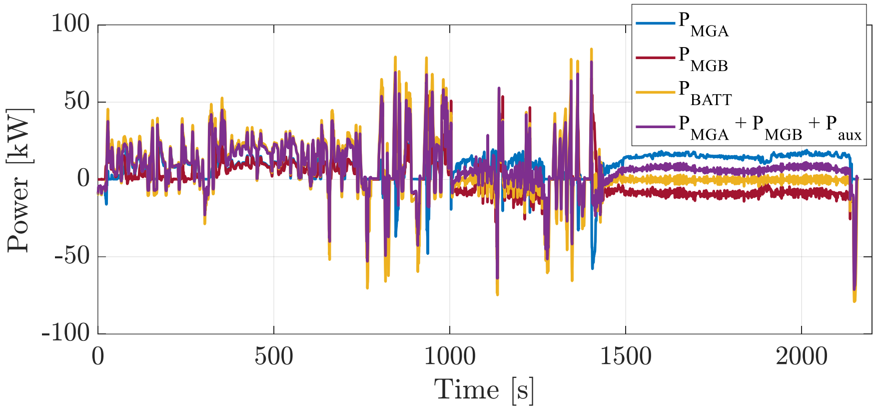

Figure 2.19: Comparison of Actual vs Predicted Electrical Power Demands

The power demand from the auxiliaries reaches a maximum of 700 W and would not affect the total power demand to the degree observed. Next, the simulated power demand from the electric motors is compared against the experimental powers, obtained by multiplying experimental motor current and voltage. This comparison, shown in Figure 2.20, shows an agreement in the MGB power demand and a disagreement in the MGA power demand. Through this investigation, it can be concluded that the original divergence in the battery subsystem can be traced back to the MGA power demand.

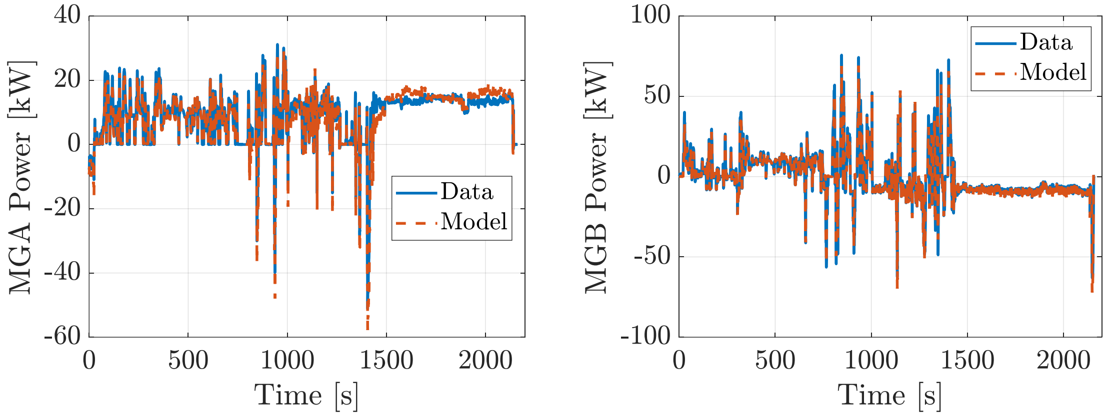

(a) (b)

Figure 2.20: Comparison of Actual vs Predicted Motor Power: (a) MGA Electrical Power Demanded (b) MGB Electrical Power Demanded

MGA speed is a function of the engine speed and the model predicted vehicle speed (Eq. (2.12)). The vehicle speed is the only factor that determines MGB speed, which is validated in Figure 2.20. The ICE speed is directly measured from the CAN. Therefore, the source of the error can be narrowed down to the MGA torque. The most plausible explanation for this error in the MGA torque demand is that value is logged before the vehicle controller modifies the signal.

The calibration approach used to correct the MGA torque is an implementation of the discharge power limits. Two types of power limits are included in the energy-based PHEV model. Namely, the SoC power limits that ensure the battery does not deplete past the minimum SoC value, and the OCV power limits that ensure the OCV does not fall below the minimum allowable battery voltage. These are both calculated using the SoC and voltage values from the previous time step:

$$P_{disc}^{SoC}(t) = \frac{SoC(t-1) - SoC_{min}}{\frac{\Delta t}{C_{nom}}} \cdot\ V_{BATT}(t-1) \tag{2.25}$$

$$P_{disc}^{OCV}(t) = \frac{V_{oc}(SoC(t-1)) - V_{BATT,min}}{R_0(SoC(t-1))} \cdot\ V_{BATT}(t-1) \tag{2.26}$$

where $V_{BATT,min}\ =\ 259.2\ V$ given by the supplier, $\Delta t\ =\ 1s$, and $SoC_{min} = 25.83\%$ determined from experimental data. The battery power limits are integrated in the model as:

$$P_{BATT,new}\ (t)\ =\ min(P_{disc}^{SoC}(t), P_{disc}^{OCV}(t), P_{BATT}(t)) \tag{2.27}$$

where P_{BATT} is the battery power defined in Eq. (2.5). The corrected power of MGA is calculated using the saturated battery power:

$$P_{MGA,new}(t)\ = P_{BATT,new}\ (t)\ -\ P_{MGB}(t) - P_{AUX}(t) \tag{2.28}$$

$$T_{MGA,new}(t)\ =\ \frac{P_{MGA,new}(t)\ -\ Ploss_{MGA}(\omega_{MGA}(t), T_{MGA}(t))}{\omega_{MGA}(t)} \tag{2.29}$$

$$T_{MGA_{min}}(\omega_{MGA}(t)) \leq T_{MGA,new}(t) \leq T_{MGA_{max}}(\omega_{MGA}(t)) \tag{2.30}$$

$$P_{MGA,new}(t)\ = P_{BATT,new}\ (t)\ -\ P_{MGB}(t) - P_{AUX}(t) \tag{2.31}$$

The corresponding constrained motor torque is:

$$T_{MGA,new}(t)\ =\ \frac{P_{MGA,new}(t)\ -\ Ploss_{MGA}(\omega_{MGA}(t), T_{MGA}(t))}{\omega_{MGA}(t)} \tag{2.32}$$

$$T_{MGA_{min}}(\omega_{MGA}(t)) \leq T_{MGA,new}(t) \leq T_{MGA_{max}}(\omega_{MGA}(t)) \tag{2.33}$$

Upon implementation of these power limits, the resulting model predicted SoC in Figure 2.21 shows charge sustaining behavior in agreement with the data. The battery current in Figure 2.22 has an improved correlation with the data, especially between 1500-2000s where the simulated battery current is close to zero. The model predicted battery voltage in Figure 2.23 also shows an improved performance with the calibration indicating less deviation between the model and the data.

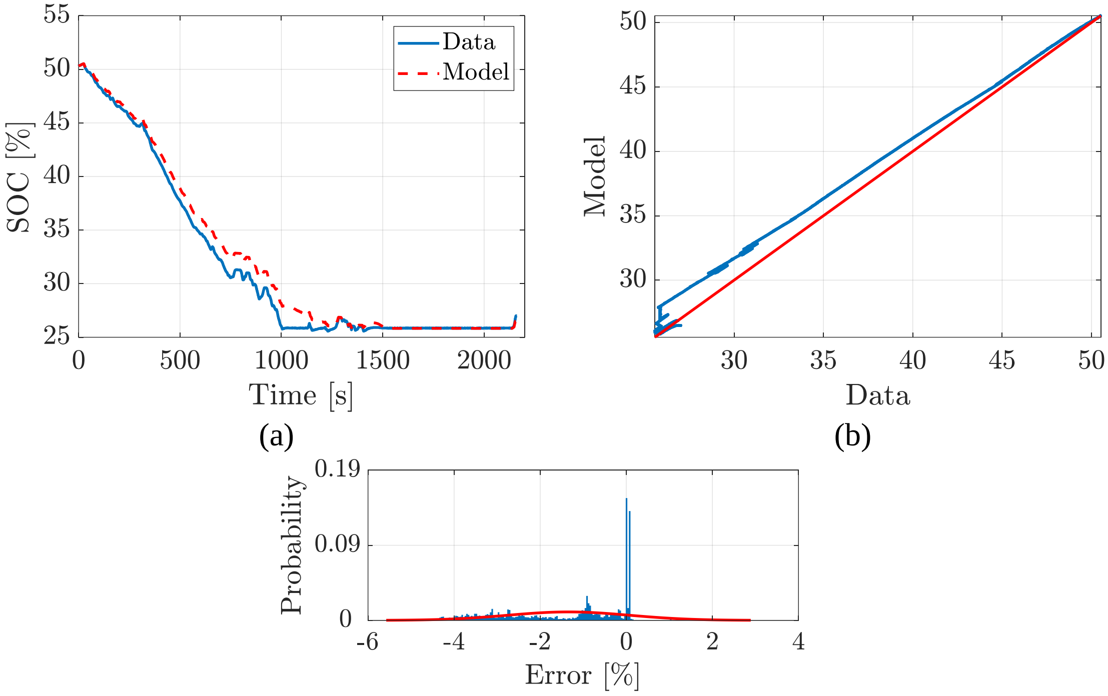

(a)

(b)

(c)

Figure 2.21: Comparison of Actual vs Calibrated Battery SoC: (a) Comparison of the Signals, (b) Correlation of the Signals, (c) Error Distribution

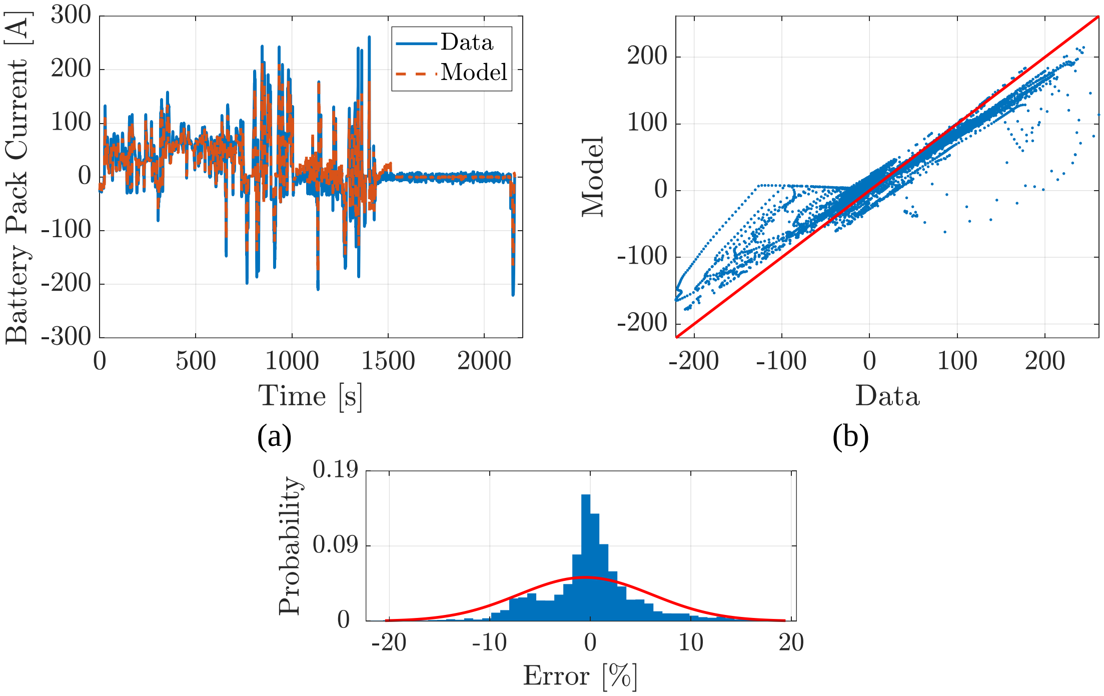

(a)

(b)

(c)

Figure 2.22: Comparison of Actual vs Calibrated Battery Current: (a) Comparison of the Signals, (b) Correlation of the Signals, (c) Error Distribution

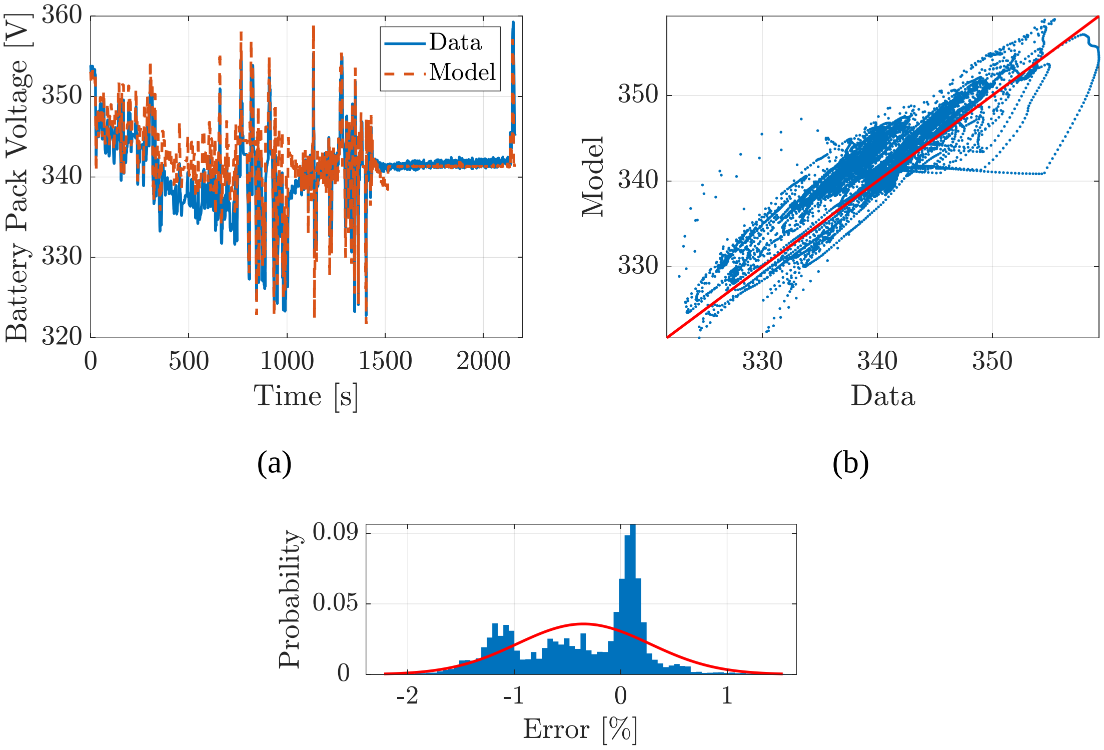

(a)

(b)

(c)

Figure 2.23: Comparison of Actual vs Calibrated Battery Voltage: (a) Comparison of the Signals, (b) Correlation of the Signals, (c) Error Distribution

Since the power limit calibration is performed on the MCT cycle, a different cycle is used for the validation. The CS run of the Mixed Route 4 cycle with a normal driver is selected and the corresponding inputs are shown in Figure 2.24.

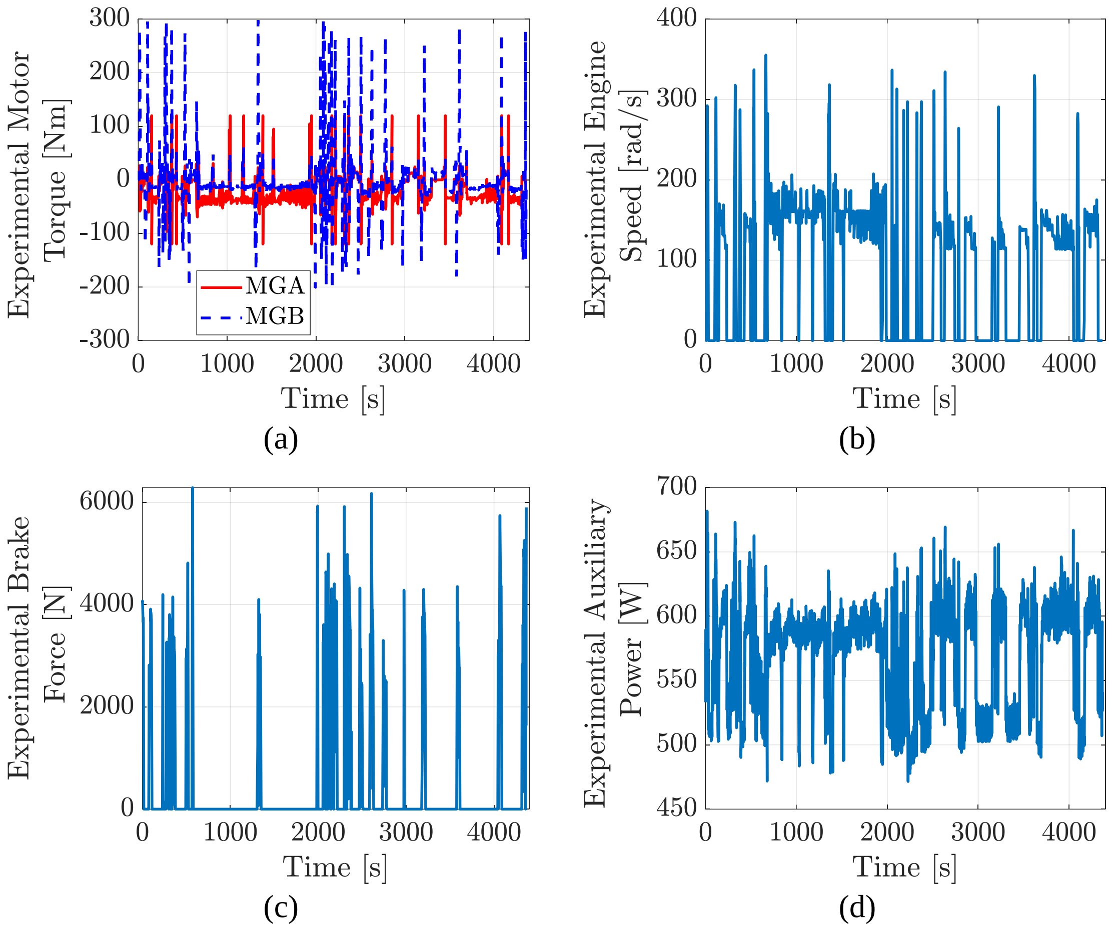

Figure 2.24: Experimental Inputs into the Vehicle Simulator for Validation using the Mixed Route 4 Cycle: (a) Motor Torques, (b) Engine Speed, (c) Brake Force, (d) Auxiliary Power

The predicted SoC, shown in Figure 2.25, remains above the minimum SoC while the SoC data occasionally falls below the minimum SoC. Despite this small discrepancy, the model SoC remains less than 2% SoC away from the data throughout the cycle. The battery current in Figure 2.26 and battery voltage in Figure 2.27 show a decreased overall error, with an average around zero.

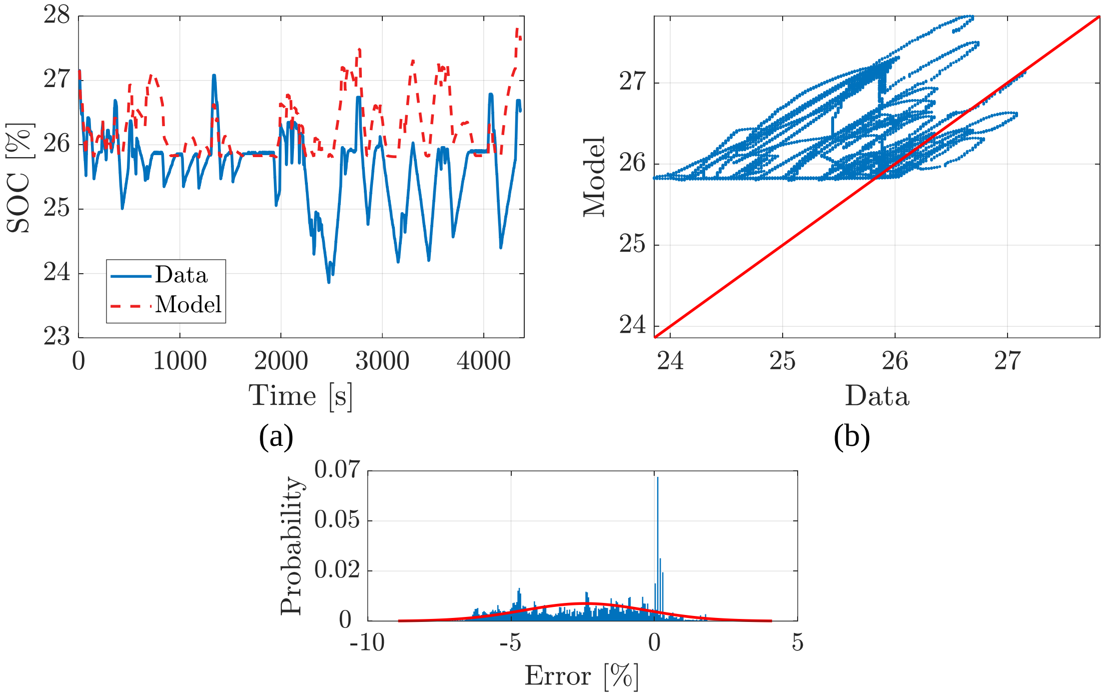

(a)

(b)

(c)

Figure 2.25: Comparison of Actual vs Calibrated Battery SoC for Validation: (a) Comparison of the Signals, (b) Correlation of the Signals, (c) Error Distribution

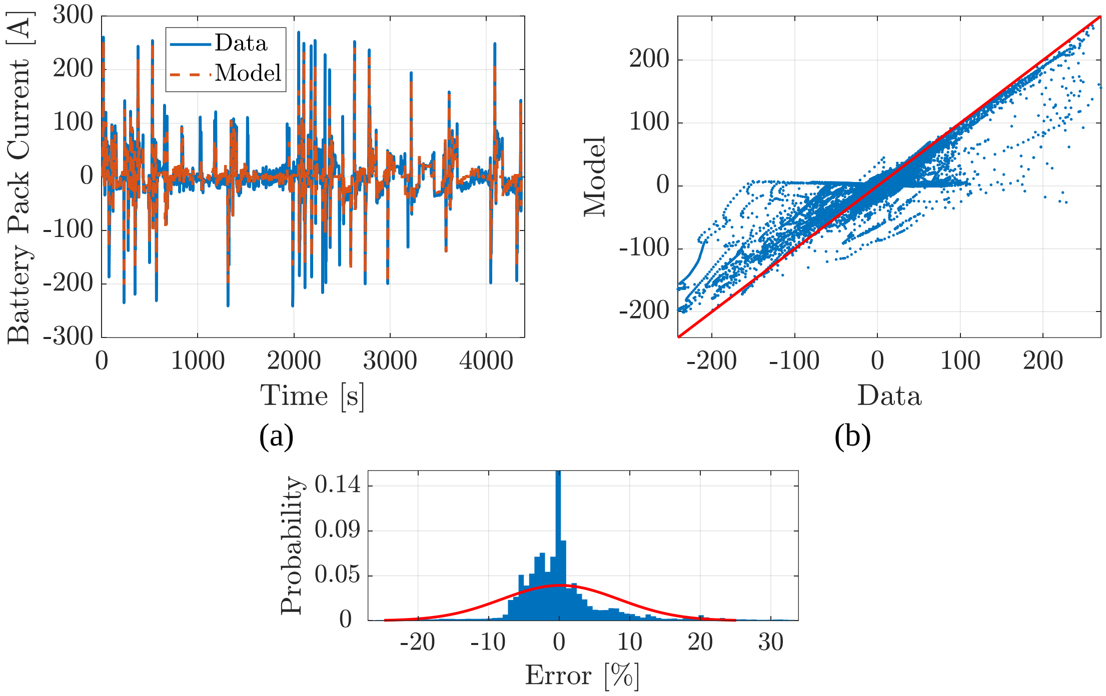

(a) (b) (c)

Figure 2.26: Comparison of Actual vs Calibrated Battery Current for Validation: (a) Comparison of the Signals, (b) Correlation of the Signals, (c) Error Distribution

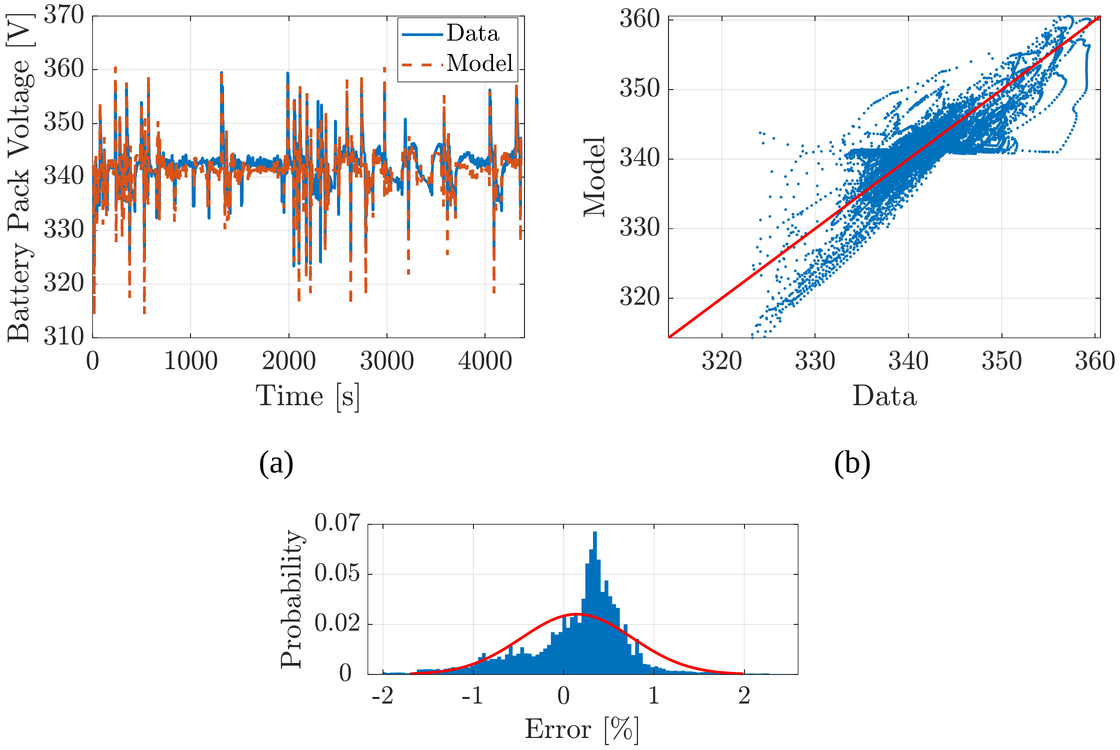

(a)

(b)

(c)

Figure 2.27: Comparison of Actual vs Calibrated Battery Voltage for Validation: (a) Comparison of the Signals, (b) Correlation of the Signals, (c) Error Distribution

2.4.2 Engine

The same run of Mixed Route 4 used to validate the power limits is also used to calibrate the engine fuel consumption. With the power limits included in the model, the predicted fuel consumption is shown in Figure 2.28. The cumulative fuel consumption is calculated as:

$$Fuel\ Consumed\ [g] = \int_0^T \dot{m}_f\, dt \tag{2.34}$$

where T is the simulation time. Because of the underestimation of fuel consumption by the model, the error accumulates between the cumulative model and data signals. At the end of the simulation, the predicted fuel consumption has an error of 12.3%.

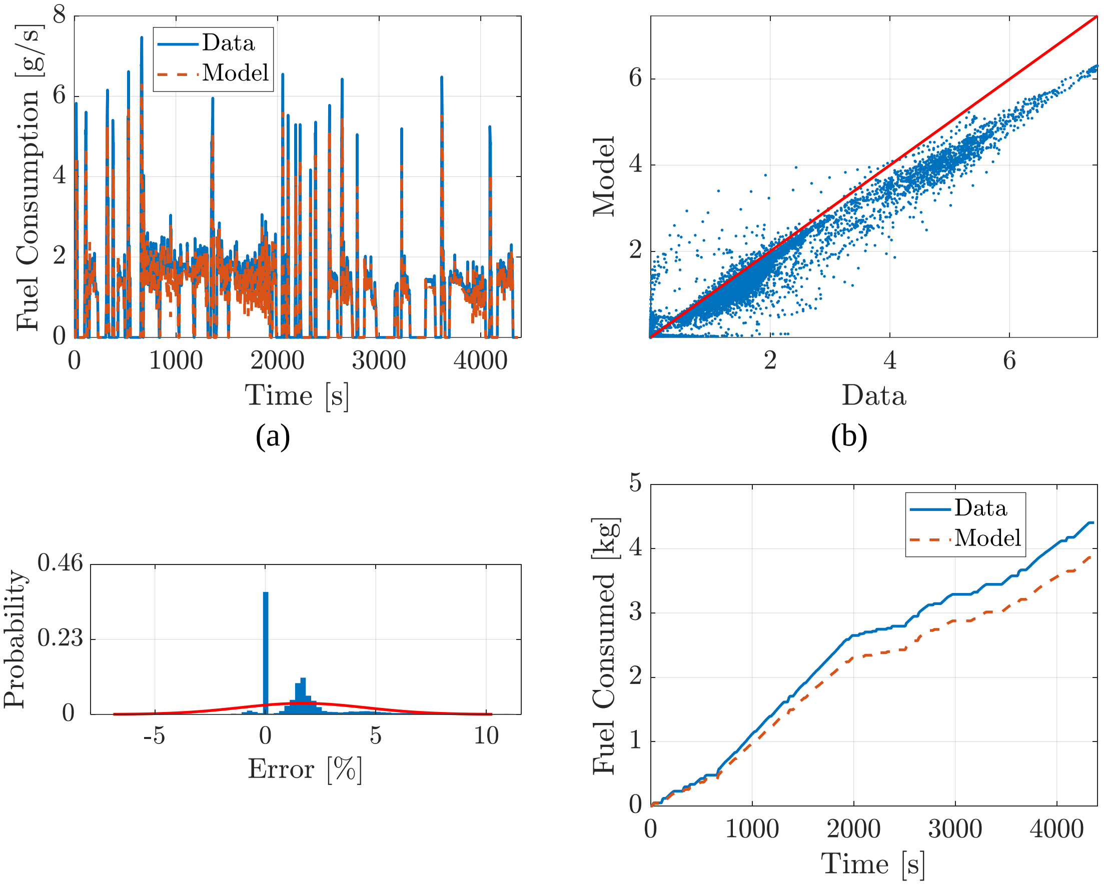

(a) (b)

(c) (d)

Figure 2.28: Comparison of Actual vs Predicted Fuel Consumption: (a) Comparison of the Signals, (b) Correlation of the Signals, (c) Error Distribution, (d) Comparison of Cumulative Consumption

To match the experimental data, the model is calibrated by including a gain:

$$\dot{m}_{f,new} = \dot{m}_f \cdot fuel_{gain} \tag{2.35}$$

where $fuel_{gain}$ is the calibration parameter. The value for $fuel_{gain}$ was determined numerically to be $fuel_{gain} = 1.155$ using the MCT cycle. The fuel consumption prediction after the calibration is shown in Figure 2.29. The error on the cumulative fuel consumption has been reduced to -1.3%.

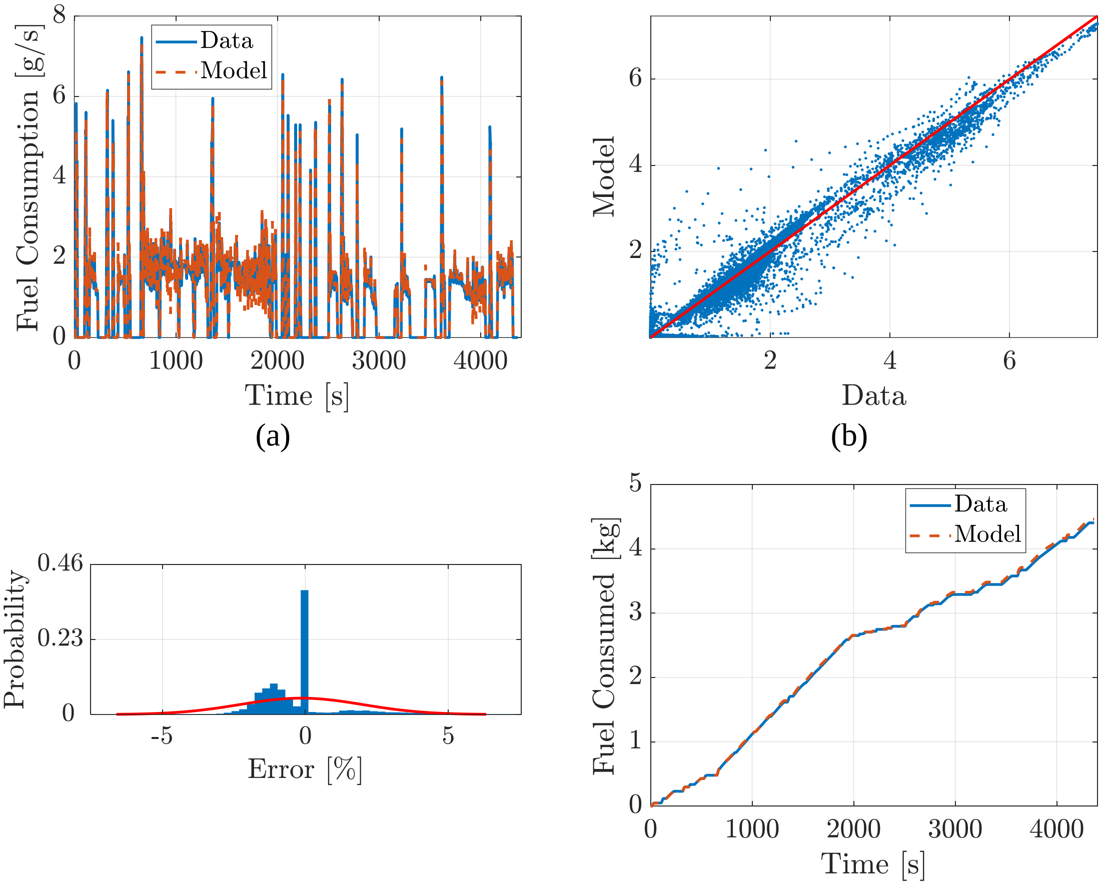

(a) (b)

(c) (d)

Figure 2.29: Comparison of Actual vs Calibrated Fuel Consumption: (a) Comparison of the Signals, (b) Correlation of the Signals, (c) Error Distribution, (d) Comparison of Cumulative Consumption

Finally, the correction factor is validated on a different cycle, namely the MCT CD-CS cycle. Simulation results show that the model predicts fuel consumption with a 4.1% average error.

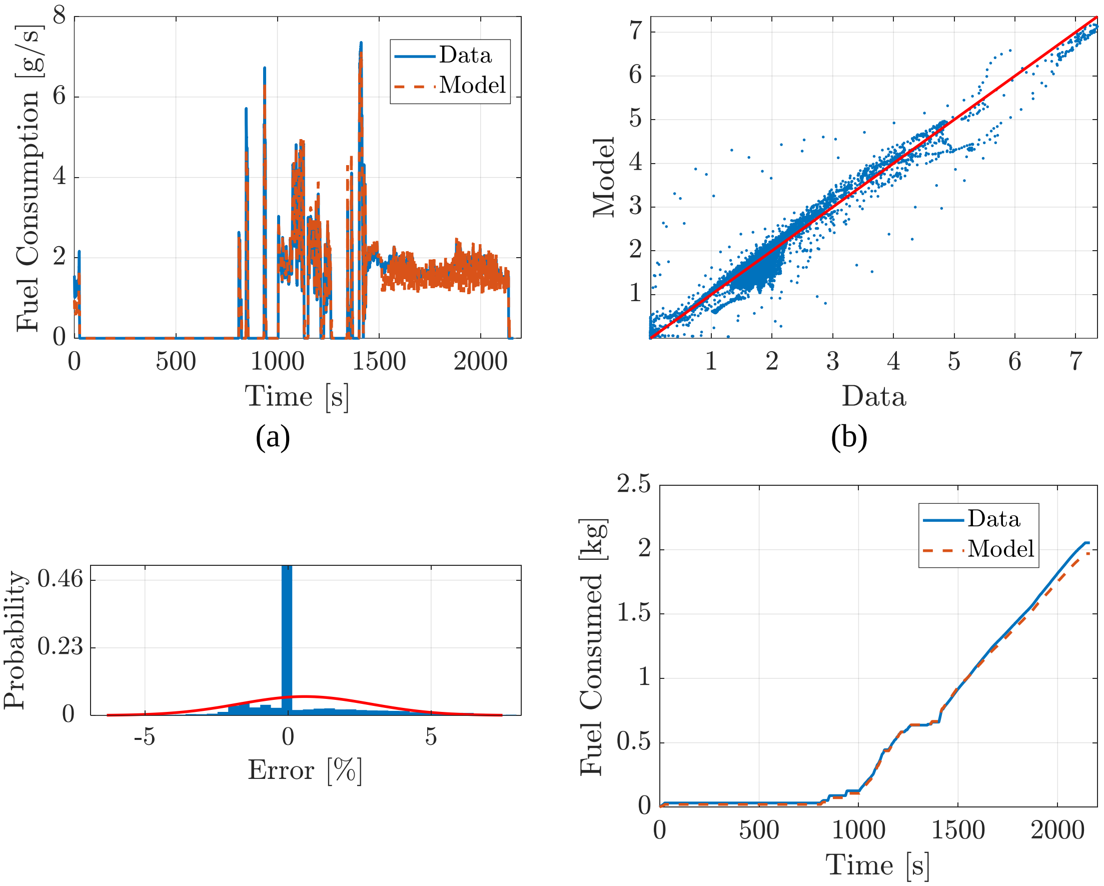

(a) (b)

(c) (d)

Figure 2.30: Comparison of Actual vs Calibrated Fuel Consumption for Validation on the MCT Cycle: (a) Comparison of the Signals, (b) Correlation of the Signals, (c) Error Distribution, (d) Comparison of Cumulative Consumption

2.5 Vehicle Simulator Validation

The block diagram of the vehicle simulator is shown in Figure 2.31. To verify the vehicle simulator's ability to predict energy usage, a validation is performed on an entirely different route than previously used for calibration. The vehicle simulator is validated on the normal driver, CS run of the Route 19 cycle. The inputs to the model are shown in Figure 2.32.

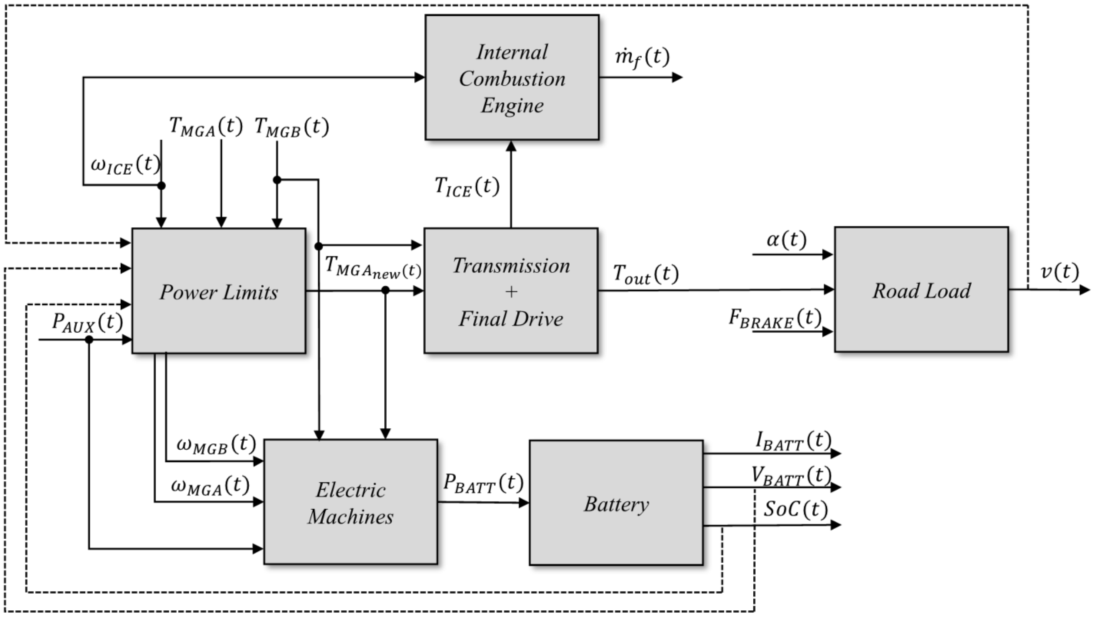

Figure 2.31: Updated Vehicle Simulator Block Diagram

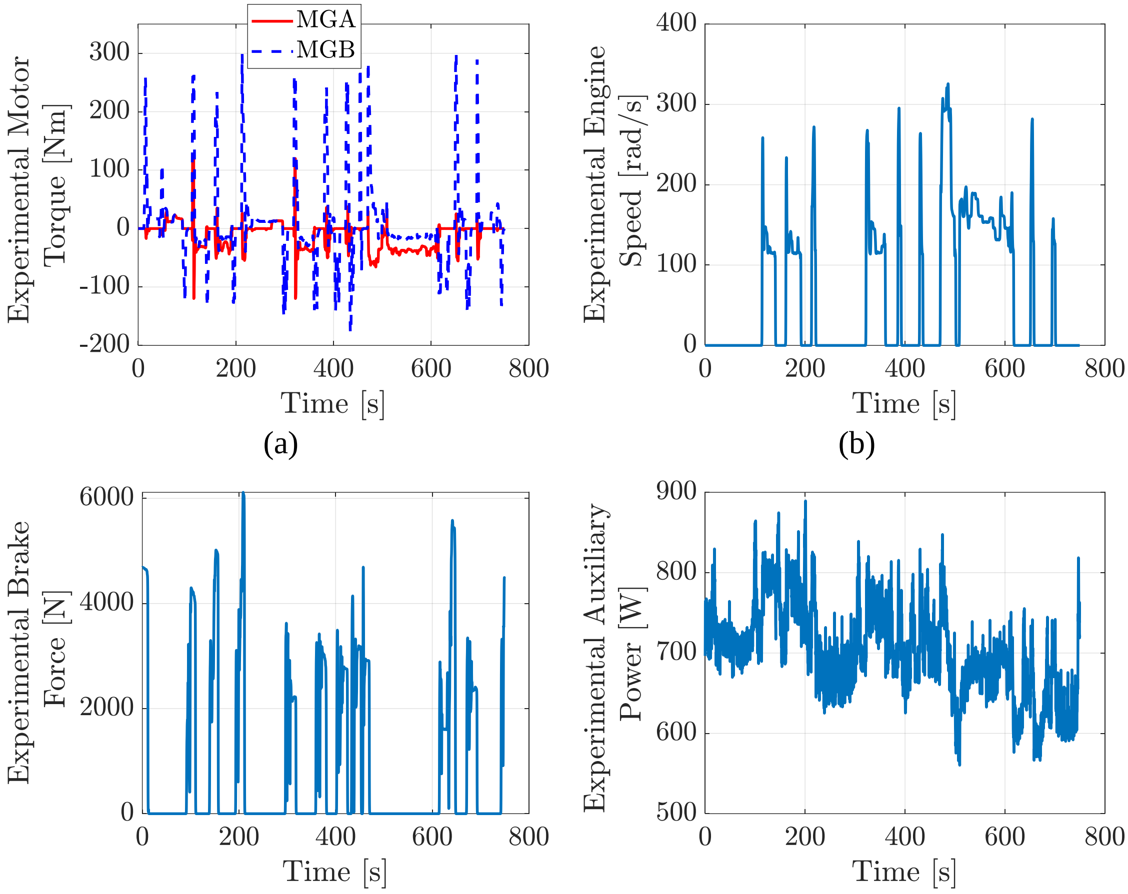

(a) (b)

(c) (d)

Figure 2.32: Experimental Inputs into the Vehicle Simulator for Validation using the Route 19 Cycle: (a) Motor Torques, (b) Engine Speed, (c) Brake Force, (d) Auxiliary Power

The simulated battery SoC, shown in Figure 2.33, follows the general trajectory of the data with an average error less than 1% SoC. Moreover, the charge sustaining behavior is captured with a negligible error as shown in the error distribution in Figure 2.33c. The predicted battery current, shown in Figure 2.34, follows the data with a normal error distribution approximately centered around zero error. The model predicted voltage, shown in Figure 2.35, captures the behavior in the data and shows a minimally shifted error distribution.

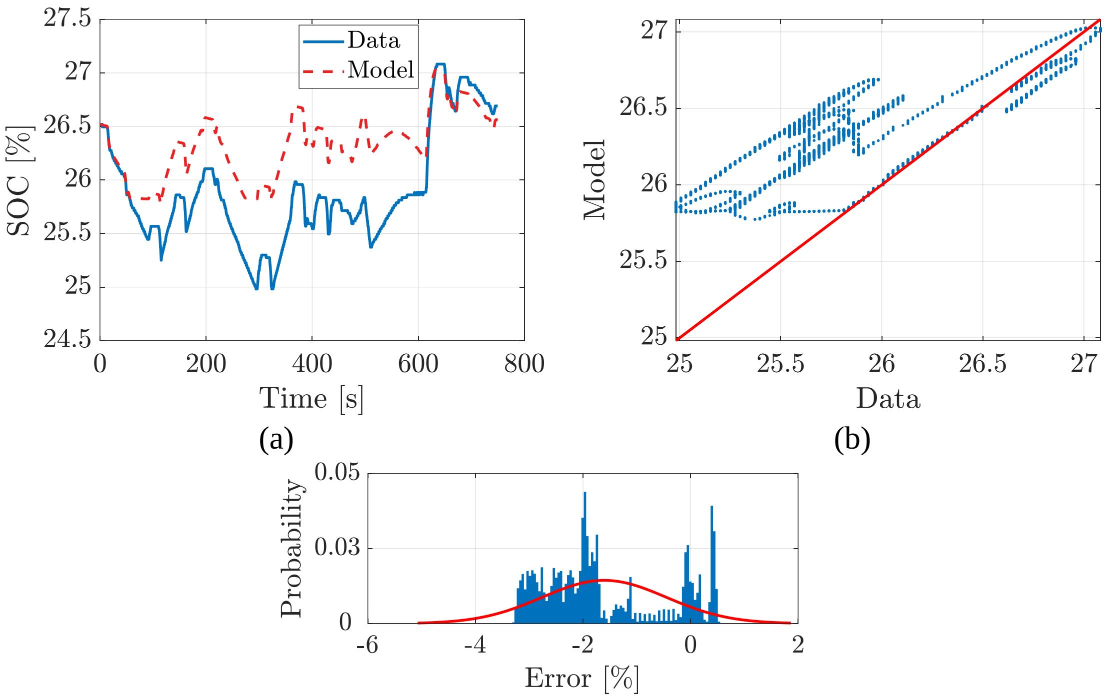

(a) (b)

(c)

Figure 2.33: Comparison of Actual vs Modeled Battery SoC for Validation: (a) Comparison of the Signals, (b) Correlation of the Signals, (c) Error Distribution

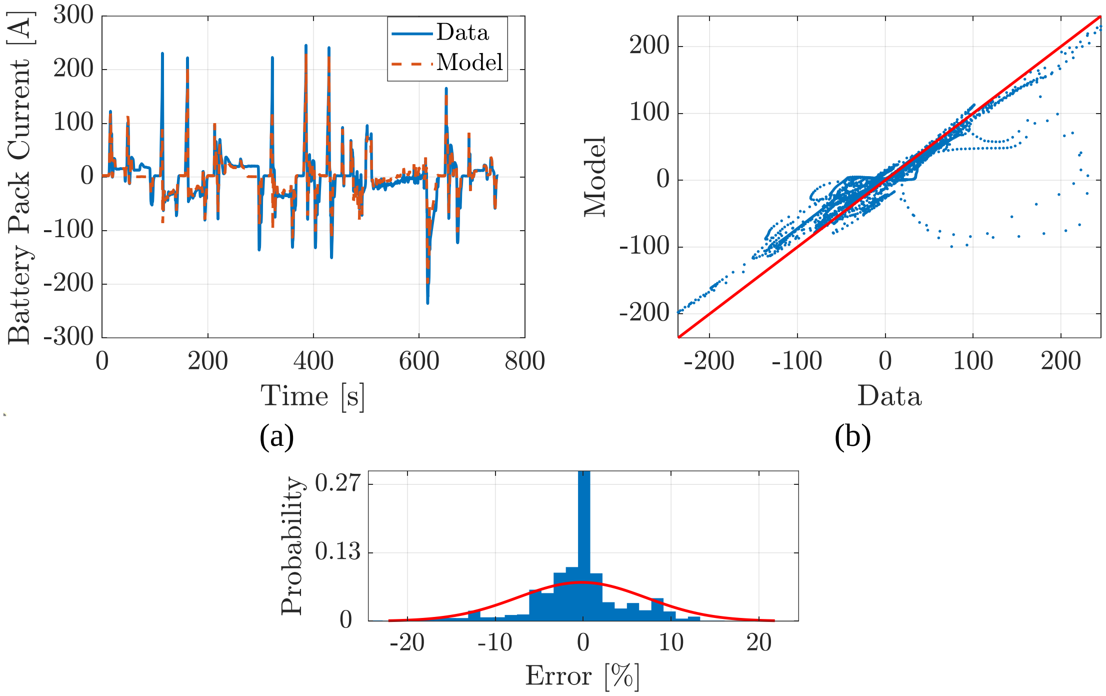

(a)

(b)

(c)

Figure 2.34: Comparison of Actual vs Modeled Battery Current for Validation: (a) Comparison of the Signals, (b) Correlation of the Signals, (c) Error Distribution

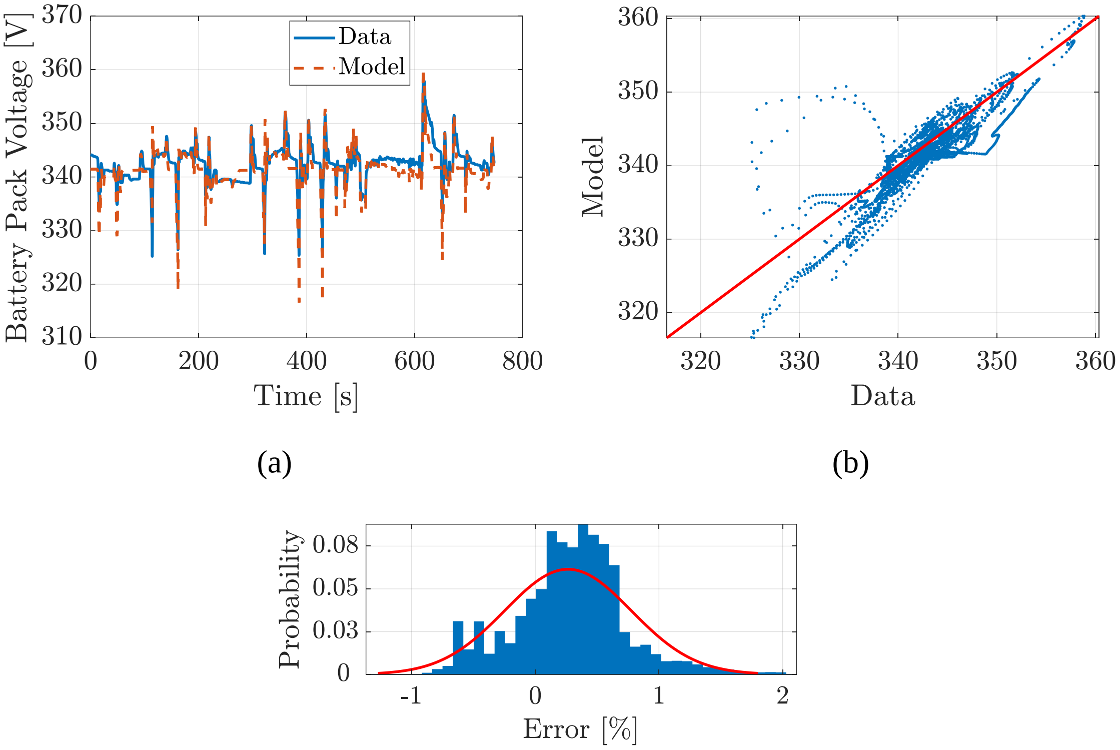

(a)

(b)

(c)

Figure 2.35: Comparison of Actual vs Modeled Battery Voltage for Validation: (a) Comparison of the Signals, (b) Correlation of the Signals, (c) Error Distribution

The fuel consumption predicted by the model in Figure 2.36 shows a strong agreement with the data. The error distribution is centered around a zero mean and average error is 1.7%.

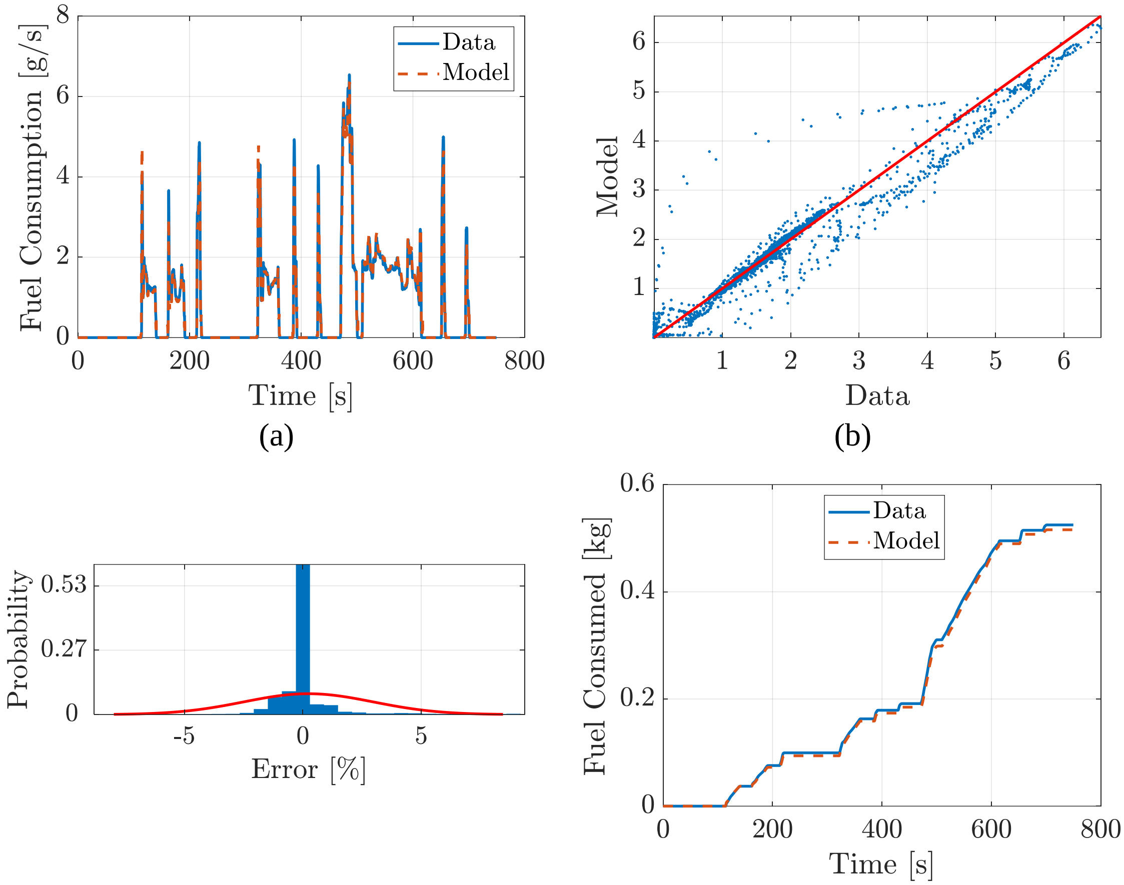

(a) (b)

(c) (d)

Figure 2.36: Comparison of Actual vs Modeled Fuel Consumption for Validation: (a) Comparison of the Signals, (b) Correlation of the Signals, (c) Error Distribution, (d) Comparison of Cumulative Consumption

The vehicle velocity is the final output of the vehicle simulator. The comparison between model and data shown in Figure 2.37 has good agreement. Some inconsistencies are observed, particularly at constant speed, but these errors are a result of the open-loop nature of the model.

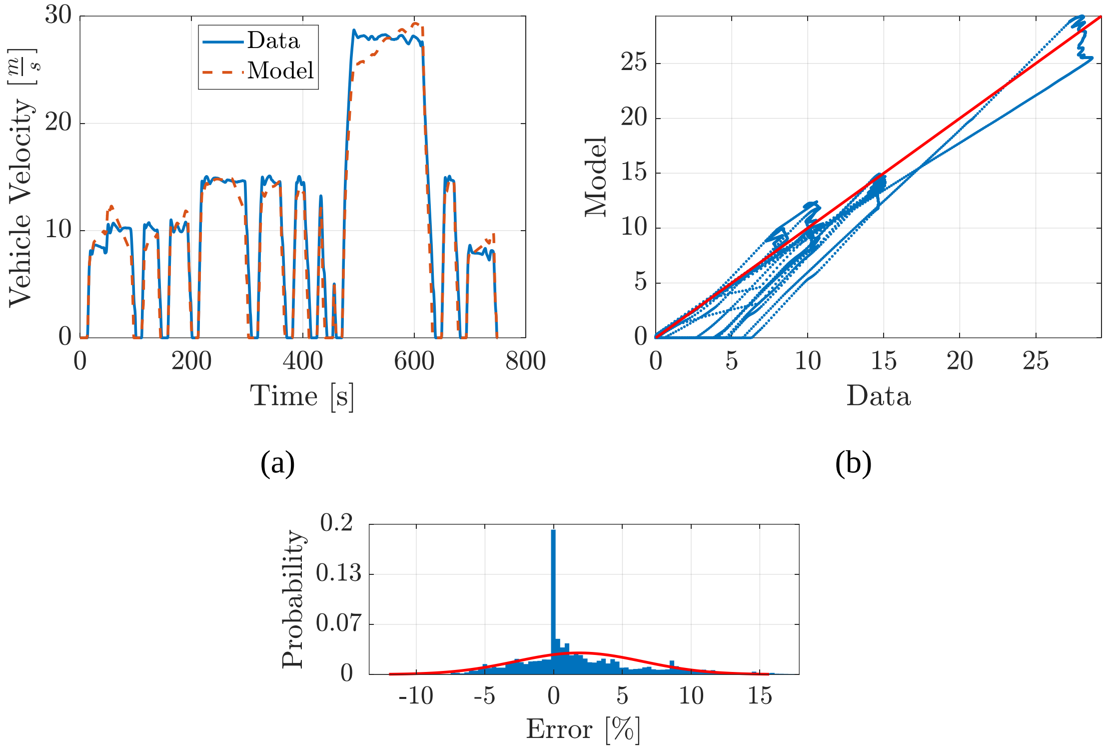

(a)

(b)

(c)

Figure 2.37: Comparison of Actual vs Modeled Vehicle Velocity for Validation: (a) Comparison of the Signals, (b) Correlation of the Signals, (c) Error Distribution

A summary of the model validation is shown in Table 2.4, where total fuel, battery energy and total equivalent energy are compared for 25 real-world cycles. The total battery energy and total energy consumption are calculated as:

$$Battery\ Energy\ [kWh] = \frac{\int_0^T P_{BATT,new}\, dt}{3.6 \cdot 10^6} \tag{2.36}$$

$$Total\ Energy\ [MJ] = \frac{Fuel\ Consumed \cdot LHV + \int_0^T P_{BATT,new}\, dt}{10^6} \tag{2.37}$$

where LHV is the lower heating value of gasoline ($LHV = 42761\, J/g$) and it is used as the equivalence between electric power and fuel. The errors in battery energy consumption are calculated only for the CD cycles as engine usage is minimal. The errors in fuel consumption are calculated for the CS cycles as the difference in battery energy is negligible during these cycles.

Table 2.4: Vehicle Simulator Validation for All Experimental Real-World Routes

	EMS	**Driver**	**SoC$_0$ [%]**	**Dist [m]**	**Travel Time [s]**	**Fuel [g]**	**Battery Energy [kWh]**	**Total Energy [MJ]**	**Model Fuel [g]**	**Model Battery Energy [kWh]**	**Model Total Energy [MJ]**
Route19	**CD**	Aggr.	61.34	8885	725	127.4	1.60	**11.2**	113.3	1.59 (-1%)	**10.6 (-5%)**
			51.21	8813	726	257.8	1.01	**14.7**	234.9	0.99 (-2%)	**13.6 (-7%)**
		Norm.	86.74	8726	749	0	1.79	**6.4**	0	1.71 (-4%)	**6.2 (-3%)**
			69.82	8791	748	25.1	2.01	**8.3**	20.7	1.95 (-3%)	**7.9 (-5%)**
		Rel.	82.84	8619	773	0	1.80	**6.5**	0	1.71 (-5%)	**6.2 (-5%)**
			71.87	8681	774	0	1.78	**6.4**	0	1.70 (-4%)	**6.1 (-5%)**
	CS	Norm.	26.52	8744	749	524.8	-0.07	**22.2**	517.0 (-1%)	-0.03	**22.0 (-1%)**
			26.25	8702	749	481.7	0.01	**20.6**	482.4 (+0.1%)	-0.04	**20.5 (-0.5%)**
		Rel.	26.86	8729	775	416.5	0.08	**18.1**	435.3 (+5%)	0.11	**19.0 (+5%)**
			26.30	8650	774	454.6	0.02	**19.5**	462.2 (+2%)	0.01	**19.8 (+2%)**
Mixed Route 1	**CD**	Aggr.	75.36	10269	928	14.6	2.12	**8.3**	12.8	2.23 (+5%)	**8.6 (+4%)**
			63.05	10250	929	36.1	1.99	**8.7**	32.3	2.10 (+6%)	**9.0 (+3%)**
		Norm.	85.74	10119	960	0	2.08	**7.5**	0	2.07 (-0.1%)	**7.4 (-1%)**
			60.00	10032	959	55.9	1.87	**9.2**	42.0	1.92 (+2%)	**8.7 (-5%)**
		Rel.	59.34	10089	988	0	1.96	**7.1**	0	1.97 (+0.3%)	**7.1 (+0%)**
			45.54	10097	988	29.9	1.85	**8.0**	25.1	1.89 (+2%)	**7.8 (-2.5%)**
	CS	Aggr.	27.91	10236	929	464.4	0.42	**21.4**	448.4 (-3%)	0.31	**20.3 (-5%)**
			25.06	10209	929	577.7	-0.02	**24.6**	579.1 (+0.2%)	-0.16	**24.2 (-2%)**
		Norm.	26.42	10023	959	517.3	0.25	**23.0**	532.7 (+3%)	0.06	**23.0 (-0%)**
			25.42	10072	960	561.4	0.11	**24.4**	569.4 (+1%)	-0.12	**24.0 (-2%)**
		Rel.	25.62	10017	991	486.7	0.12	**21.2**	512.6 (+5%)	-0.06	**21.8 (+3%)**
			25.32	9988	990	501.3	0.11	**21.9**	527.2 (+5%)	-0.11	**22.2 (+1%)**
Mixed4	**CS**	Aggr.	26.69	85124	4261	4451.3	-0.15	**189.8**	4501.4 (+1%)	-0.11	**191.8 (+1%)**
		Norm.	27.15	84267	4367	4404.5	-0.08	**188.1**	4466.9 (+1%)	-0.19	**190.1 (+1%)**
		Rel.	26.64	84033	4477	4250.4	-0.09	**181.4**	4308.9 (+1%)	-0.20	**183.3 (+1%)**

As summarized in Table 2.4, over the 25 cycles, the developed model shows a maximum error in model predicted fuel consumed of 5%, a maximum error in model predicted battery energy consumed of 6%, and a maximum error in model predicted total energy consumed of 7%. This corresponds to an average absolute fuel consumption error of 2.2% over the 13 CS cycles and an average absolute battery energy consumption error of 2.9% over the 12 CD cycles. The average absolute error of the model predicted total energy consumption is 2.8% over all 25 cycles.

From the validation of the vehicle simulator on these real-world cycles, the calibrated model can be considered sufficient for the purpose of providing a baseline prediction of vehicle performance.

2.6 Conclusion

In this chapter, an energy-based model of the Chrysler Pacifica PHEV is introduced. The model is calibrated and validated through on-road vehicle testing over regulatory and real-world cycles. The process of instrumenting the vehicle and the routes chosen for vehicle testing is also described.

The data acquired during vehicle testing is used as input to the model for performing calibration and verification and to evaluate the model agreement on battery state of charge and fuel consumption. The calibration of the model was limited to the implementation of battery power limits and a scaling factor for fuel consumption.

The open-loop vehicle verification shows good agreement with the experimental data, with average fuel consumption, battery energy consumption, and total energy consumption errors below 3%.

Chapter 3 Vehicle Dynamics and Powertrain Optimization for a Plug-In HEV

In this chapter, the VD&PT problem for the Chrysler Pacifica is formulated as an OCP. Then, the problem is solved numerically and the results are compared against the baseline strategy.

3.1 Optimal Control Problem

3.1.1 Problem Formulation

The problem is discretized in space where the road is divided into N segments of equal length. The system is characterized by two states, namely state of charge and vehicle speed. Hence the discrete state vector is:

$$x_k = [SoC_k, v_k]^T \in \mathcal{X} \subset \mathbb{R}^2 \tag{3.1}$$

The discrete state dynamics is defined by:

$$x_{k+1} = f_k(x_k, u_k), \qquad k = 0, 1, \dots, N-1 \tag{3.2}$$

where u_k is the control input at stage k and f_k is the dynamic of the system. The system dynamics follows from Section 2.2 and its discrete form will be addressed in the next section. The system can be considered as an MDP where the choice of the control input and the current value of the state determines the value of the next state. The control input u_k is given by the power of the engine and the acceleration:

$$u_k = \left[P_{ICE_k}, a_k\right]^T \in \mathcal{U} \subset \mathbb{R}^2 \tag{3.3}$$

These two control inputs are sufficient to characterize the system dynamics under a set of assumptions on the operating conditions. The power of the engine is used as an indicator of the vehicle operating mode and the assumptions are as follows:

- When $P_{ICE_k} > 0$, the vehicle operates in HEV mode and the engine operation is constrained to minimize fuel consumption.
- When $P_{ICE_k} = 0$, the vehicle operates in EV mode and the torque split between the two electric machines is constrained to minimize the total power drawn from the battery.

The objective of the VD&PT optimization is to find the control input u that minimizes the performance metric J defined as the tradeoff between equivalent energy usage and travel time:

$$J(u) = \sum_{k=1}^{N} g_k(x_k, u_k) = \sum_{k=1}^{N} \left(\gamma \frac{\dot{m}_{f,eq_k}}{\dot{m}_{norm}} + (1-\gamma)\right) dt_k \tag{3.4}$$

where $g_k(x_k, u_k)$ is the stage cost, $\dot{m}_{norm}$ is a normalization factor, γ is the weighting factor, and dt_k is the time increment. The equivalent energy consumption at stage k, denoted by $\dot{m}_{f,eq_k}$, is derived from both fuel and battery energy consumption:

$$\dot{m}_{f,eq_k} = \dot{m}_{f_k} + \frac{P_{batt_k}}{LHV} \tag{3.5}$$

The problem is then subject to state and input constraints:

$$\begin{cases} v_k \epsilon \left[0, v_{lim_k}\right], \forall k = 0, \dots, N-1 \\ SoC_k \epsilon [SoC_{min}, SoC_{max}], \forall k = 0, \dots, N-1 \\ SoC_N \epsilon [SoC_T, SoC_{max}] \\ a_k \epsilon [a_{min}, a_{max}], \forall\, k = 0, \dots, N-1 \\ P_{ICE_k}\, \epsilon \left[P_{ICE_{min}}, P_{ICE_{max}}\right], \forall\, k = 0, \dots, N-1 \end{cases} \tag{3.6}$$

where the vehicle speed is constrained to be within the route speed limits and the battery SoC is bound by manufacturer's constraints. A constraint on the terminal battery SoC prevents complete battery depletion at the end of a route. Additionally, P_{ICE_k} is constrained to the engine operation limits and a_k is subject to a lower and upper bound to ensure comfort and safety.

3.1.2 Discrete State Dynamics

The transmission and longitudinal vehicle dynamics equations outlined in Section 2.2 are discretized using Euler forward equations [82]. Additionally, they are rewritten in terms of the control inputs and modified to facilitate the inclusion of spatial constraints such as stops and traffic lights. First, the conversion process from time to space discretization is illustrated here for the velocity:

$$v = \frac{ds}{dt} \tag{3.7}$$

$$dt = \frac{ds}{v} \tag{3.8}$$

where ds is the space discretization and dt is the time discretization. The acceleration in the spatial domain can be found by substituting dt for Eq. (3.8):

$$a = \frac{dv}{dt} = \frac{dv}{\frac{ds}{v}} = v\frac{dv}{ds} \tag{3.9}$$

Using a temporary variable $p = v^2$, the acceleration can be rewritten using the power rule for derivatives to convert Eq. (3.10) to Eq. (3.11):

$$\frac{dv^2}{ds} = \frac{dp}{ds} \tag{3.10}$$

$$2v\frac{dv}{ds} = \frac{dp}{ds} \tag{3.11}$$

Hence:

$$a = v\frac{dv}{ds} = \frac{1}{2}\frac{dv^2}{ds} \tag{3.12}$$

Eq. (3.12) is then discretized using a Euler forward method with a constant step size $ds = 10\ m$. The velocity at the next stage $k + 1$ can therefore be calculated using the acceleration control input and the speed at stage k:

$${v_{k+1}}^2 - {v_k}^2 = 2a_k\, ds \tag{3.13}$$

$$v_{k+1} = \sqrt{{v_k}^2 + 2a_k\, ds} \tag{3.14}$$

The time increment dt_k in Eq. (3.8) is then defined based on the average speed:

$$dt_k = \frac{2\, ds}{v_k + v_{k+1}} \tag{3.15}$$

which is also used to determine wheel speed:

$$\omega_{wheel_k} = \frac{v_k + v_{k+1}}{2R_{wheel}} \tag{3.16}$$

Given the acceleration and velocity at stage k, the traction force can be calculated under the assumption that the road grade is known a priori. Provided with traction force, the wheel torque can then be determined:

$$F_{trc_k} \ = \ a_k M_{eq} + A + Bv_k + C{v_k}^2 + M_{eq} g \sin \alpha_k \tag{3.17}$$

$$T_{wheel_k} \ = \ F_{trc_k} R_{wheel} \tag{3.18}$$

As stated in Section 3.1.1, the method in which the transmission equations are computed is dependent upon the engine power control input. In HEV mode, the engine is constrained to the optimal operating line (OOL) shown in Figure 3.1, which corresponds to an optimal engine speed and torque pair (ω_{ICE}, T_{ICE}) that minimizes fuel consumption for a given power.

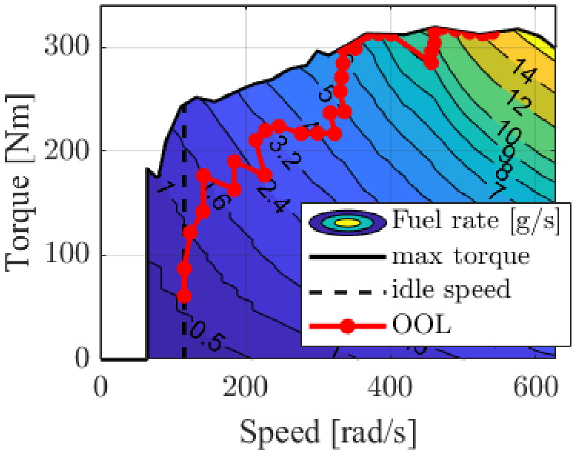

Figure 3.1: Engine OOL Illustration on the Engine Fuel Consumption Map

With the engine speed and torque pair, the losses modelled in Eq. (2.16) can be computed to obtain the output torque at the differential. Additionally, the transmission equations in Eq. (2.11) – (2.18) can be used to compute the speeds and torques of MGA and MGB:

$$T_{out_k} = T_{wheel_k} + \frac{P_{losses}(\omega_{wheel_k}, \omega_{ICE_k}, T_{wheel_k})}{\omega_{wheel_k}} \tag{3.19}$$

$$\omega_{MGB_k} = \frac{n_t}{n_B} \tau_{FD} \omega_{wheel_k} \tag{3.20}$$

$$\omega_{MGA_k} = \frac{n_S + n_R}{n_S} \omega_{ICE_k} - \frac{n_R}{n_S} \frac{n_t}{n_{\bar{R}}} \tau_{FD} \omega_{wheel_k} \tag{3.21}$$

$$T_{MGA_k} = -\frac{n_S}{n_S + n_R} T_{ICE_k} \tag{3.22}$$

$$T_{MGB_k} = \frac{n_B}{n_t} \left(\frac{1}{\tau_{FD}} T_{out_k} + \frac{n_R}{n_S} \frac{n_t}{n_{\bar{R}}} T_{MGA_k}\right) \tag{3.23}$$

In EV mode, T_{ICE_k} and ω_{ICE_k} are set to zero. The resulting calculations of the motor speeds are dependent upon the vehicle speed. Therefore, given the wheel torque T_{out_k} and vehicle speed v_k, the torque split of MGA and MGB can be computed using an offline map. Using Figure 3.2, the value of T_{MGA_k} that minimizes battery power is determined and T_{MGB_k} can then be found using Eq. (3.23).

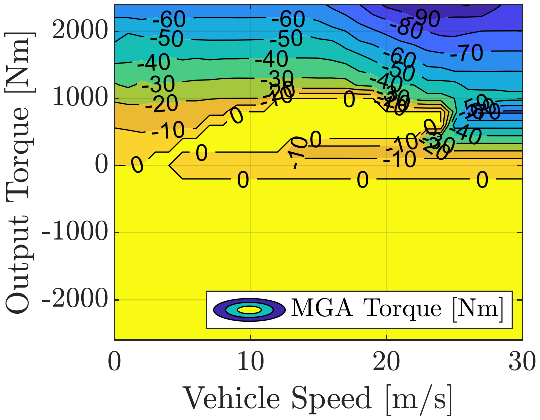

Figure 3.2: The Optimal MGA Torque Map

The torques and speeds are all saturated within the possible bounds of operation, where the torque bounds are dependent on the speed:

$$\omega_{ICE_k} \in \left[\omega_{ICE}^{idle}, \omega_{ICE}^{redline}\right] \cup \{0\} \tag{3.24}$$

$$\omega_{MGA_k} \in \left[\omega_{MGA}^{min}, \omega_{MGA}^{max}\right] \tag{3.25}$$

$$\omega_{MGB_k} \in [0, \omega_{MGB}^{max}] \tag{3.26}$$

$$T_{ICE_k} \in \left[0, T_{ICE}^{max}\left(\omega_{ICE_k}\right)\right] \tag{3.27}$$

$$T_{MGA_k} \in \left[T_{MGA}^{min}\left(\omega_{MGA_k}\right), 0\right] \tag{3.28}$$

$$T_{MGB_k} \in \left[T_{MGB}^{min}\left(\omega_{MGB_k}\right), T_{MGB}^{max}\left(\omega_{MGB_k}\right)\right] \tag{3.29}$$

If T_{MGB_k} exceeds T_{MGB}^{min} during regeneration, the excess torque is translated into mechanical braking which is computed by:

$$F_{brk_k} = \frac{1}{R_{wheel}}(T_{out_k} - \tau_{FD}\,(\frac{n_t}{n_B}T_{MGB}^{min}\left(\omega_{MGB_k}\right) - \frac{n_R}{n_S}\frac{n_t}{n_{\bar{R}}}T_{MGA_k}\,)) \tag{3.30}$$

From the following Eq. (3.13) - (3.30), the inputs into the block diagram in Figure 2.3 can be determined from the two control inputs of engine power P_{ICE_k} and acceleration a_k. The final input into the block diagram is auxiliary power P_{aux_k} which can be assumed a constant 600 W based on the experimental data. Using these assumptions of constant auxiliary power and the operations of the ICE, MGA, and MGB, the control inputs can be used to solve for all remaining variables in the model.

3.2 Solution Approach

The nonlinear optimization problem is then solved numerically using DP. Specifically, a generic MATLAB® function [83]. The *dpm.m* function requires the OCP to be discretized. The state and control variables in this case are discretized as follows:

- The vehicle velocity v_k grid has 31 discrete points every 1 m/s from 0 m/s to 30 m/s.
- The SoC_k grid is populated between 20% and 90% with 56 points and entries every 1.25%.

- The acceleration a_k is limited between $-3\ m/s^2$ and 2.4 m/s^2 and has 28 points that are $0.2\ m/s^2$apart.
- The engine power P_{ICE_k} is constrained between $0\ -\ 133\ kW$ and contains 20 points in the grid.

3.3 Route Results

The optimization problem is solved for Route 19, an urban driving cycle with stops displayed in Figure 2.13a. The solution is found for different values of γ representing different driver aggressiveness based on the Enhanced Driver Model (EDM) [84]. Specifically, solutions for an aggressive driver ($\gamma = 0.1$), a normal driver ($\gamma = 0.4$), and a relaxed driver ($\gamma = 0.7$) are obtained. Moreover, the results for three different initial state of charge values are included:

- $SoC_0\ =\ 70\%$: The high initial state of charge allows the vehicle to complete the entire route in EV mode. This trajectory results in charge depleting (CD) behavior.
- $SoC_0\ =\ 35\%$: This intermediate initial state of charge is optimal in exhibiting the effect of γ on the DP solution. The velocity trajectory results in a blended charge depleting – charge sustaining (CD-CS) behavior.
- $SoC_0\ =\ 26\%$: This value is also the minimum terminal state of charge, therefore the vehicle must exhibit charge sustaining (CS) behavior to satisfy this constraint.

The engine will need to be turned on throughout the route to maintain the charge and complete the route without violating constraints.

Charge Depleting Results ($\boldsymbol{SoC_0 = 70\%}$):

The solutions are similar for the different values of aggressiveness. Both the state of charge and speed only have minor deviations between $4000 - 8000\ m$ associated with the aggressive driver ($\gamma = 0.1$) shown in Figure 3.3. The battery depletes about 11% through the entire route with small charge/discharge peaks when the vehicle decelerates for a stop. MGA and MGB solutions for all three weighting factors are very similar as well with small deviations from the aggressive driver at about $4000\ m$ (Figure 3.4 and Figure 3.5). At this distance, the aggressive driver solution shows that the engine is activated to meet the acceleration demand and reduce travel time (Figure 3.6).

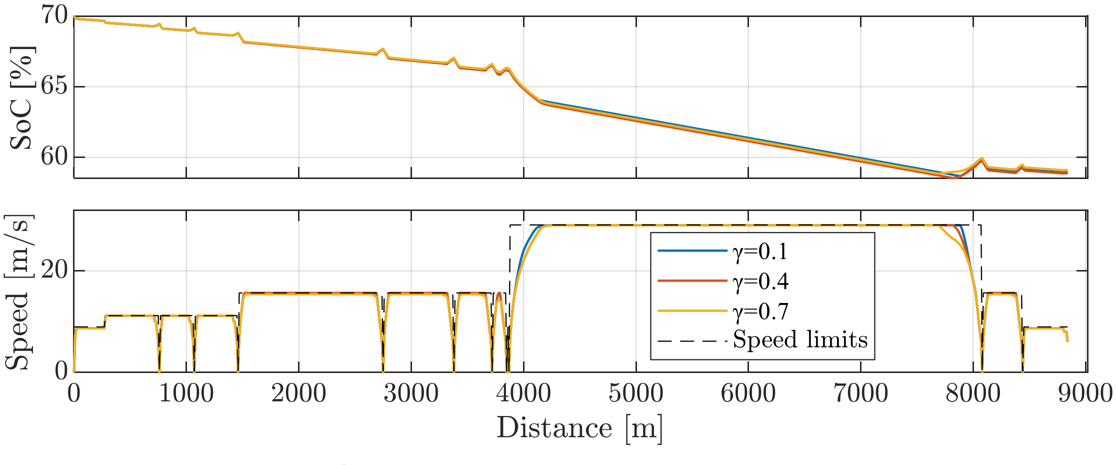

Figure 3.3: Battery State of Charge and Vehicle Velocity in Charge Depleting Strategy for an Aggressive, Normal, and Relaxed Driver.

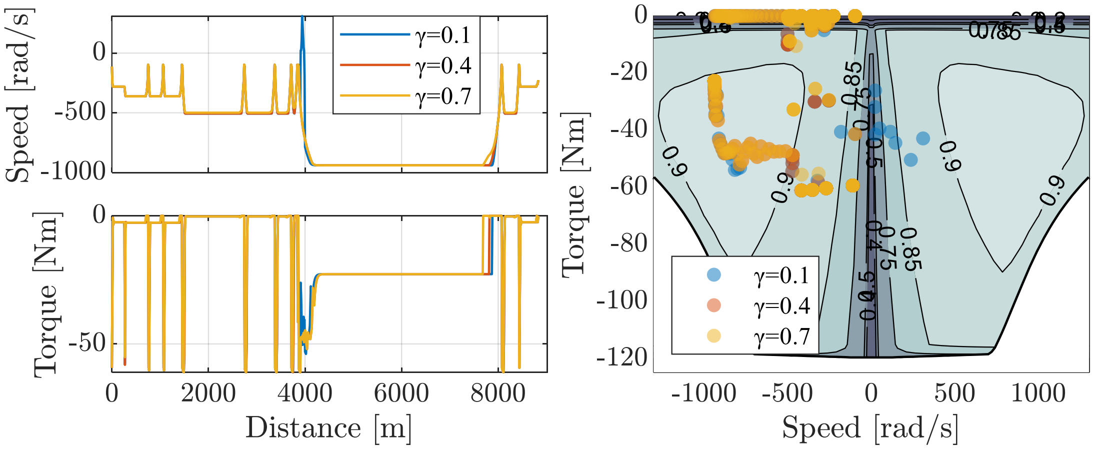

(a) (b)

Figure 3.4: MGA conditions for an aggressive, normal, and relaxed driver for charge depleting conditions (a) MGA speed and torque plots (b) MGA operational points on the efficiency map

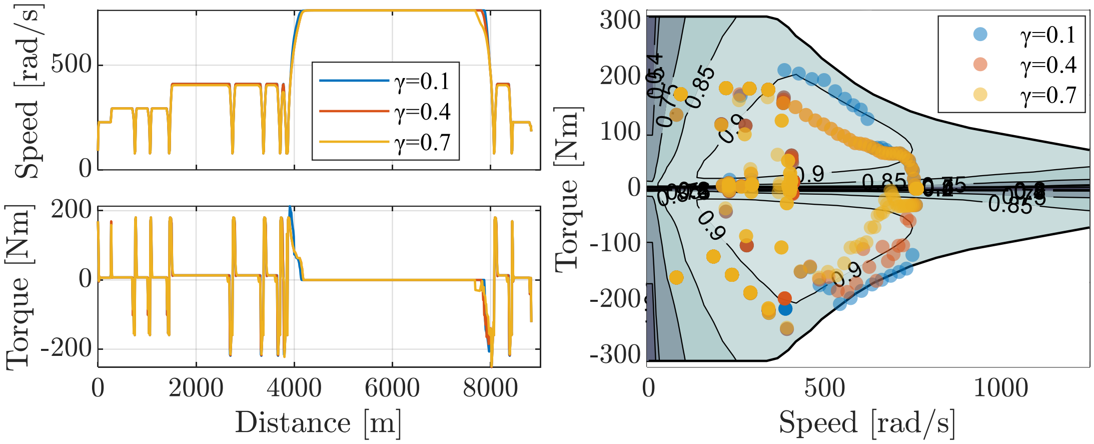

(a) (b)

Figure 3.5: MGB conditions for an aggressive, normal, and relaxed driver for charge depleting conditions (a) MGB speed and torque plots (b) MGB operational points on the efficiency map.

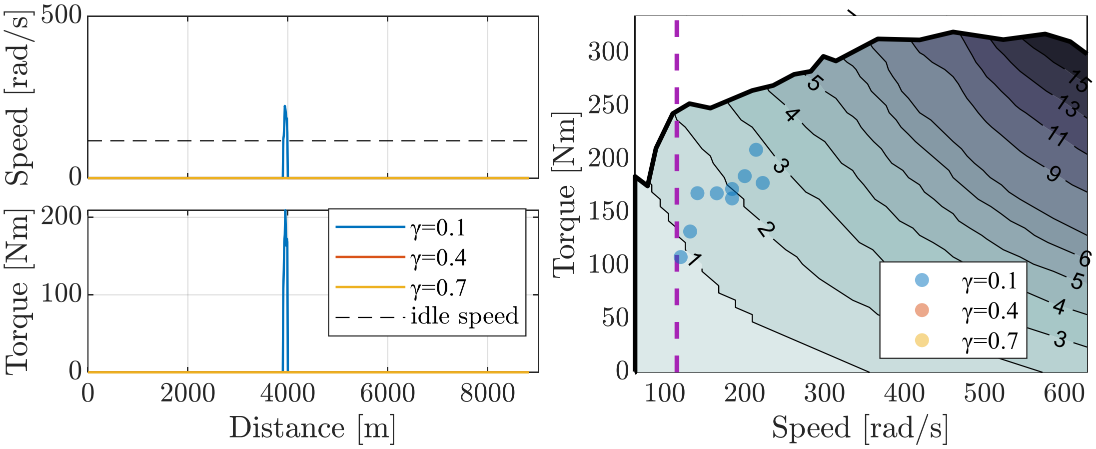

(a) (b)

Figure 3.6: ICE conditions for an aggressive, normal, and relaxed driver for charge depleting conditions (a) ICE speed and torque plots (b) ICE operational points on the efficiency map.

The Pareto fronts shown in Figure 3.7 are obtained by exploring different values of driver aggressiveness of $\gamma = 0.1$ to 0.9 for each initial SoC run. From left to right, the driver aggressiveness ranges from most aggressive ($\gamma = 0.1$) to most relaxed ($\gamma = 0.9$). In the simulation study, the engine only turns on for the more aggressive runs. More relaxed settings show less electricity consumption correlated with a higher travel time.

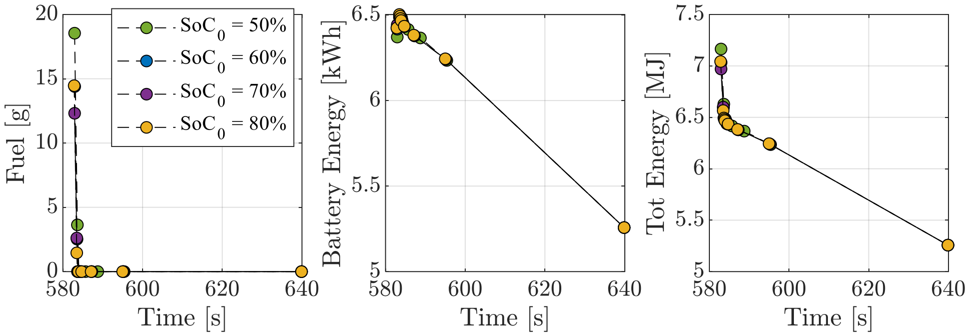

Figure 3.7: Pareto front of the DP results comparing the travel time vs energy consumed for weighting factors $\gamma = 0.1$ to 0.9 for four different initial SoC's in CD strategy

Charge Depleting - Charge Sustaining Results ($SoC_0 = 35\%$):

The CD-CS results show a larger variability in the state of charge and velocity trajectory between different weighting factors, shown in Figure 3.8. The $\gamma = 0.7$ run representing a relaxed driver consistently holds a lower velocity than the other runs which prevents the engine from turning on. In fact, as shown in Figure 3.11, the engine only turns on at the very end of the route to satisfy the minimum SoC constraint. Chattering in the MGA and MGB torques are shown in Figure 3.9 and Figure 3.10. This is because the on/off actuation of the motors is not penalized in the problem formulation since it would require an additional state. The three different runs have a very similar MGB torque profile with some variations in the speed due to the MGB being directly connected to the wheels. The baseline vehicle explained in section 2.5 would show a much more defined switch from a charge depleting to a charge sustaining strategy than the DP solution. This occurs because the DP solution allows the engine to turn on at any time in the route to ensure an optimal run, resulting in the desired blended strategy.

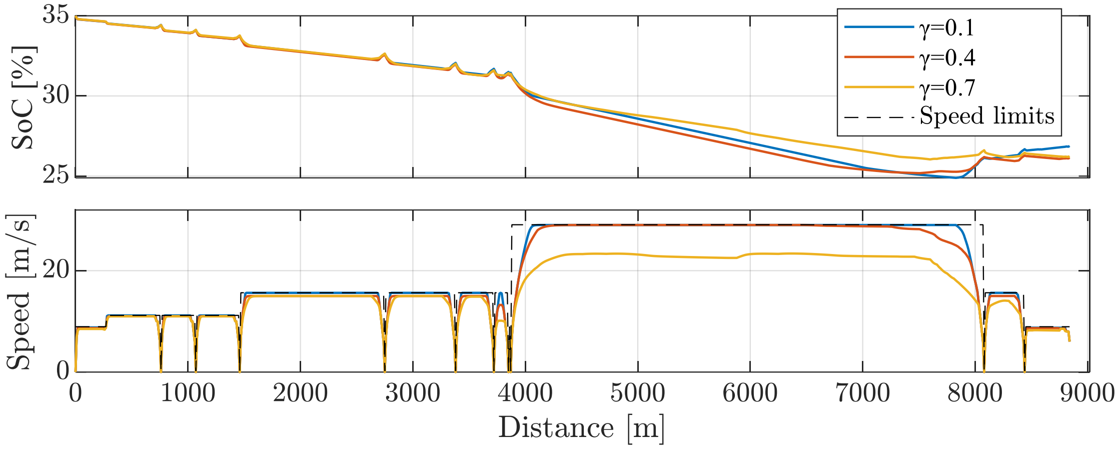

Figure 3.8: Battery State of Charge and Vehicle Velocity in CD-CS Strategy for an Aggressive, Normal, and Relaxed Driver.

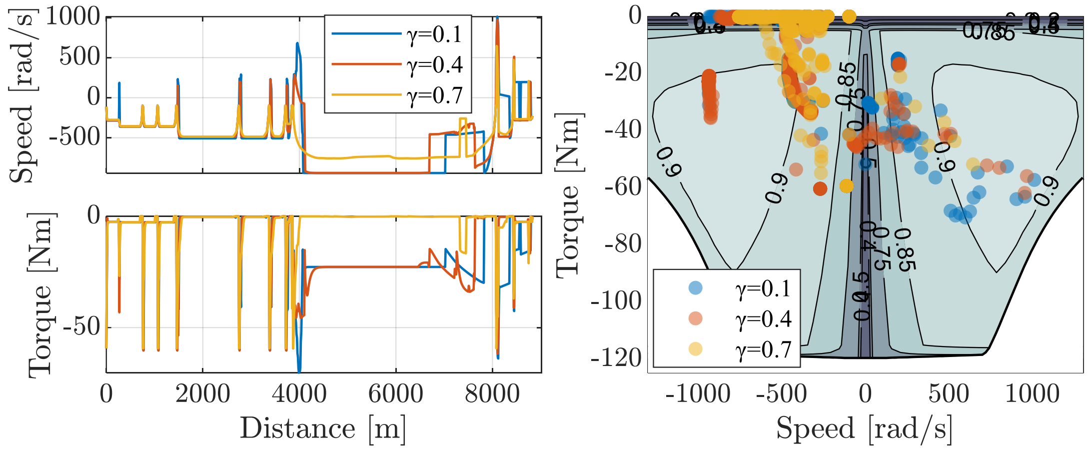

(a) (b)

Figure 3.9: MGA conditions for an aggressive, normal, and relaxed driver for CD-CS conditions (a) MGA speed and torque plots (b) MGA operational points on the efficiency map.

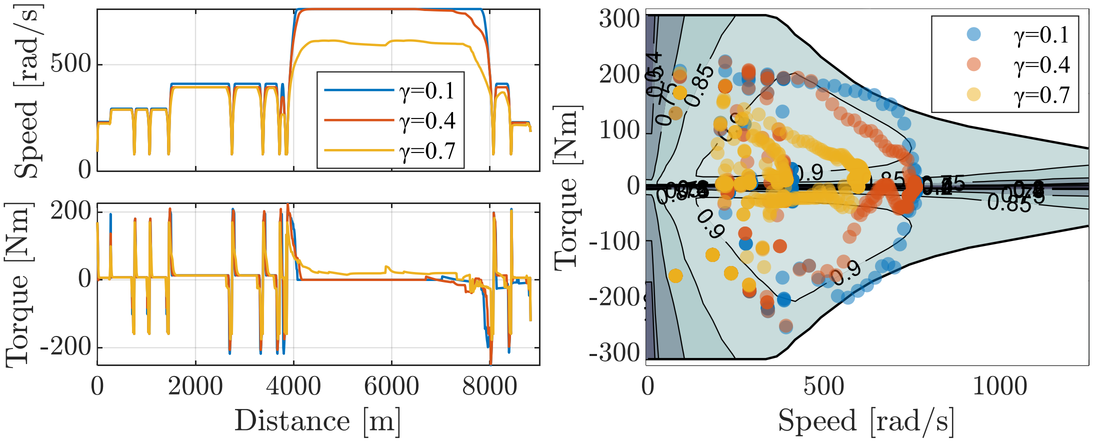

(a) (b)

Figure 3.10: MGB conditions for an aggressive, normal, and relaxed driver for CD-CS conditions (a) MGB speed and torque plots (b) MGB operational points on the efficiency map.

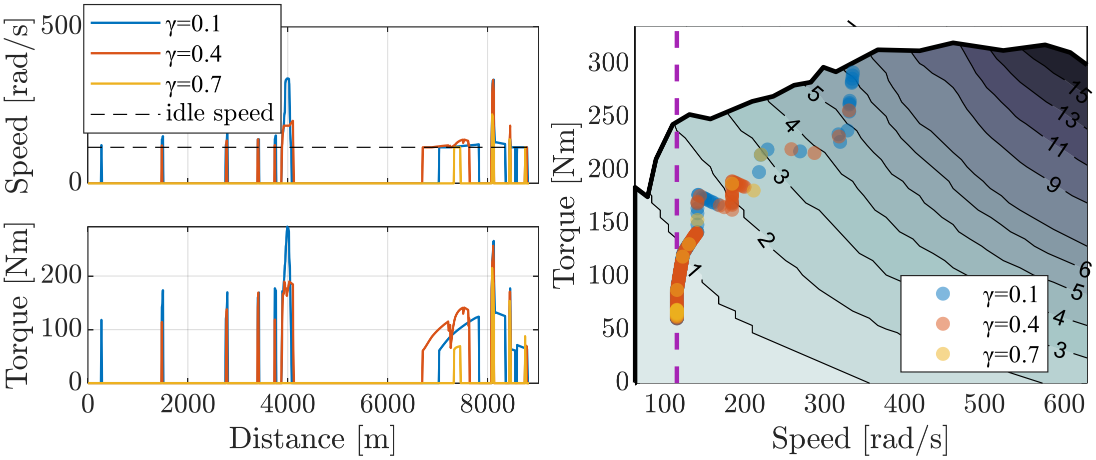

(a) (b)

Figure 3.11: ICE conditions for an aggressive, normal, and relaxed driver for CD-CS conditions (a) ICE speed and torque plots (b) ICE operational points on the efficiency map.

The Pareto front for three different initial SoCs is shown in Figure 3.12. The difference in the energy and time cost varies greatly between different values of γ. For low values of γ, the battery energy consumption increases with travel time as there is less opportunity for regenerative braking when the driver is less aggressive. For higher values of γ, velocity smoothing results in a decrease in battery energy with travel time. The solutions associated with a lower SoC_0 have less battery energy available and therefore use more fuel. Because of this, the velocity smoothing affects the fuel consumption more significantly than the battery energy for the 30% Pareto front.

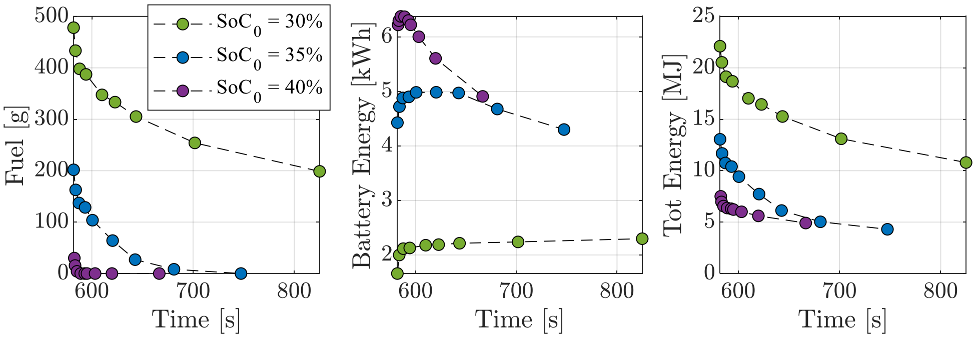

Figure 3.12: Pareto front of the DP results comparing the travel time vs energy consumed for weighting factors $\gamma = 0.1$ to 0.9 for three different initial SoC's in CD-CS strategy.

The conditions of MGA and MGB seen in Figure 3.14 and Figure 3.15 show a similar behavior across all weighting factors in the acceleration and braking regions with differences associated with the cruising region. The results of the engine in Figure 3.16 show higher actuation spikes for the more aggressive run. The engine operation points are distributed along the OOL.

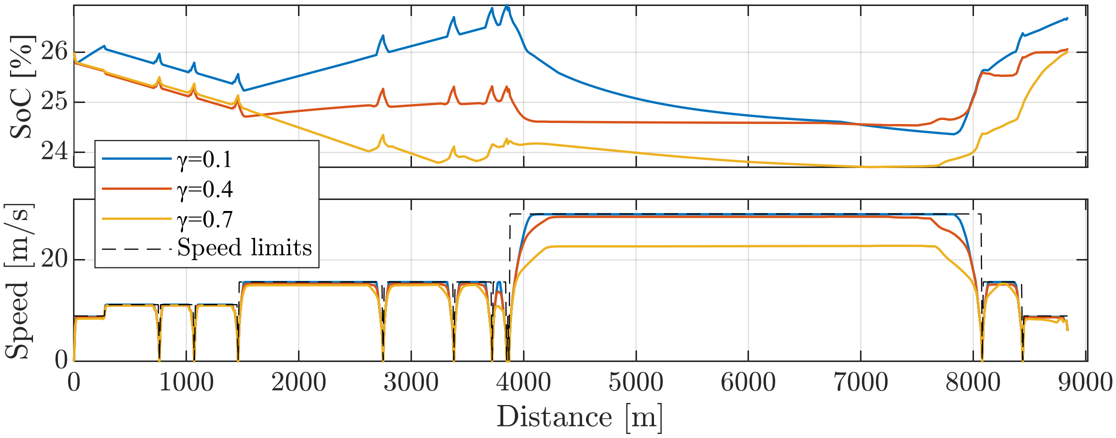

Figure 3.13: Battery State of Charge and Vehicle Velocity in CS Strategy for an Aggressive, Normal, and Relaxed Driver.

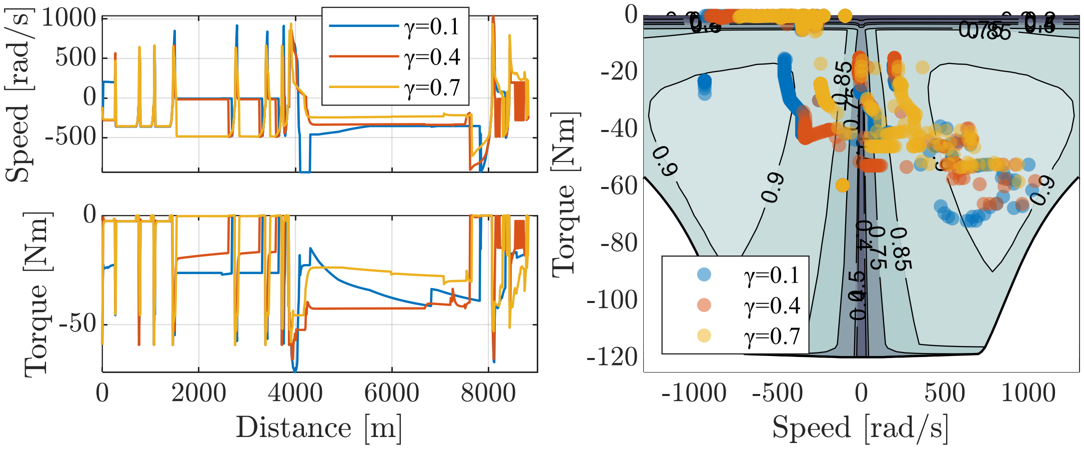

(a) (b)

Figure 3.14: MGA conditions for an aggressive, normal, and relaxed driver for CS conditions (a) MGA speed and torque plots (b) MGA operational points on the efficiency map.

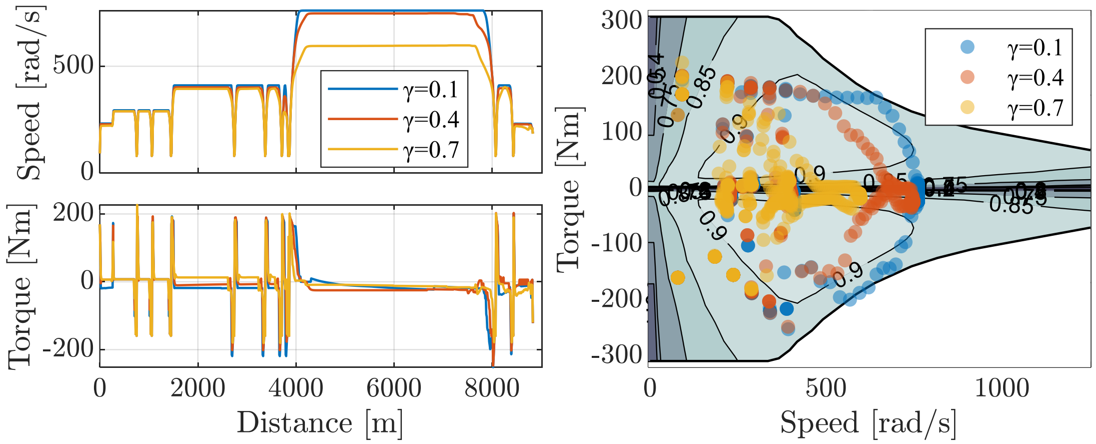

(a) (b)

Figure 3.15: MGB conditions for an aggressive, normal, and relaxed driver for CS conditions (a) MGB speed and torque plots (b) MGB operational points on the efficiency map.

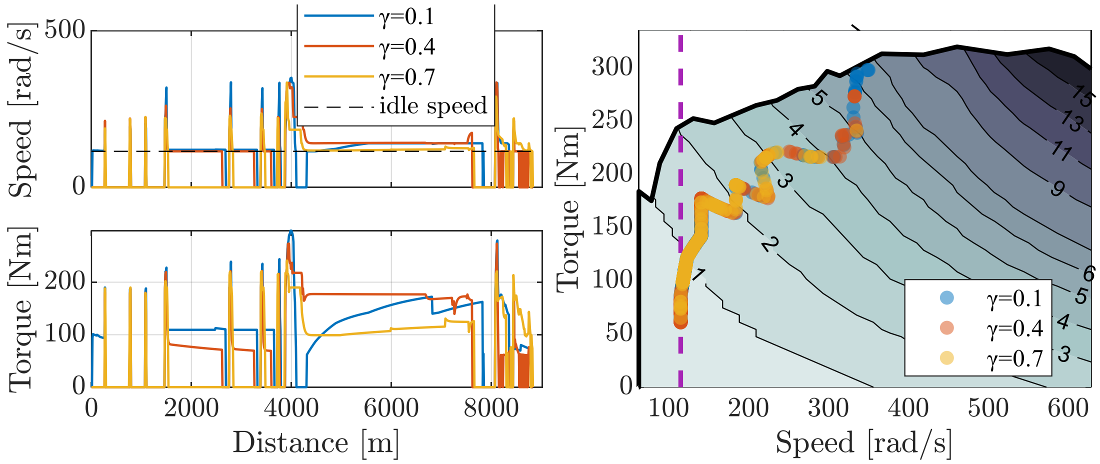

(a) (b)

Figure 3.16: ICE conditions for an aggressive, normal, and relaxed driver for CS conditions (a) ICE speed and torque plots (b) ICE operational points on the efficiency map.

Figure 3.17 displays the Pareto front for four different SoC_0's that span the operational region of the battery, with varying weights exhibiting the significance of the initial state of charge and the driver aggressiveness on the solutions. With a slightly increased SoC_0

to 35% all of the solutions use less fuel than the $SoC_0 = 30\%$ solutions. On the other hand, the $SoC_0 = 80\%$ Pareto shows less spread in the travel time for its weighted runs though the most relaxed driver uses significantly less battery energy than the aggressive driver. This supports the finding that an increased SoC_0 causes the solutions to collapse to a minimum energy consumption and travel time, showing a decline in the influence of driver aggressiveness. A summary of the results is reported in Table 3.1.

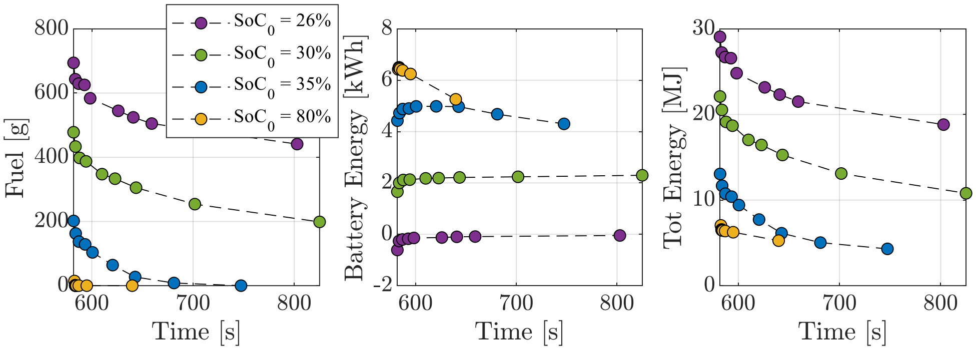

Figure 3.17: Pareto front of the DP results comparing the travel time vs fuel consumed for weighting factors $\gamma = 0.1$ to 0.9 for four different initial SoC's spanning all strategies.

Table 3.1. Summary of the cumulative cost for the three different SoCs analyzed for three different weighting factors.

Charge-Depleting (Initial SoC = 70%)				
γ – Driver	*Fuel consumed [g]*	*Battery Energy consumed [kWh]*	*Travel time [s]*	*Final SoC [%]*
0.1 – Aggressive	12.3	1.79	582.9	58.98
0.4 – Normal	0	1.80	583.9	58.91
0.7 – Relaxed	0	1.77	587.2	59.14
CD-CS (Initial SoC = 35%)				
γ – Driver	Fuel consumed [g]	Battery Energy consumed [kWh]	Travel time [s]	Final SoC [%]
0.1 – Aggressive	201.7	1.23	582.0	26.88
0.4 – Normal	128.6	1.36	593.3	26.15
0.7 – Relaxed	27.0	1.38	642.8	26.24
Charge-Sustaining (Initial SoC = 26%)				
γ – Driver	Fuel consumed [g]	Battery Energy consumed [kWh]	Travel time [s]	Final SoC [%]
0.1 – Aggressive	694.2	-0.17	581.9	26.70
0.4 – Normal	625.5	-0.05	592.7	26.08
0.7 – Relaxed	524.4	-0.03	640.9	26.04

To evaluate the energy benefits obtained from DP, the results are compared against the experimental data obtained using the production strategy (baseline). First, the value of γ is varied in simulation to match each route travel time in the experiments. The results of the comparison are summarized in Table 3.2. Over 25 cycles, the DP solution uses a maximum of 59% and average of 19% less total energy than the production strategy. The primary savings in CD mode derive from avoidance of engine turn on events. Velocity smoothing is the largest contributor to energy saving in CS modes. In CS modes, the change in battery energy is negligible as the battery is depleted in both cases. The DP solution decreases the fuel consumption during CS modes by a maximum of 22% and an average of 10%. As expected, the fuel savings decrease with a longer route. For example, Route 19 is much shorter than Mixed Route 4 and the energy savings are significantly larger. The DP solution decreases battery energy usage in CD modes by a maximum of 25% and an average of 8%.

Table 3.2: Comparison of DP Solution vs Experimental

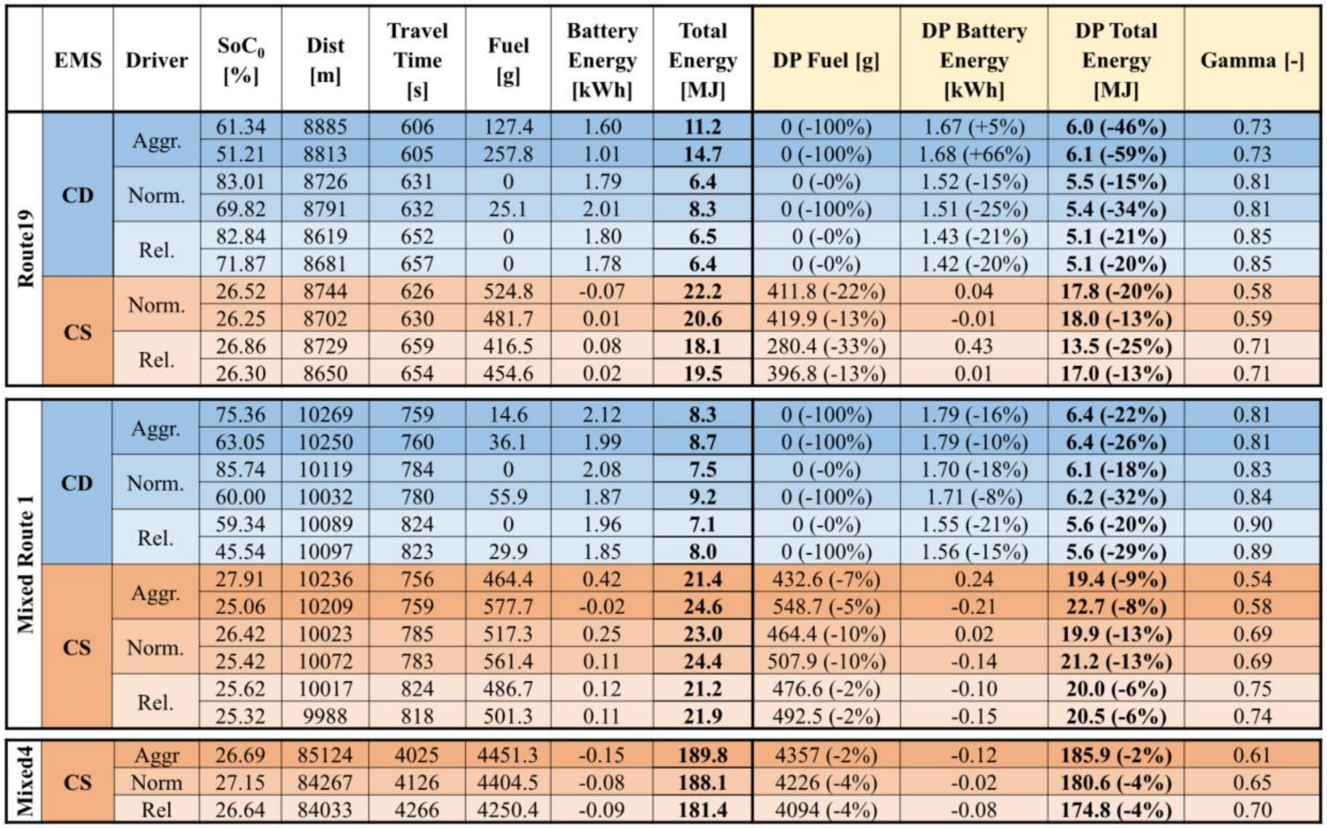

	EMS	Driver	SoC_0 [%]	Dist [m]	Travel Time [s]	Fuel [g]	Battery Energy [kWh]	Total Energy [MJ]	DP Fuel [g]	DP Battery Energy [kWh]	DP Total Energy [MJ]	Gamma [-]
Route19	**CD**	Aggr.	61.34	8885	606	127.4	1.60	**11.2**	0 (-100%)	1.67 (+5%)	**6.0 (-46%)**	0.73
			51.21	8813	605	257.8	1.01	**14.7**	0 (-100%)	1.68 (+66%)	**6.1 (-59%)**	0.73
		Norm.	83.01	8726	631	0	1.79	**6.4**	0 (-0%)	1.52 (-15%)	**5.5 (-15%)**	0.81
			69.82	8791	632	25.1	2.01	**8.3**	0 (-100%)	1.51 (-25%)	**5.4 (-34%)**	0.81
		Rel.	82.84	8619	652	0	1.80	**6.5**	0 (-0%)	1.43 (-21%)	**5.1 (-21%)**	0.85
			71.87	8681	657	0	1.78	**6.4**	0 (-0%)	1.42 (-20%)	**5.1 (-20%)**	0.85
	CS	Norm.	26.52	8744	626	524.8	-0.07	**22.2**	411.8 (-22%)	0.04	**17.8 (-20%)**	0.58
			26.25	8702	630	481.7	0.01	**20.6**	419.9 (-13%)	-0.01	**18.0 (-13%)**	0.59
		Rel.	26.86	8729	659	416.5	0.08	**18.1**	280.4 (-33%)	0.43	**13.5 (-25%)**	0.71
			26.30	8650	654	454.6	0.02	**19.5**	396.8 (-13%)	0.01	**17.0 (-13%)**	0.71
Mixed Route 1	**CD**	Aggr.	75.36	10269	759	14.6	2.12	**8.3**	0 (-100%)	1.79 (-16%)	**6.4 (-22%)**	0.81
			63.05	10250	760	36.1	1.99	**8.7**	0 (-100%)	1.79 (-10%)	**6.4 (-26%)**	0.81
		Norm.	85.74	10119	784	0	2.08	**7.5**	0 (-0%)	1.70 (-18%)	**6.1 (-18%)**	0.83
			60.00	10032	780	55.9	1.87	**9.2**	0 (-100%)	1.71 (-8%)	**6.2 (-32%)**	0.84
		Rel.	59.34	10089	824	0	1.96	**7.1**	0 (-0%)	1.55 (-21%)	**5.6 (-20%)**	0.90
			45.54	10097	823	29.9	1.85	**8.0**	0 (-100%)	1.56 (-15%)	**5.6 (-29%)**	0.89
	CS	Aggr.	27.91	10236	756	464.4	0.42	**21.4**	432.6 (-7%)	0.24	**19.4 (-9%)**	0.54
			25.06	10209	759	577.7	-0.02	**24.6**	548.7 (-5%)	-0.21	**22.7 (-8%)**	0.58
		Norm.	26.42	10023	785	517.3	0.25	**23.0**	464.4 (-10%)	0.02	**19.9 (-13%)**	0.69
			25.42	10072	783	561.4	0.11	**24.4**	507.9 (-10%)	-0.14	**21.2 (-13%)**	0.69
		Rel.	25.62	10017	824	486.7	0.12	**21.2**	476.6 (-2%)	-0.10	**20.0 (-6%)**	0.75
			25.32	9988	818	501.3	0.11	**21.9**	492.5 (-2%)	-0.15	**20.5 (-6%)**	0.74
Mixed4	**CS**	Aggr	26.69	85124	4025	4451.3	-0.15	**189.8**	4357 (-2%)	-0.12	**185.9 (-2%)**	0.61
		Norm	27.15	84267	4126	4404.5	-0.08	**188.1**	4226 (-4%)	-0.02	**180.6 (-4%)**	0.65
		Rel	26.64	84033	4266	4250.4	-0.09	**181.4**	4094 (-4%)	-0.08	**174.8 (-4%)**	0.70

3.4 Conclusion

This chapter covers the formulation of the OCP for the power split Chrysler Pacifica PHEV and analyzes the results of the optimization. The current results use the EPA recommended weighting between battery and fuel consumption, though further analysis can be performed with a varied equivalence factor. The real time factor of the algorithm is 3.

Chapter 4 Effect of Charging Behavior on Energy Consumption Study

4.1 Introduction

The simulation study shown in Chapter 3 is performed with the underlying assumption that the vehicle will be charged at the end of each route. Realistically, charging at the end of every route is not the case for the majority of PHEV users [85]. In the case that the vehicle runs multiple routes - possibly over multiple days - without charging, the optimal solution of a single route may become more conservative with battery energy usage.

For instance, Figure 4.1 outlines a simple weekly driving schedule with daily charging behavior. On Monday, the drive from home to work and then back home depletes the battery to 30%, considering the assumption that the daily routes fall within the AER of the vehicle. If a charging event does not occur after the Monday driving, the vehicle would be driving Tuesday’s routes starting with a 30% battery SoC. With a low initial SoC, the vehicle compensates for the lack of battery energy with fuel. An optimal SoC depletion for this two-day event may be a blended strategy, using some fuel on Monday to leave an adequate amount of battery energy for Tuesday’s driving and avoid CD operations.

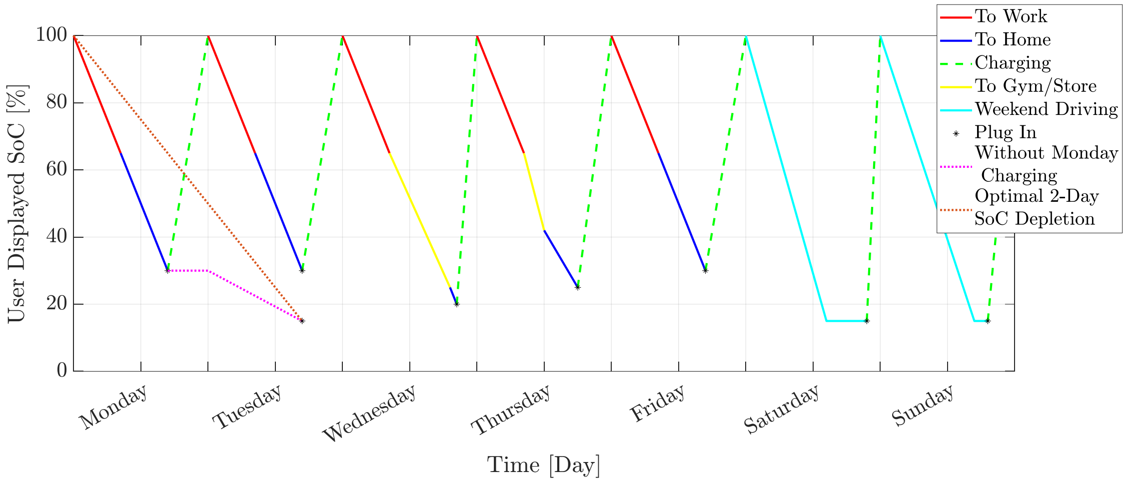

Figure 4.1: Representative Driving Schedule

This blended solution might alter the energy consumption of the vehicle and the travel time of the route. By broadening the horizon from a single route to an entire week of driving with many routes, this study aims to capture different and realistic charging behaviors to measure the effect of those behaviors on the vehicle energy consumption. The model of a PHEV developed in Chapter 2 and the optimizer developed in Chapter 3 are utilized to simulate a week of driving and measure the effect of varying charging behaviors on vehicle energy efficiency.

4.2 Study Framework

First, a weekly driving schedule representative of a normal week of driving is created for this study. Charging events are filled into the schedule with variations indicative of different charging behaviors. Provided the weekly routes remain constant, each week represents a different charging behavior. The following section provides the approach in creating the weekly route and the charging variations.

4.2.1 Representative Route Creation

The weekly route is created using real world routes and destinations in the Columbus, Ohio region representing both urban and mixed driving conditions. The schedule shown in Table 4.2 is typical of a working individual who commutes to work during the weekday and embarks on outings during the weekend. Overall, the weekly route totals an annual mileage of 12,713 miles which is comparable to the mean annual mileage of private PHEVs in US, Canada, and Germany totaling 13,608 miles [85]. According to the google maps travel time estimate of these routes during business hours, the weekly schedule averages 53 minutes spent driving each day. The recorded average travel time for individuals driving an LDV is 55.6 minutes [86], [87]. Using these metrics, the driving schedule can be considered a representative week of driving.

Table 4.1: Representative Weekly Driving Schedule

	Monday	Tuesday	Wednesday	Thursday	Friday	Saturday	Sunday
Locations	Home	Home	Home	Home	Home	Home	Home
	Work	Work	Work	Work	Work	Park	Grocery Store
	Home	Lunch	Physical Therapy	Lunch	Lunch	Home	Home
	Gym	Work	Work	Work	Work	Hardware Store	Event
	Home	Home	Home	Home	Home	Home	Home
		Gym		Pharmacy	Gym	Gym	
		Home		Home	Home	Home	

To minimize the number of unique routes used in the schedule, for each outbound trip there is a corresponding return trip. In total, the weekly schedule is comprised of nine unique round trips which can be previewed on OpenStreetMap (OSM), an open-source mapping tool in Figure 4.2 [88].

Figure 4.2: Map of Weekly Routes: (a) Home to Work, (b) Home to Hardware Store, (c) Home to Event, (d) Work to Lunch, (e) Work to Physical Therapy, (f) Home to Gym, (g) Home to Park, (h) Home to Grocery Store, (i) Home to Pharmacy [88]

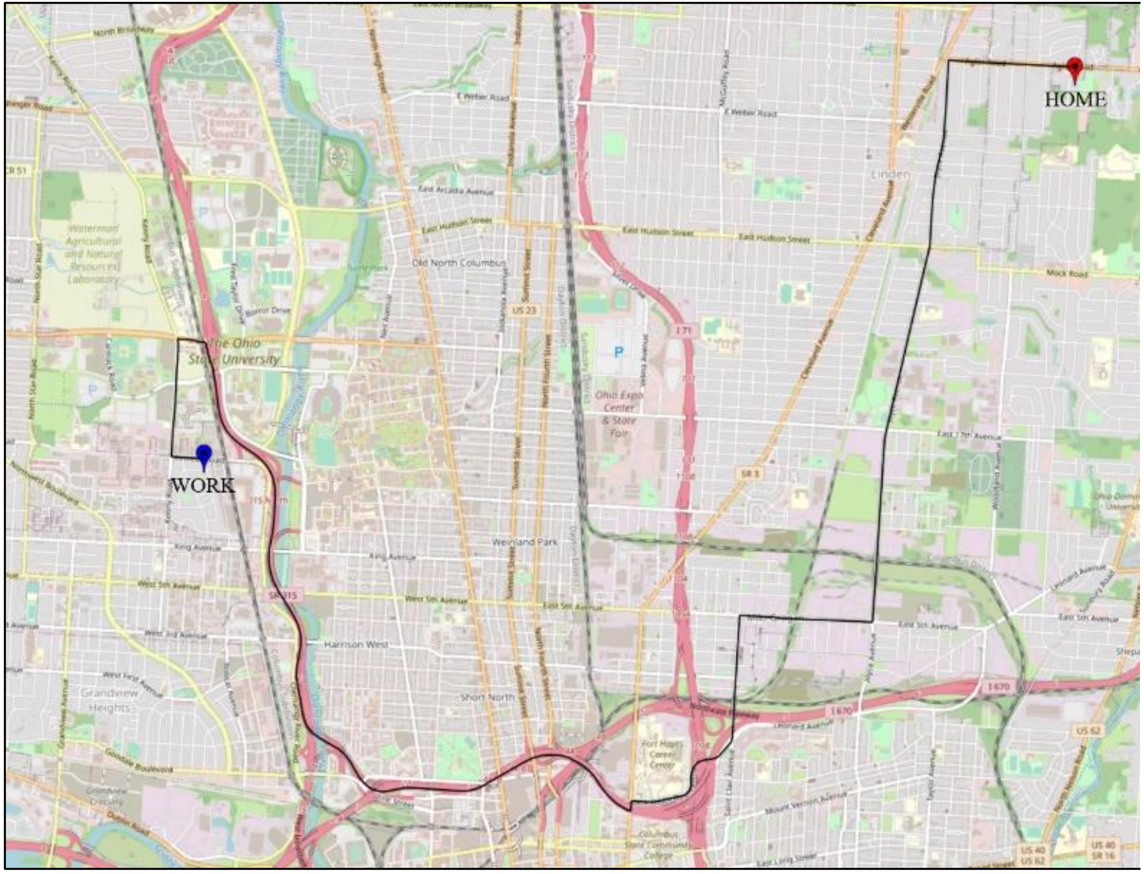

(a)

Figure 4.2: Continued

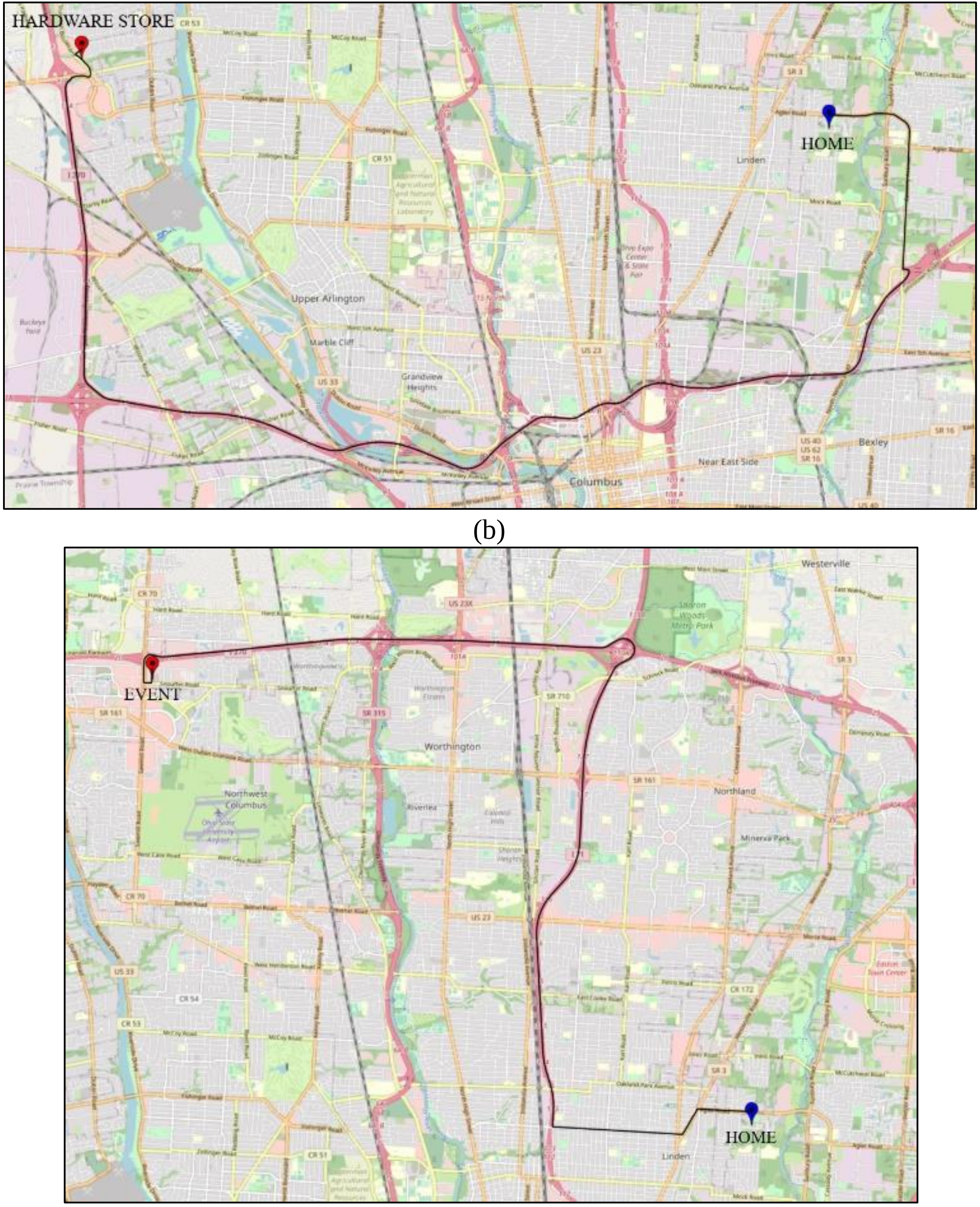

(b)

(c)

Figure 4.2: Continued

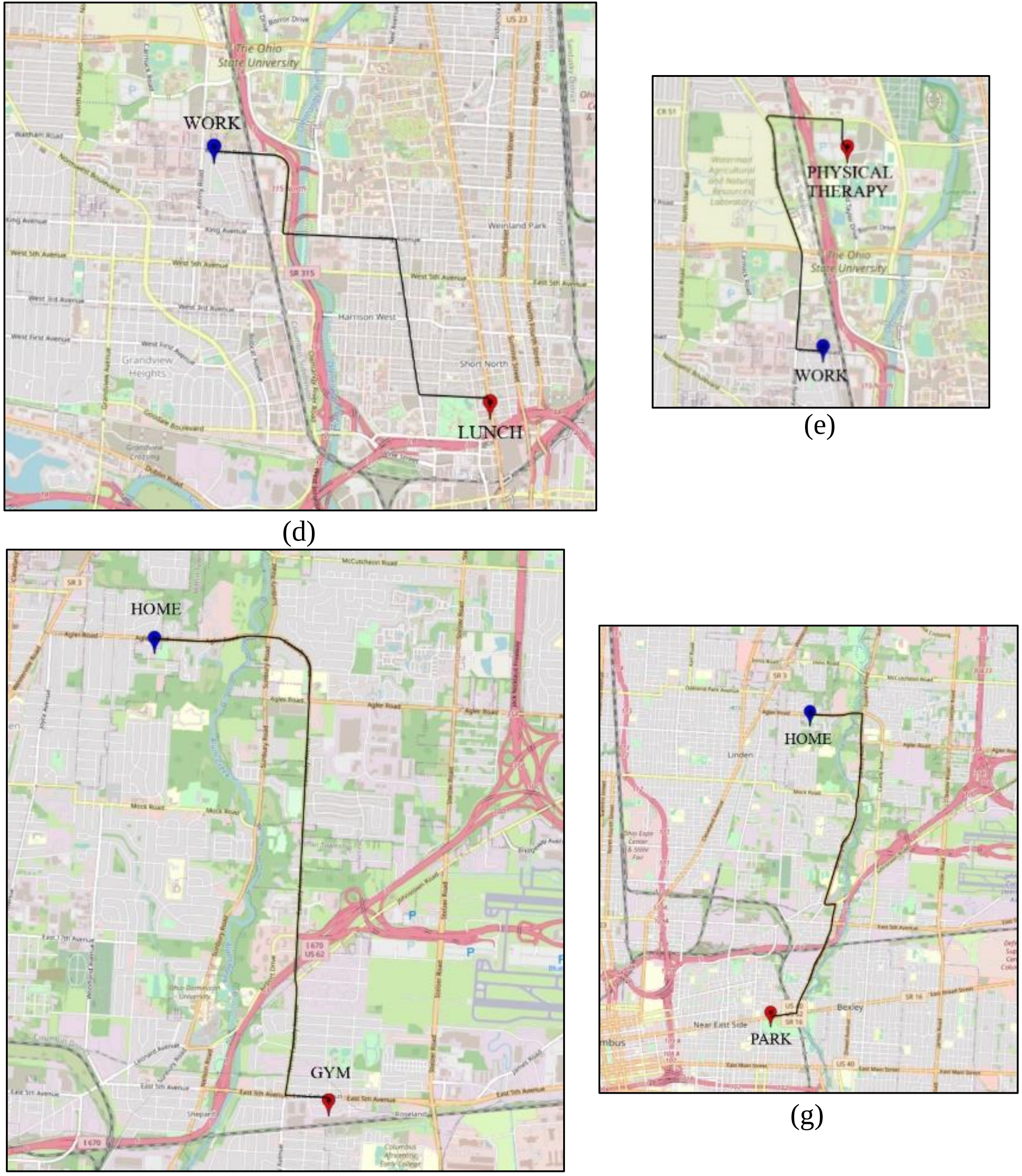

(d)

(e)

(f)

(g)

Figure 4.2: Continued

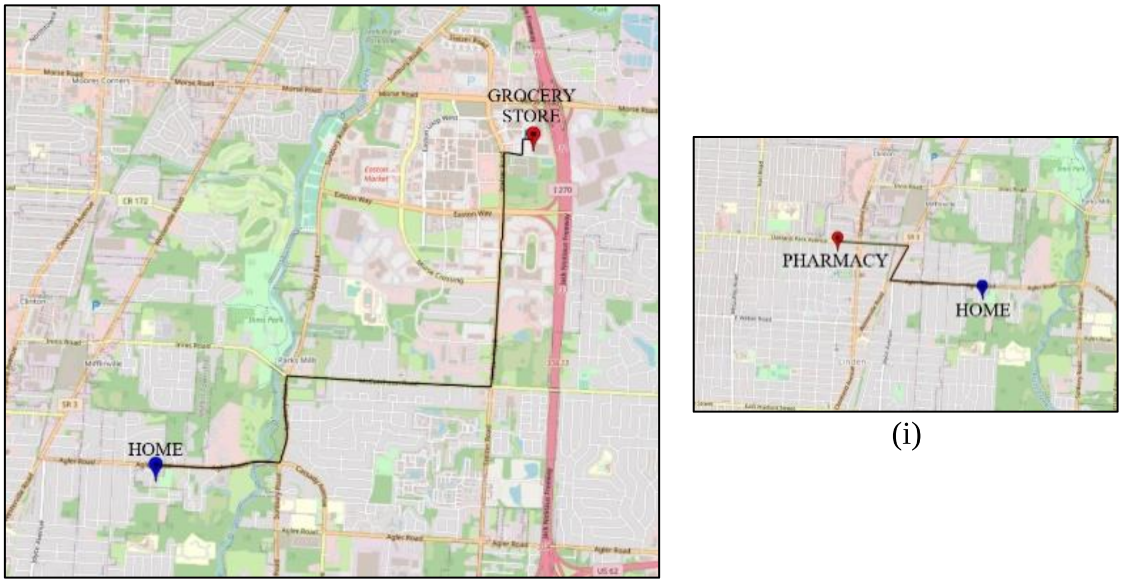

(h)

(i)

The individual routes in the weekly schedule are simulated using SUMO (Simulation of Urban MObility), an open-source simulation package that can model a single vehicle moving individually through a roadway network. The speed limits and stop signs along the route can be collected along with other route characteristics. The ability of SUMO to simulate traffic light changes is utilized to create different variations of the same route where the vehicle stops at different stop lights. To convert the routes collected from SUMO to be used for the study, all stops in the route are treated as stop signs. Therefore, the varying traffic light stops are integrated into the speed limits. For example, the Home to Work route shown in Figure 4.3, has five different variations where the vehicle stops at different combinations of stop lights. Therefore, the Home to Work route on Monday will have a different combination of stops on the route than the Home to Work route on

Tuesday, and so forth for the rest of the week. Additionally, traffic is omitted in SUMO to simplify the study.

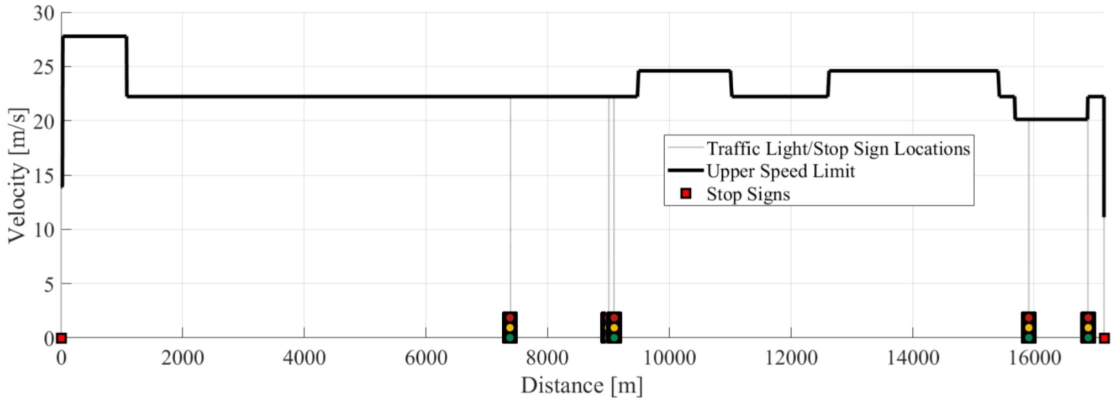

Figure 4.3: Home to Work Route Features

4.2.2 Charging Variation Approach

The methodology to create charging schedules has been developed using the charging behaviors found in literature [85], [89]-[92]. To determine the number of charging events for one week, n_{ch}, is chosen randomly between 1 and 11, representing the wide range of realistic charging behaviors [89]. According to [9], the most likely charging location for a PHEV user is at home followed by work. Therefore, for all weekdays it can be assumed that the representative PHEV user will charge either at home, work, or both locations. On the weekend, PHEV users can charge in public which includes at the park, hardware store, grocery store, and the event in the weekly schedule. Table 4.2 summarizes the probability that a user will charge at home, work, or in public depending on the day of the week.

Table 4.2: Probability of Charging Events per Location

Charging Location	Probability of Charging	
	Weekday	Weekend
p_{home}	0.53	0.83
p_{work}	0.47	-
p_{public}	-	0.17

The weekly charging events are determined using Algorithm 4.1. Here, n_{daily_ch} refers to the number of daily charging events.

Algorithm 4.1: Generate Charging Behavior

```
According to $n_{ch}$, randomly generate charging permutation for the week
foreach $day \in week$ do
    Generate $n_{daily\_ch}$ from charging permutation
    if $n_{daily\_ch} > 1$ then
        $bool_{charge\_home} \leftarrow TRUE$
        if $weekday$, $bool_{charge\_work} \leftarrow TRUE$ else $bool_{charge\_work} \leftarrow False$
        if $weekend$, $bool_{charge\_public} \leftarrow TRUE$ else $bool_{charge\_public} \leftarrow False$
    else if $n_{daily\_ch} == 1$ then
        $bool_{charge\_home} \leftarrow TRUE\ w/\ prob.\ p_{home}$
        $bool_{charge\_work} \leftarrow TRUE\ w/\ prob.\ p_{work}$
        $bool_{charge\_public} \leftarrow TRUE\ w/\ prob.\ p_{public}$
    else
        $bool_{charge\_home} \leftarrow FALSE$
        $bool_{charge\_work} \leftarrow FALSE$
        $bool_{charge\_public} \leftarrow FALSE$
    end if
    if $bool_{charge\_home} = TRUE$ then
        charge at home
    end if
    if $bool_{charge\_public} = TRUE$ then
        charge in public
    end if
    if $bool_{charge\_work} = TRUE$ then
        charge at work
    end if
end
```

For a public charging event, the location is decided between the public locations visited that day with equal probability. For example, if a charging event occurs in public on Saturday, either the park or the hardware store will be chosen as the charging location with equal probability. These rules for populating the charging variations allow a maximum of two charging events a day. Therefore, if a day does contain two charging events, one of those events is guaranteed to be at home. As a charging location may be visited multiple times in the same day, a standard is set for the charging event to occur after the vehicle visits the location for the final time that day. For example, if a charging event is to occur at home on Monday, the event is delegated to occur at the end of the day, after the Gym to Home route.

4.3 Simulation Setup and Outputs

Using the determined speed limit information from the representative route and the charging behavior, the route and initial SoC are used as the input into the VD&PT DP algorithm. The DP solver is run two different ways for each week, once to represent a realistic vehicle operation and a second time to run a collective set of routes assuming future knowledge of driving. The realistic run uses the Route by Route (R by R) technique in which each route is run individually (36 routes in the week indicates 36 subsequent runs of the DP). If the vehicle is not charged before a run, the initial SoC of that run equals the final SoC of the run before it. This technique mirrors a realistic experience where the only information known is the current route and the beginning SoC. Contrarily, the grouped run includes look-ahead information up until the next charging event. The routes in between charging events are concatenated and solved as a single route in DP. In this case, the initial SoC of the concatenated route is always fully charged. The information collected from both the R by R and grouped runs includes the initial and final SoC of each run, the computation time of the DP solver, travel time, distance, and fuel consumption. Additionally, resulting data indicative of the vehicle operation including the acceleration, motor torques, and engine speed is collected. With this information, the energy consumption and fuel economy can be calculated.

4.4 Preliminary Simulation Results

The simulation setup is verified first over three days of vehicle operation. Two charging events are generated for this sample result, one at work on Monday and another at home on Tuesday. A fully charged battery is assumed to be 70% SoC to ensure feasibility with respect to battery current limits. The aggressiveness factor is chosen as $\gamma = 0.3$, which weights the travel time heavily.

The test case is considered to begin with a fully charged battery. The resulting SoC trajectory, vehicle velocity, and total energy consumption for both the R by R and grouped runs of the sample week are shown in Figure 4.4. The green and magenta points demarcate the individual routes that comprise the sample. Additionally, the route names are abbreviated and annotated on the SoC trajectory plot to further distinguish the individual routes where: W = work, H = home, L = lunch, and PT = physical therapy. The route number that is annotated after the route name corresponds to the speed limit with the designated variation of stops. The difference in cumulative energy consumption between the R by R and grouped runs are annotated on the total energy consumption plot in Figure 4.4 for each charging occurrence and the final difference at the end of the sample. A positive difference indicates that the R by R energy consumption is greater than the grouped energy consumption.

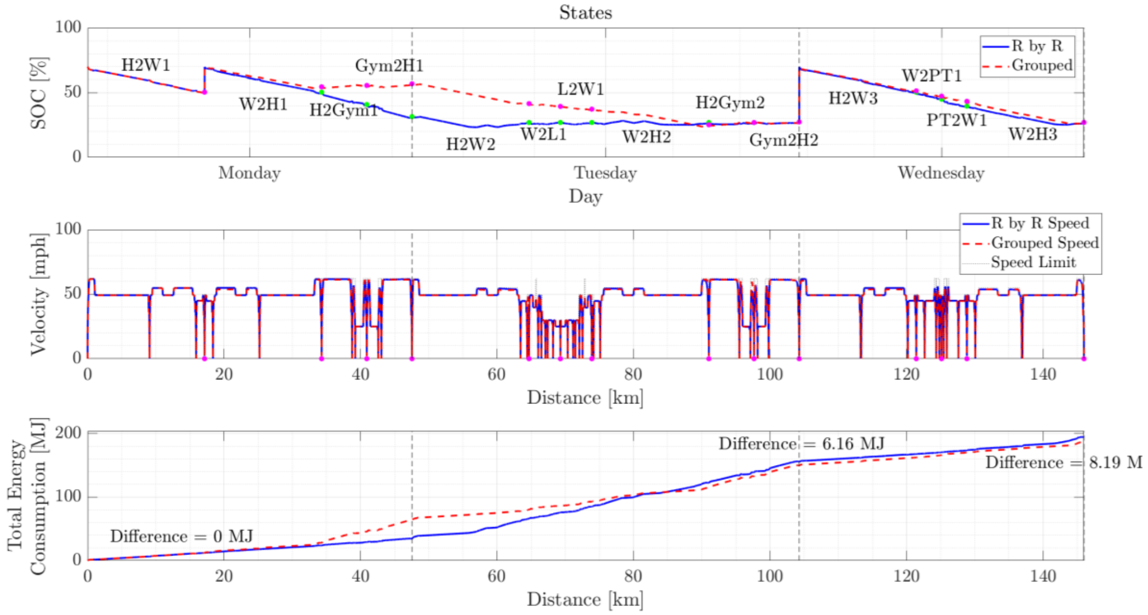

Figure 4.4: Sample Week Results Plot

The difference between R by R and grouped solution is evident between the first and second charge, approximately between 20 and 105 km. The R by R solution shows the battery initially depleting until the H2W2 route. This particular route is characterized by a blended SoC trajectory that gradually depletes the battery to the minimum SoC. The remaining routes between the H2W2 route and the next charging event show a charge sustaining behavior. As expected, the grouped solution shows a blended strategy the entire distance between the first and second charging events. This blended strategy follows a pattern of depleting then sustaining the battery using the engine. Despite the different SoC trajectories, the R by R and grouped solutions both result in a similar ending SoC after the Gym2H2 route.

Since the engine is, on average, less efficient than the electric machines, using fuel results in a larger loss of energy than using battery energy. Therefore, a vehicle using fuel to drive a set distance would deplete more energy than if the same vehicle used battery energy to drive the distance. In short, this reasoning explains the behavior of the energy consumption plot between the first and second charging event. The grouped energy consumption is higher than the R by R consumption until the R by R solution has depleted the battery. After the H2W2 route, the R by R sustains the SoC using the engine which significantly increases the energy consumption, surpassing the grouped energy consumption.

To inspect the vehicle velocity, the sample results are enlarged between 60 and 80 km in Figure 4.5. The R by R solution shows a higher velocity that is closer to the speed limit during constant high speeds, for instance around 62 km. During these constant speeds, the R by R SoC is increasing whereas the grouped SoC trajectory is decreasing. The R by R charge sustaining strategy involves using the engine both to provide traction to the vehicle and provide energy to charge the battery in comparison to the blended strategy of the grouped run. The grouped speed extends above the R by R speed during quick changes in speed (around 64.5 km), and sometimes has a larger deceleration at a later distance than the R by R solution (around 73.7 km).

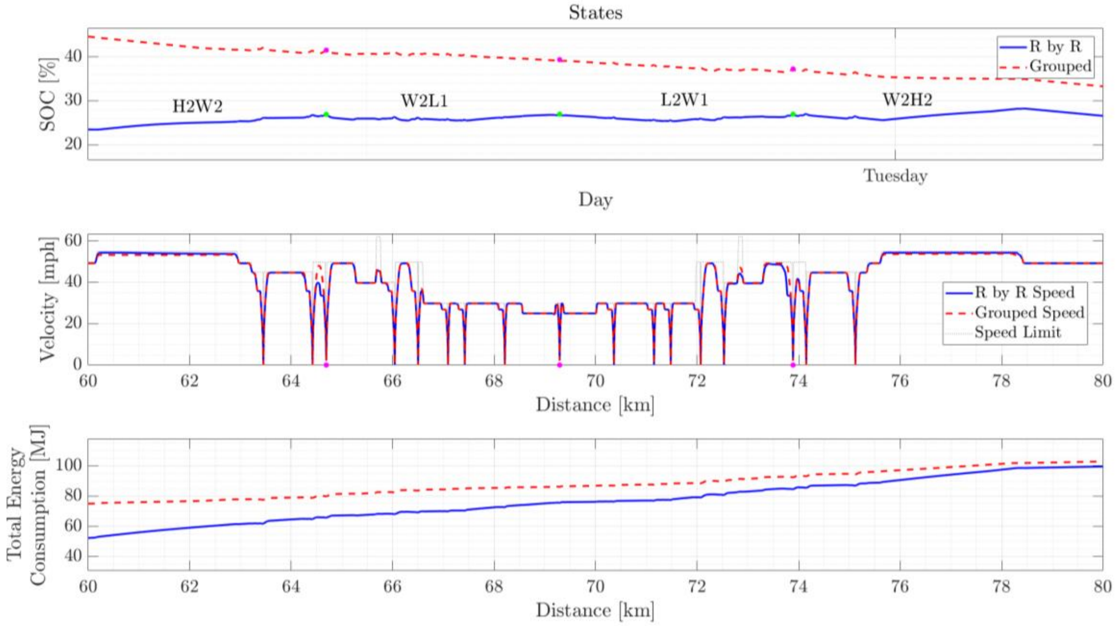

Figure 4.5: Enlarged Portion of Sample Results

Table 4.3 summarizes the distance, fuel consumed, battery energy consumed, and travel time of each route in the sample. Omitting the first route that was completed solely using electricity for both runs, the R by R solution for the routes immediately following a charging event only uses electricity whereas the grouped solution uses fuel for every route. Despite this difference, the total fuel consumed by the R by R is approximately 20% more than the grouped run fuel consumption. Considering the distances of each route, the R by R solution increasingly uses more fuel further away from a charging event. This is evident in the H2W2 route which uses around 30% less fuel than the W2H2 route later the same day. The two routes are the same distances, yet the fuel consumption deviation is significant. With the exception of H2W3, the grouped solution provides a faster travel time than the R by R solution. This can be attributed to the cost function in the optimization problem. The routes for the grouped runs are longer because they are a concatenation of multiple individual routes. A larger route inherently has a larger travel time and therefore will dominate more of the cost than if the optimal control problem was solved over one individual route. Despite this discrepancy, the maximum difference in travel time for one route is 5 seconds with a total difference of 14 seconds between the grouped and R by R runs for the sample.

Table 4.3: Sample Week Results Summary

Route	Distance [m]	Fuel Consumed [g]		Battery Energy Consumed [kWh]		Travel Time [s]	
		R by R	Grouped	R by R	Grouped	R by R	Grouped
H2W1	17150	0	0	3.2	3.2	789.8	786.9
W2H1	17150	0	151.9	3.2	2.6	790.0	786.4
H2Gym1	6620	2.8	430.5	1.4	-0.2	346.2	340.9
Gym2H1	6620	9.1	440.5	1.4	-0.2	346.5	340.8
H2W2	17150	679.6	181.6	0.69	2.5	791.5	790.2
W2L1	4600	234.1	118.9	-0.05	0.3	357.3	354.6
L2W1	4600	212.6	120.4	-0.03	0.3	360.0	355.5
W2H2	17150	882.2	343.3	-0.05	1.9	791.7	789.5
H2Gym2	6620	386.2	460.1	-0.03	-0.4	346.1	341.1
Gym2H2	6620	409.2	406.9	-0.1	-0.1	347.1	344.4
H2W3	17150	0	29.6	3.2	3.1	800.1	802.9
W2PT1	3710	0	38.1	0.8	0.6	222.7	219.8
PT2W1	3710	0	43.5	0.8	0.6	222.5	219.6
W2H3	17150	326.3	162.0	2.0	2.5	804.8	802.0
Sample Total	146000	3142	2927	16.5	16.8	7316	7302

Chapter 5 . Evaluating the Effect of Charging Behavior on Energy Consumption

5.1 Definition of Metrics

A large-scale simulation is performed to compare the effects of charging behavior on the energy consumption of a week-long route. Three specific charging behaviors are explored:

1. the number of charging events in the week defined as the charging frequency
2. the spread of the charging events throughout the route defined as the allocation of charging
3. look-ahead route information such as availability of charging and route speed limits, represented by comparing the R by R and grouped runs

For a comprehensive comparison, two metrics are defined to represent the fuel economy. The MPG of a vehicle is commonly used in the automotive industry to attract consumers. For PHEVs, the miles per gallon equivalent (MPGe) is the other relevant metric, which requires other energy sources to be converted to the equivalent fuel energy content [93]. For each week in the study, the MPG and MPGe can be calculated for a certain distance d:

$$MPG = \frac{d}{m_f} \tag{5.1}$$

$$MPGe = \frac{d}{m_f + m_e} \tag{5.2}$$

where m_f is the fuel consumed in gallons and m_e is the gallon equivalent of battery energy consumed found using the EPA equivalent conversion of $33.7\ kWh$ ↔ 1 gallon of fuel [94]. For one week, the fuel economy difference between the grouped and the R by R simulations is calculated as:

$$MPGe\ Gain = \frac{MPGe_{group} - MPGe_{R\ by\ R}}{MPGe_{group}} \cdot 100 \tag{5.3}$$

In addition to the fuel economy, the utility factor (UF) is commonly used in automotive reports to compare PHEVs for consumers and refers to the share of distance driven on electricity [85].

5.2 Case Study

The study involves generating variations of weekly charging behaviors and simulating the R by R and grouped runs for each variation. In total, 50 variations for each realistic charging frequency ranging from 1 to 11 charges per week are run. Further, extension to the study includes charging frequencies up to 36 charges per day to generate large scale trendlines for analysis. The aggressiveness factor for these runs stays constant at $\gamma = 0.3$. The initial SoC at the beginning of each week is 70%.

5.3 Results

The results of the realistic charging scenarios give insight into all three charging behaviors of charging frequency, allocation of charging, and knowledge of look-ahead information.

The effect of the charging frequency on the energy consumption is shown in Figure 5.1. As expected, the overall trend is that the weekly energy consumption decreases with a more frequent charging behavior. Replenishing the battery more frequently increases the battery energy available for use throughout the week; therefore, an increased availability of battery energy is correlated with a lower total energy consumption.

For a specific charging frequency and run (grouped or R by R), the charging allocations are varied. The effect of these charging allocations is represented in the spread of the boxplot. A larger spread indicates that the charging allocation has a larger influence in the energy consumption of a specific route, and vice versa. For example, charging 11 times a week could result in a range of energy consumption that spans around 100 MJ. The charging allocation determines where in this range the specific energy consumption for a run will fall.

The boxplot spreads are similar for the R by R and grouped runs, though the grouped run clearly achieves a lower weekly energy consumption than the R by R. Because the grouped run has access to look-ahead information and the R by R run does not, this shows that the knowledge of look-ahead information affects the energy consumption of the route. The effect of look-ahead information is investigated further in the energy savings plot in Figure 5.2. With knowledge of route information up until the next charging event, the grouped run is able to utilize the battery more efficiently and reduce fuel consumption. The median energy savings stays within 4 MJ for all realistic charging frequencies and the effect of look-ahead information peaks around 5 charges per week. On average, the horizon of look-ahead information provided to the grouped run decreases as charging frequency increases due to shorter regions in between charging events. Because energy savings are similar for varying frequencies, the existence of look-ahead information seems to make much more of a difference in energy savings than the horizon length of the information.

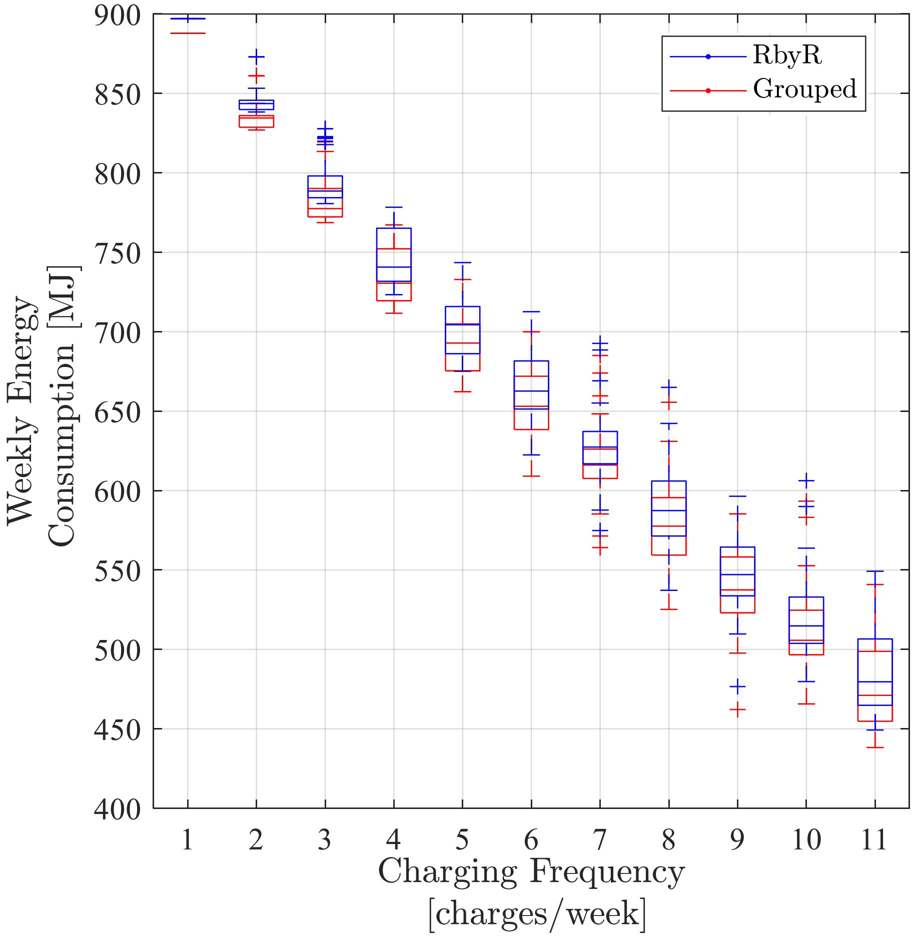

Figure 5.1: Weekly Energy Consumption

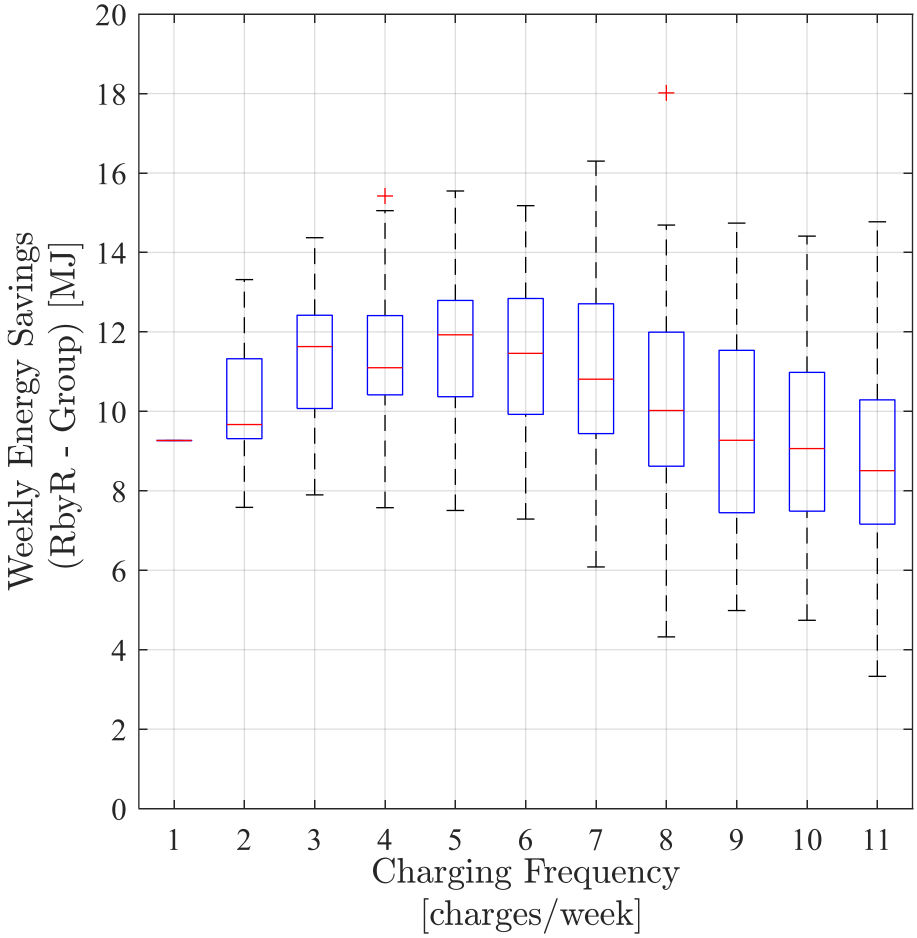

Figure 5.2: Weekly Energy Savings

By separating the energy consumption into the specific fuel and battery energy consumption, the effect of look-ahead information can be studied further. The R by R and grouped run results are very similar when comparing battery energy in Figure 5.3. Both the spread of the boxplots and the median battery energy consumptions are alike. The difference in energy consumption between the R by R and grouped runs can be attributed to the fuel consumption in Figure 5.4. In this figure, there is a pronounced offset between the R by R and grouped run fuel consumption. A more prominent offset in fuel consumption signifies that future information is more significant for fuel than for battery energy consumption.

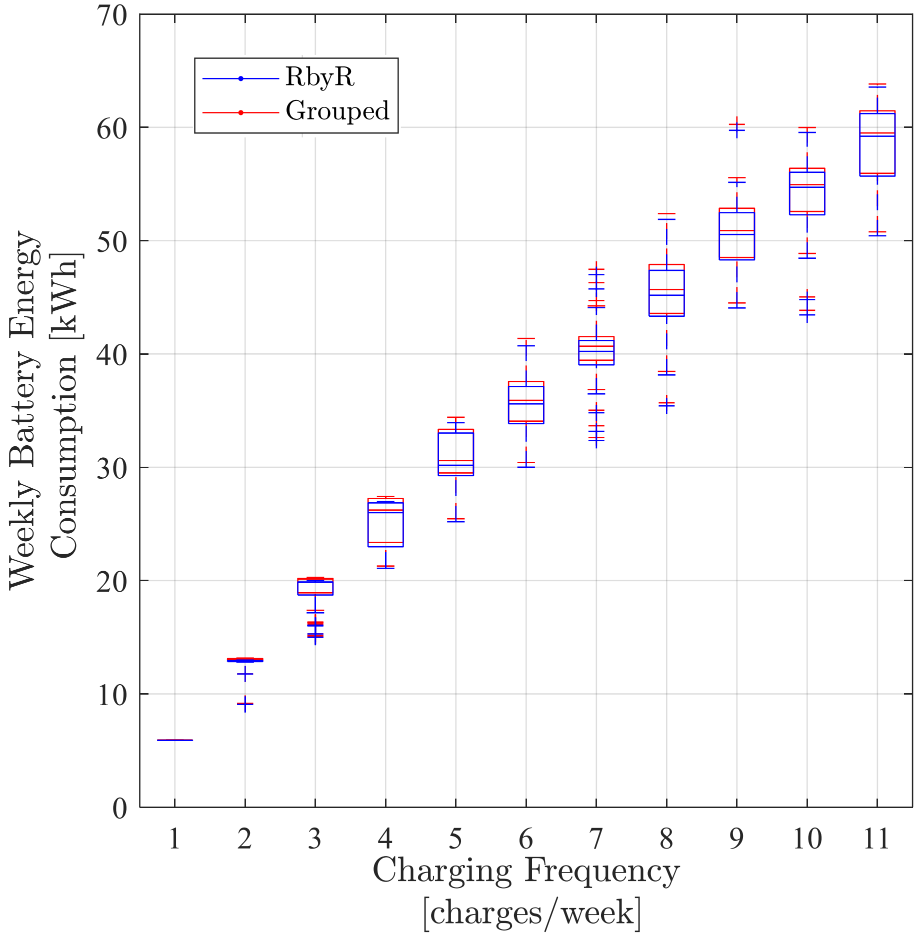

Figure 5.3: Weekly Battery Energy Consumption

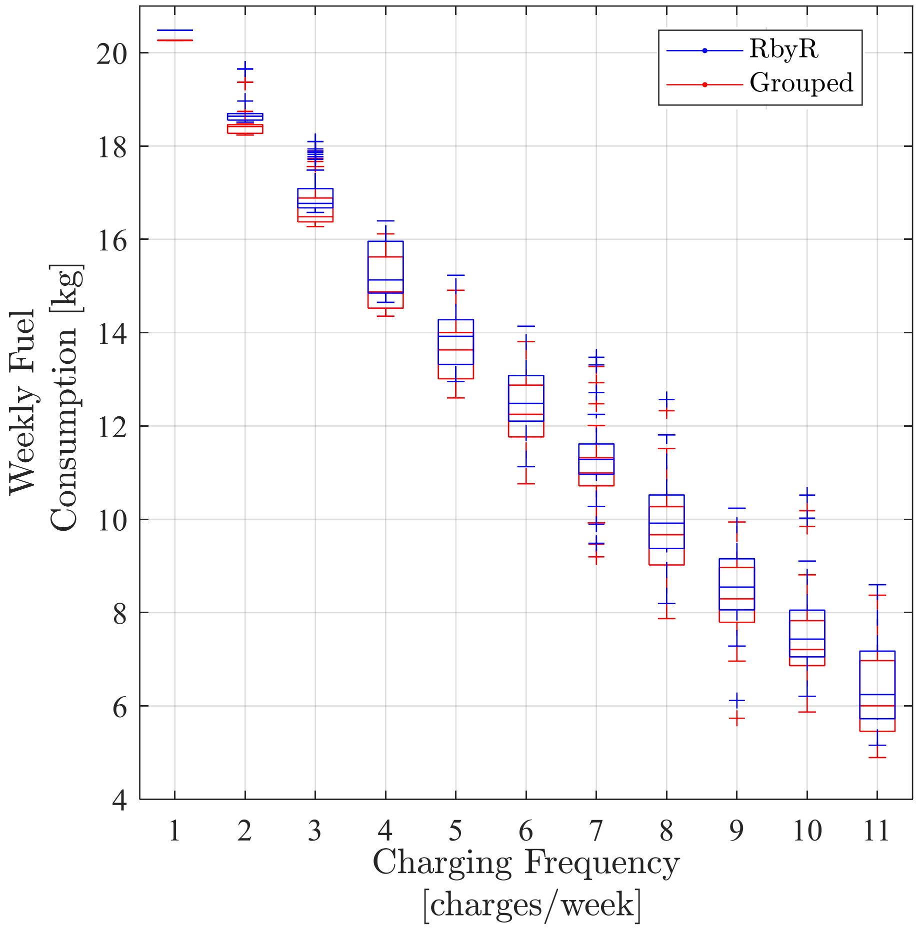

Figure 5.4: Weekly Fuel Consumption

To provide more insight on the effect of future information, charging frequency, and allocation of charging events, the fuel economy of the weekly variations are compared in Figure 5.5 and Figure 5.6. The MPG and MPGe both show an increase in the spread of data as the charging frequency increases. Though, the MPGe spread for 8 charges per week in Figure 5.6 is evidently smaller than the MPG spread. This indicates that, similarly to the effect of future information, the allocation of charging events has a heightened effect on the fuel consumption compared to the battery energy. The comparison between MPG and MPGe also shows a difference in the trend between fuel economy and charging frequency. The MPG increases exponentially with a higher charging frequency. Charging once more per week corresponds to a larger gain in MPG if the original charging frequency is already elevated compared to a lower frequency. The MPGe plot displays a linear trend, in which one more charge per week would increase the MPGe a similar amount regardless of the original frequency.

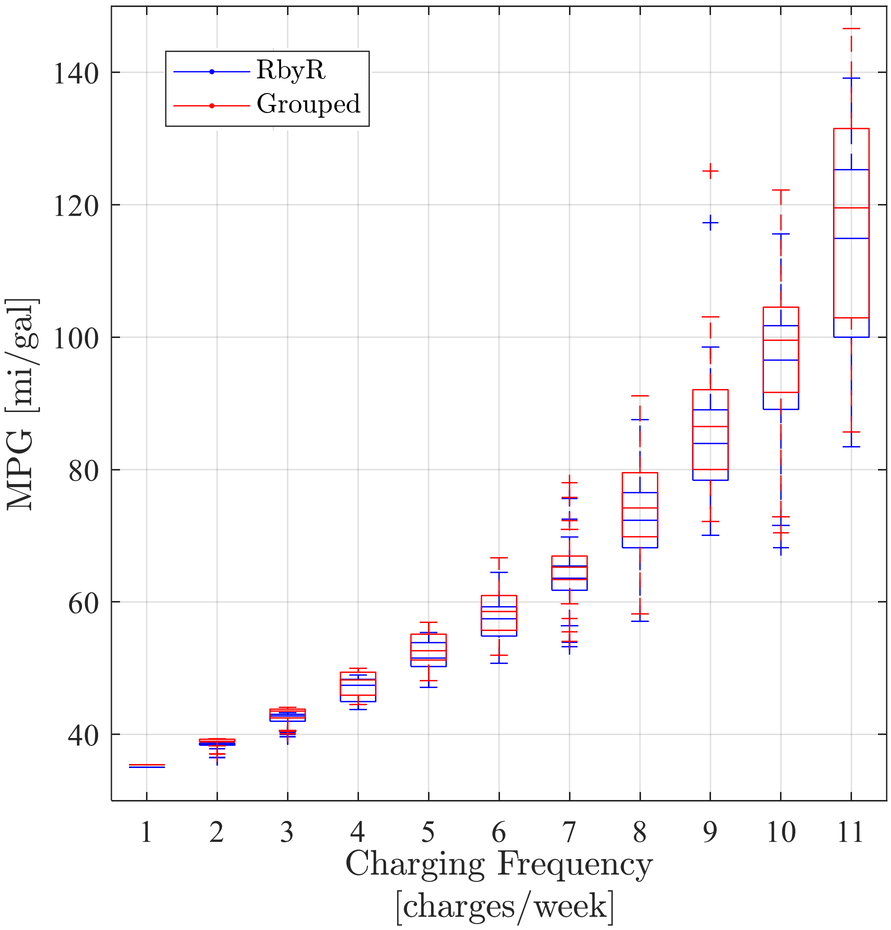

Figure 5.5: MPG of the Week Variations

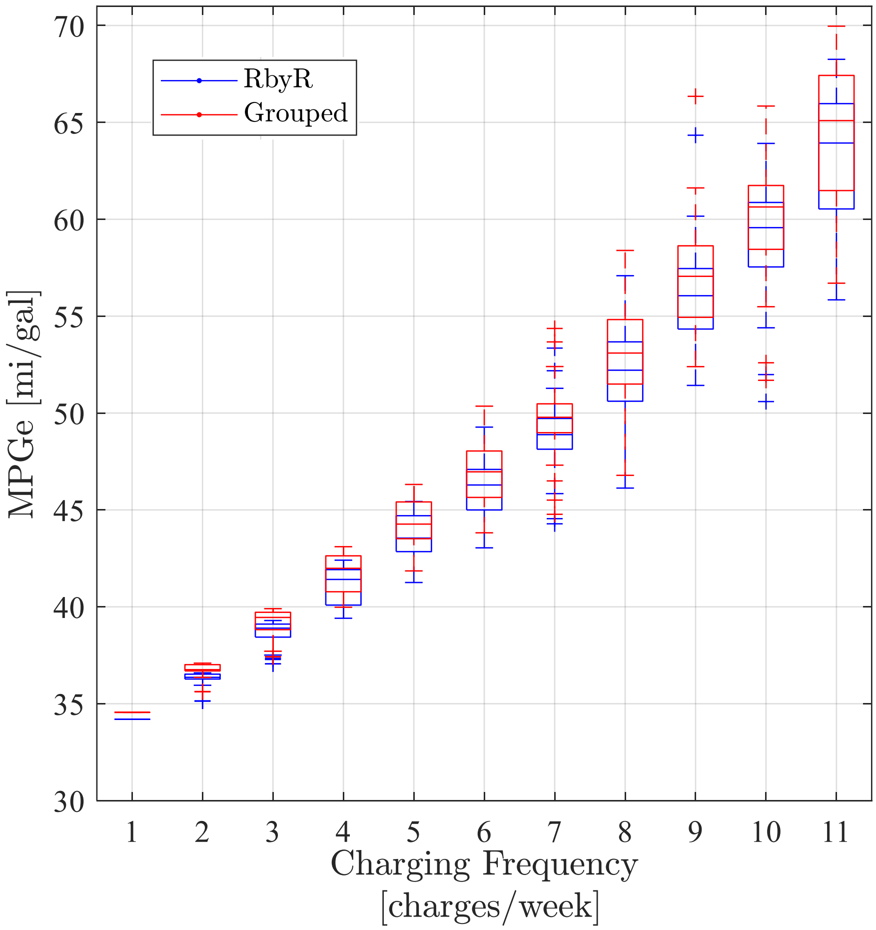

Figure 5.6: MPGe of the Week Variations

To further explore these charging behavior trends, the study has been extended to include higher charging frequencies for further analysis. With 36 routes in the week, the study can be extended to a maximum of 36 charging events. With an unrealistic number of charging events, the locations of the charges cannot be determined by Algorithm 4.1 and are instead populated randomly.

The extended weekly energy consumption is shown in Figure 5.7. The transition from realistic to more frequent charging behaviors can be seen from the slightly disjoint nature between 11 and 12 charges per week. As the charging frequency increases, the energy consumption converges to a minimum value of 300 MJ. The expansion of charging frequencies reveals a more defined exponential trend between charging frequency and energy consumption than the realistic charging behaviors. Due to this exponential nature, one additional charge per week would conserve more energy if the original frequency is smaller compared to a larger original frequency.

The extended energy savings in Figure 5.8 extends the parabolic trend seen with the realistic charging behaviors. After the peak in savings at 5 charges per week, the savings decrease as charging frequency increases. Because the grouped run only gets look-ahead information up to the next charging event, at 36 charges per week the grouped and R by R routes would receive the same route information.

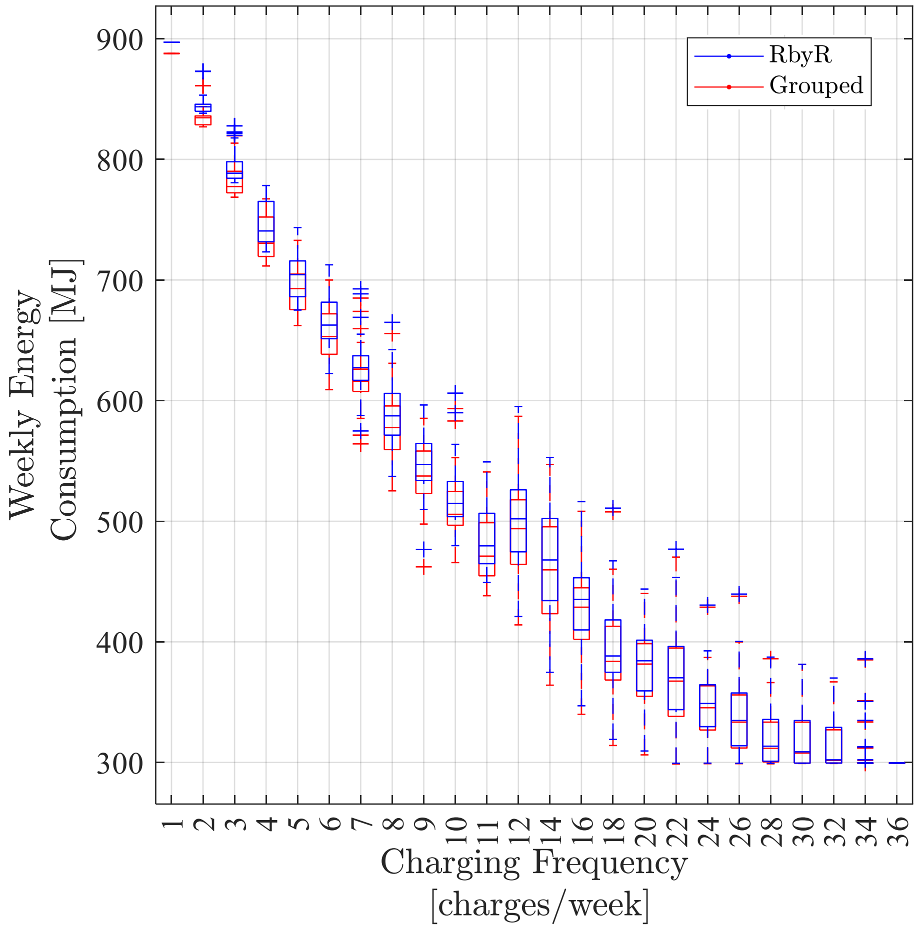

Figure 5.7: Extended Weekly Energy Consumption

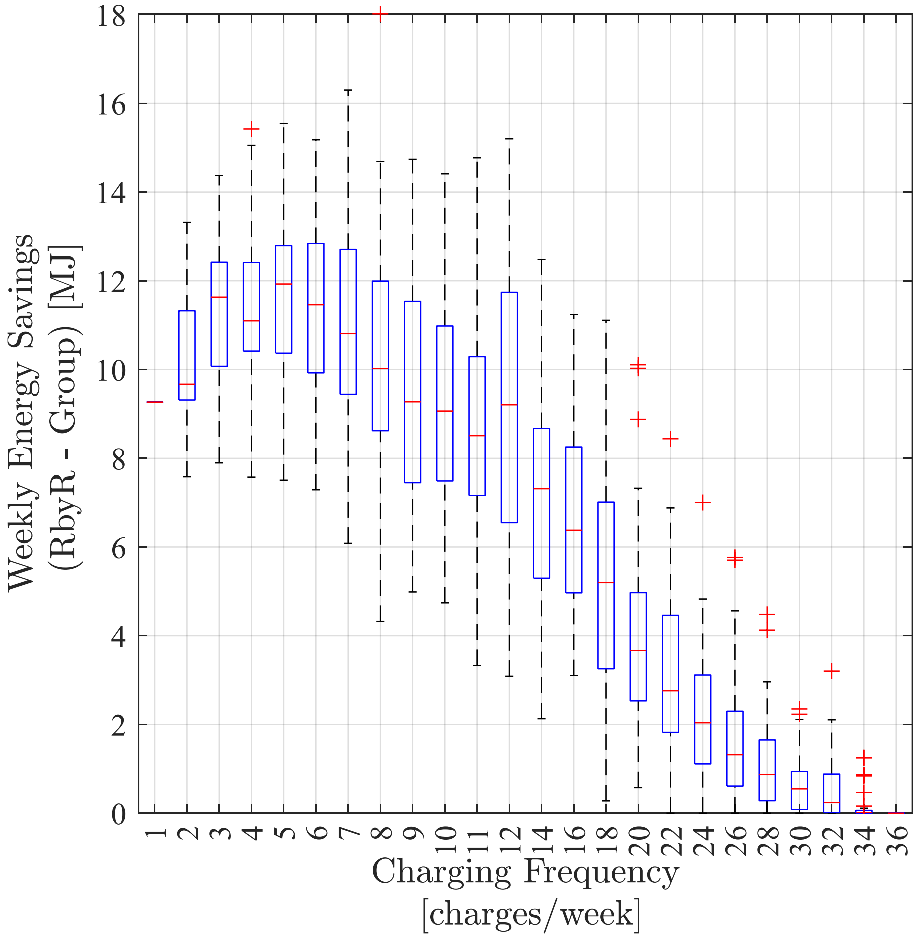

Figure 5.8: Extended Weekly Energy Savings

As the extended simulations use less fuel due to the increasing frequency of charging, the MPGe is sufficient in analyzing the fuel economy in Figure 5.9. The MPGe spread is much wider for the extended simulations than the realistic simulations. This is expected because the unrealistic charging frequencies have 36 total possible charging events, while the realistic charging frequencies only have 14. The maximum possible MPGe can be achieved with just 22 charges per week with the right charging allocation for both the R by R and the grouped runs. The effect of look-ahead information is further investigated in Figure 5.10 in which the MPGe gain for each week is found using Eq. (5.3) and the minimum, mean, and maximum values for each charging frequency are shown (disregarding outliers). The highest values of MPGe gain indicates where the effect of future information is the most significant. The average and maximum trends both reach a global maximum at 12 charges per week while the minimum trend peaks at 6 charges per week. This difference is due to the increase in the spread of data as charging frequency increases. The mean trend shows a fairly constant MPGe gain between 6 and 12 charges per week. This indicates that access to future information can increase fuel economy significantly within this region.

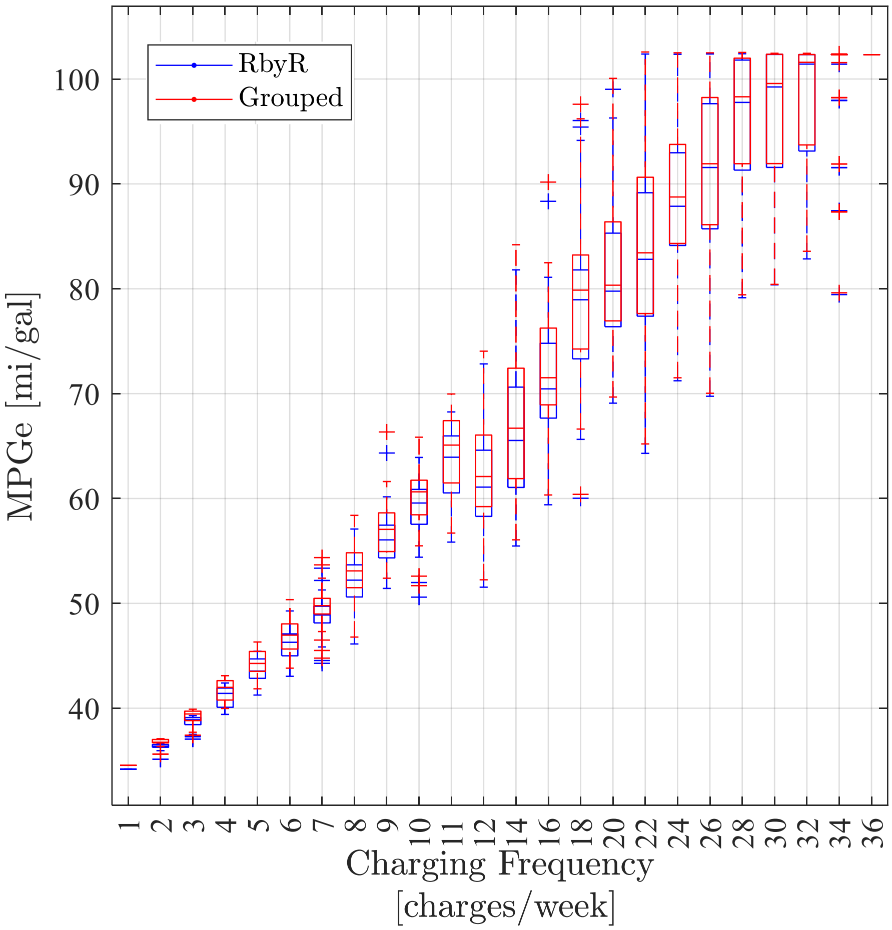

Figure 5.9: Extended Weekly MPGe

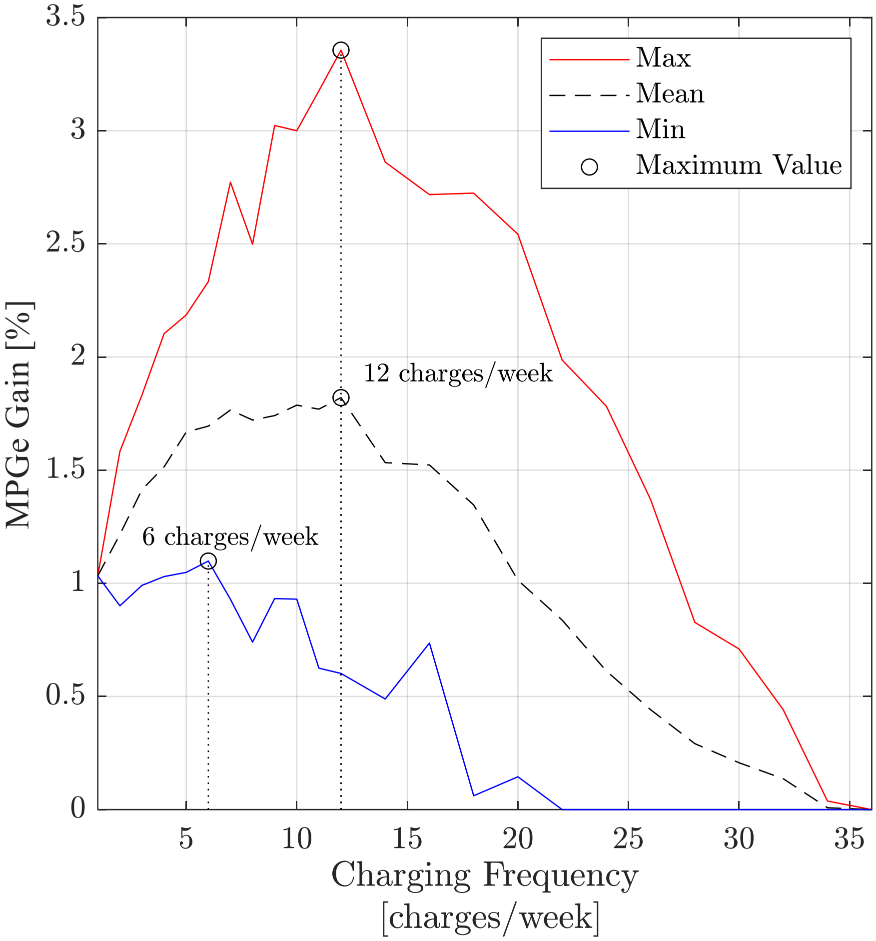

Figure 5.10: Extended MPGe Gain

To further analyze the spread of data for R by R and grouped runs, the MPGe is calculated individually for each area in between charges as shown in Figure 5.11. For most distances less than 34.3 km, the grouped and R by R runs have similar fuel economy. Further distances show an increased fuel economy for the grouped run in many cases. The lower boundary of the trend is an exception, where the similar fuel economy between grouped and R by R runs may be attributed to differing velocity profiles in between each charge. The region between 34.3 and about 130 km shows the most potential for future information to increase the fuel economy.

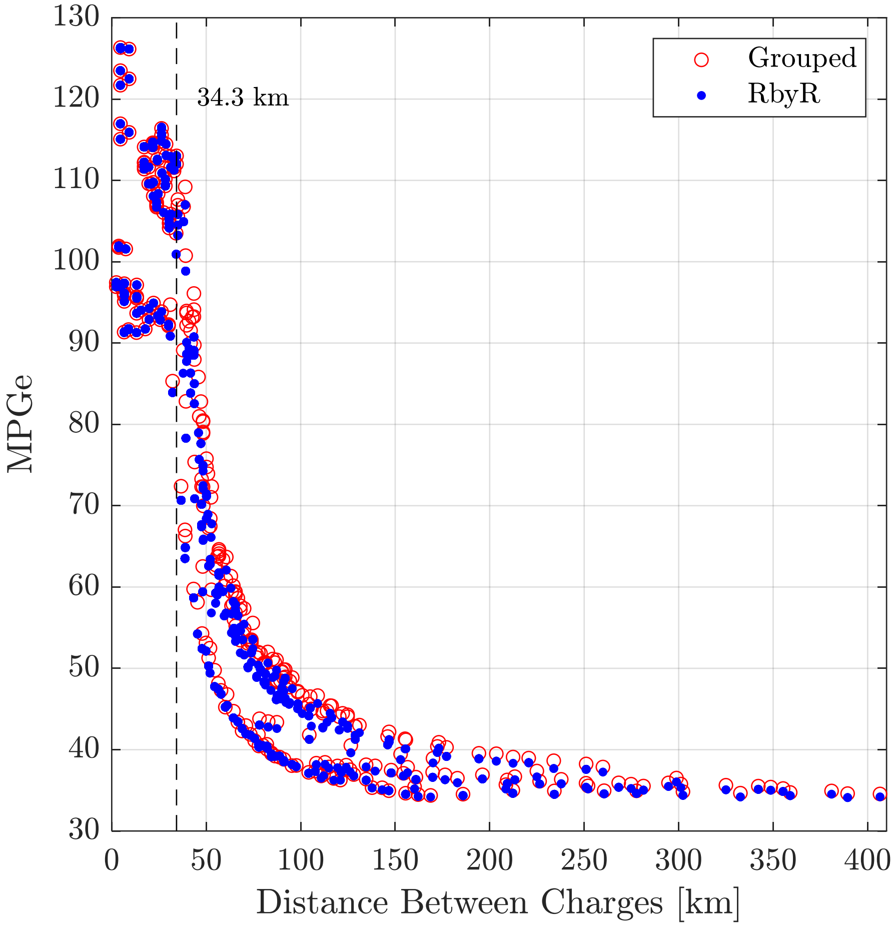

Figure 5.11: Distance Between Charges with MPGe

The utility factor (Figure 5.12) is only calculated for the R by R run as the blended strategy of the grouped run complicates the process of separating the AER from the charge sustaining regions. As expected, more charging events enable a larger percentage of distance to be traversed using only electricity. The utility factor increases at a steep linear slope for the realistic charging frequencies. Each additional charging frequency shows about a 5% increase in the median utility factor. The extension reveals a more logarithmic trend with unrealistic charging frequencies as the utility factor converges at 100%. Because the spread of data increases with charging frequency, the best utility factor for 2 charges per week is lower than the average for 3 charges per week. In comparison, the best utility factor for 8 charges per week exceeds the 3rd quartile utility factor for 9 charges per week. Generally, a charging frequency greater than 4 charges per week, with well-planned charging allocations, can achieve a utility factor greater than or equal to the median for the next charging frequency.

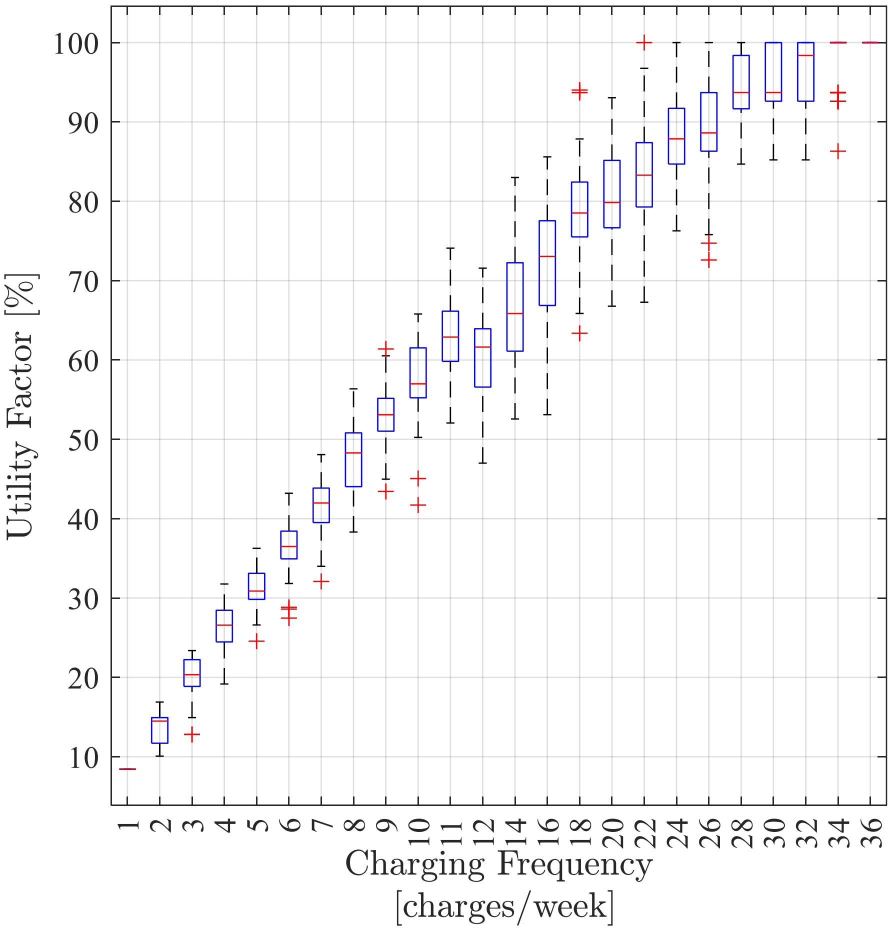

Figure 5.12: Utility Factor

On average, more frequent charging behaviors correlate with less distance in between charging events. Therefore, further investigation on the spread of data for the utility factor is shown in Figure 5.13 where the allocation of charging events is represented by the distance in between charging events. A smaller distance in between charges correlates with a higher utility factor. In fact, a distance between charges of over 100 km will deterministically achieve a utility factor below 40% for this PHEV and weekly route. The spread in the middle of the plot is due to the variation of the route. A distance of 100 km with a lower utility factor may have more urban characteristics with less opportunity to operate in EV mode than a highway or mixed route.

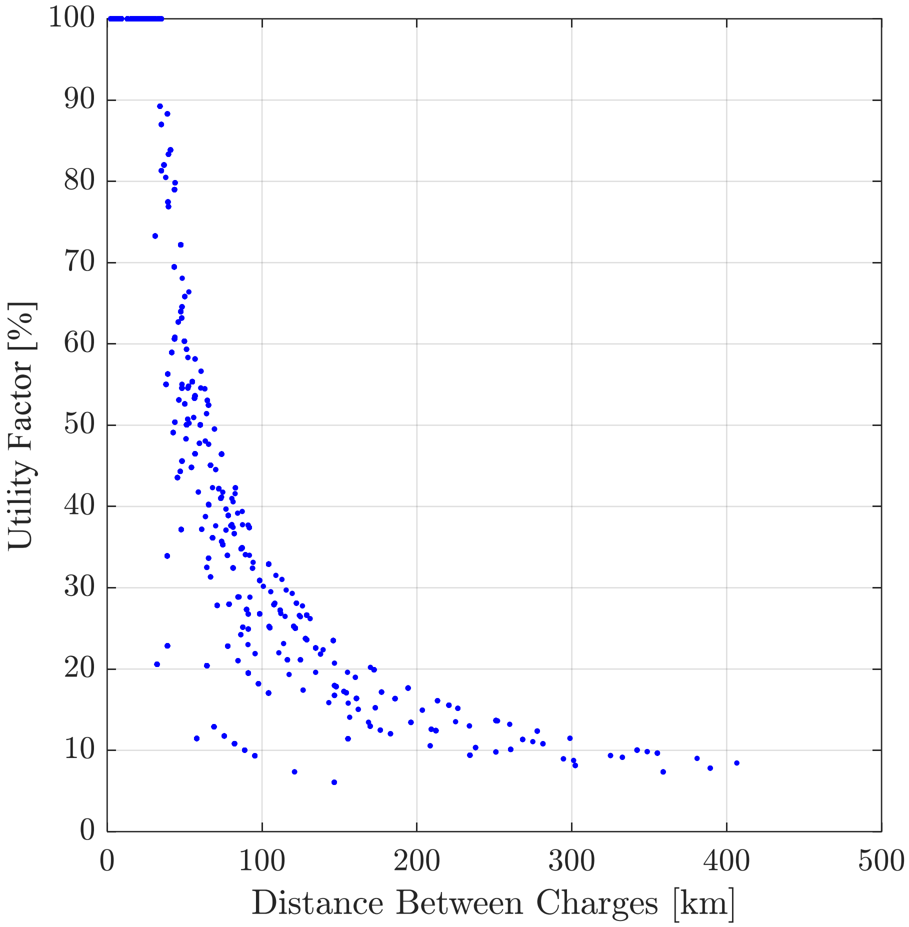

Figure 5.13: Effect of Charging Allocation on the Utility Factor

This study was run with the aim of exploring the effect of different charging behaviors on the energy consumption of a PHEV. Over 1102 charging behavior variations, the resulting average computation time for a grouped run was 2.25 hours and 2.27 hours for an R by R run. The findings revealed correlations between the three different charging behaviors analyzed, and the consumption, fuel economy, and utility factor metrics. A higher charging frequency determined lower energy and fuel consumption and a higher battery energy consumption. A higher charging frequency also corresponds to a higher fuel economy and utility factor. Look-ahead information of route characteristics, obtained by the group runs but not the R by R, was found to be related to charging frequency. This behavior was shown to have a larger influence on consumption and fuel economy as the charging frequency increased. Additionally, look-ahead information is shown to be most influential in fuel economy for distances between charging events between 34 and 130 km. The allocation of charging events was also shown to have greater influence on consumption and fuel economy with a higher charging frequency.

The three charging behaviors included in the analysis can be utilized to efficiently plan the charging decisions made for a trip. The charging frequency can be determined based on how many charging events the driver is willing to undergo and the metric the driver is most concerned about. The specific metric and the charging frequency can also aid in the decision of charging allocation. If the metric boxplot spread for the charging frequency is small, the driver may choose to not plan out the distance between charging events. Or if the metric spread is large, the driver may choose a different route that would decrease distances between charging events. With these two behaviors decided, the route characteristics have been satisfied as well. Alternatively, if the route characteristics cannot be changed and the charging frequency is still known, the best charging allocation can be found. If both the best charging allocation and route characteristics are chosen, either based on necessity or the metric results, the charging frequency is automatically known. In conclusion, the interconnectedness between these three charging behaviors can be crucial in route planning for energy efficiency.

Chapter 6 Conclusion and Future Work

6.1 Conclusion

In this thesis, an open-loop model of the power split PHEV is developed to predict vehicle energy usage. The model is calibrated using experimental data collected on regulatory and real-world driving cycles. After the component-level calibration, open-loop model simulations show an average fuel consumption error of 2.2%, an average battery energy consumption error of 2.9%, and an average energy consumption error of 2.9% over 25 real-world cycles.

Then, an optimization for the velocity dynamics and powertrain optimization is formulated with a cost that accounts for both equivalent energy consumption and travel time. Dynamic Programming is used to solve the nonlinear deterministic problem. The solution is solved for an aggressive driver, normal driver, and relaxed driver, and each beginning with a full, moderately charged, and a fully depleted battery. The Pareto fronts obtained from these solutions show more variability in energy consumption and travel time with a lower initial state of charge. Moreover, the variation in driver behavior was a significant variable in the travel time and fuel consumed in the solution. The optimization problem was also solved over 25 real-world cycles using the weighting factor γ that results in a similar travel time to the cycle. Overall, the DP solution on average reduced the fuel consumption by 10%, the battery energy consumption by 8%, and the total energy consumption by 19% as compared to the real-world data.

Utilizing the developed optimization algorithm, a representative weekly driving schedule with varying charging behaviors is simulated and optimized. In this study 1102 different weeks with varying charging events are generated. The deterministic routes with corresponding speed limits are used as inputs to the optimization algorithm. Each week variation is optimized following two different strategies, one involving look-ahead route information and the other without look-ahead information. The results of these strategies are compared in terms of energy consumption, fuel economy, and utility. Results show connectivity between the strategic placement of charging events, the presence of future information, and the charging frequency on the energy metrics analyzed. The recommended charging behavior can therefore be determined based on the regarded metric and route characteristics for the objective of energy efficient trip planning.

6.2 Future Work

Future work consists in further improving the computation time of the DP solver. This will enable further large-scale simulation studies and the in-vehicle implementation of the algorithm.

Moreover, the online solution of the VD&PT optimization strategy has been implemented in Phase I using a Rollout strategy [95]. This approach uses the offline solution over an entire route to provide an estimation of a terminal cost in an MPC [96].

Due to the significance of the availability of charging on the vehicle energy efficiency performance, future work will focus on the integration of the availability of charging information in the terminal cost used in the rollout strategy.

Bibliography

[1] Runsen Zhang and Shinichiro Fujimori 2020 *Environ. Res. Lett.* 15 034019.

[2] Creutzig F et al 2015 Transport: a roadblock to climate change mitigation? Science 350 911–2.

[3] Girod, B., van Vuuren, D.P., Grahn, M. *et al.* Climate impact of transportation A model comparison. *Climatic Change* 118, 595–608 (2013). https://doi.org/10.1007/s10584-012-0663-6

[4] IPCC (2014). *Climate Change 2014: Mitigation of Climate Change (PDF)*(1454 pp, 50 MB). Contribution of Working Group III to the Fifth Assessment Report of the Intergovernmental Panel on Climate Change [Edenhofer, O., R. Pichs-Madruga, Y. Sokona, E. Farahani, S. Kadner, K. Seyboth, A. Adler, I. Baum, S. Brunner, P. Eickemeier, B. Kriemann, J. Savolainen, S. Schlömer, C. von Stechow, T. Zwickel and J.C. Minx (eds.)]. Cambridge University Press, Cambridge, United Kingdom and New York, NY, USA.

[5] EPA. Environmental Protection Agency. Accessed March 30, 2023. https://www.epa.gov/transportation-air-pollution-and-climate-change/carbon-pollution-transportation.

[6] United States Environmental Protection Agency. “Fast Facts on Transportation Greenhouse Gas Emissions.” *US EPA*, 27 Aug. 2018, www.epa.gov/greenvehicles/fast-facts-transportation-greenhouse-gas-emissions.

[7] “Corporate Average Fuel Economy (CAFE) Standards.” *US Department of Transportation*, 11 Aug. 2014, www.transportation.gov/mission/sustainability/corporate-average-fuel-economy-cafe-standards.

[8] Lynberg, Matthew. “NHTSA.” *NHTSA*, 7 Nov. 2016, www.nhtsa.gov/laws-regulations/corporate-average-fuel-economy.

[9] Executive Office of the President. “Strengthening American Leadership in Clean Cars and Trucks.” *Federalregister.gov*, 10 Aug. 2021, www.federalregister.gov/documents/2021/08/10/2021-17121/strengthening-american-leadership-in-clean-cars-and-trucks.

[10] Revised 2023 and Later Model Year Light-Duty Vehicle Greenhouse Gas Emissions Standards, 86 Red. Reg. 74450 (December 30, 2021), https://www.govinfo.gov/content/pkg/FR-2021-12-30/pdf/2021-27854.pdf

[11] IEA (2021), *Global EV Outlook 2021*, IEA, Paris https://www.iea.org/reports/global-ev-outlook-2021, License: CC BY 4.0

[12] Gonder, J., Chen, Y., Lammert, M., and Wood, E., Assessing the Energy Impact of Connected and Automated Vehicle (CAV) Technologies. No. NREL/PR-5400-

65743 (Golden, CO (United States): National Renewable Energy Lab. (NREL), 2016).

[13] Vahidi, A., and Sciarretta, A., “Energy Saving Potentials of Connected and Automated Vehicles,” Transportation Research Part C: Emerging Technologies 95:822-843, 2018.

[14] US EPA,OAR. “Highlights of the Automotive Trends Report | US EPA.” *US EPA*, 6 Mar. 2019, www.epa.gov/automotive-trends/highlights-automotive-trends-report.

[15] Ebbesen, Soren & Elbert, Philipp & Guzzella, Lino. (2012). Engine Downsizing and Electric Hybridization Under Consideration of Cost and Drivability. Oil & Gas Science and Technology. 68. 109-116. 10.2516/ogst/2012030.

[16] Pantelis Kopelias, Elissavet Demiridi, Konstantinos Vogiatzis, Alexandros Skabardonis, Vassiliki Zafiropoulou, Connected & autonomous vehicles – Environmental impacts – A review, Science of The Total Environment, Volume 712, 2020, 135237, ISSN 0048-9697, https://doi.org/10.1016/j.scitotenv.2019.135237.

[17] EPA. Environmental Protection Agency. Accessed March 9, 2023. https://www.epa.gov/greenvehicles/self-driving-vehicles.

[18] Avi Chaim Mersky, Constantine Samaras, Fuel economy testing of autonomous vehicles, Transportation Research Part C: Emerging Technologies, Volume 65, 2016, Pages 31-48, ISSN 0968-090X, https://doi.org/10.1016/j.trc.2016.01.001.

[19] Parekh, Darsh, Nishi Poddar, Aakash Rajpurkar, Manisha Chahal, Neeraj Kumar, Gyanendra Prasad Joshi, and Woong Cho. 2022. "A Review on Autonomous Vehicles: Progress, Methods and Challenges" *Electronics* 11, no. 14: 2162. https://doi.org/10.3390/electronics11142162.

[20] Othman, K. Exploring the implications of autonomous vehicles: a comprehensive review. *Innov. Infrastruct. Solut.* 7, 165 (2022). https://doi.org/10.1007/s41062-022-00763-6

[21] Alawadhi, M., Almazrouie, J., Kamil, M. *et al.* A systematic literature review of the factors influencing the adoption of autonomous driving. *Int J Syst Assur Eng Manag* 11, 1065–1082 (2020). https://doi.org/10.1007/s13198-020-00961-4

[22] Litman T (2023) Autonomous vehicle implementation predictions. Victoria Transport Policy Institute.

[23] "Federal Motor Vehicle Safety Standards; Electronic Stability Control Systems." NHTSA. Accessed March 9, 2023. https://www.nhtsa.gov/fmvss/federal-motor-vehicle-safety-standards-electronic-stability-control-systems-0.

[24] Litman T (2015) Autonomous vehicle implementation predictions. Victoria Transport Policy Institute.

[25] Ahmed, Hafiz Usman, Ying Huang, Pan Lu, and Raj Bridgelall. 2022. "Technology Developments and Impacts of Connected and Autonomous Vehicles: An Overview" *Smart Cities* 5, no. 1: 382-404. https://doi.org/10.3390/smartcities5010022

[26] Dot, U. Preparing for the Future of Transportation: Automated Vehicles 3.0. US. Available online: https://www.transportation.gov/av/3

[27] "ARPA-E's NEXTCAR Program: Next-Generation Energy Technologies for Connected and Automated on-Road Vehicles." Accessed March 9, 2023. https://arpa-e.energy.gov/technologies/programs/nextcar.

[28] arpa-e.energy.gov. "Press Release | U.S. Department of Energy Awards $18 Million for Cutting-Edge Technologies to Optimize Vehicle Performance and Efficiency," March 11, 2021. http://arpa-e.energy.gov/news-and-media/press-releases/us-department-energy-awards-18-million-cutting-edge-technologies.

[29] Ha, Paul, Sikai Chen, Runjia Du, Jiqian Dong, Yujie Li, and Samuel Labi. "Vehicle Connectivity and Automation: A Sibling Relationship." Frontiers, October 26, 2020. https://doi.org/10.3389/fbuil.2020.590036.

[30] Robert J. Lempert, Benjamin Preston, Sophia M. Charan, Laura Fraade-Blanar, Marjory S. Blumenthal, The societal benefits of vehicle connectivity, Transportation Research Part D: Transport and Environment, Volume 93, 2021, 102750, ISSN 1361-9209, https://doi.org/10.1016/j.trd.2021.102750.

[31] J. Liu, Y. Chen, W. Li, F. Shang and J. Zhan, "Hybrid-Trip-Model-Based Energy Management of a PHEV With Computation-Optimized Dynamic Programming," in *IEEE Transactions on Vehicular Technology*, vol. 67, no. 1, pp. 338-353, Jan. 2018, doi: 10.1109/TVT.2017.2777852.

[32] Gunter Heppeler, Marcus Sonntag, Oliver Sawodny, Fuel Efficiency Analysis for Simultaneous Optimization of the Velocity Trajectory and the Energy Management in Hybrid Electric Vehicles, IFAC Proceedings Volumes, Volume 47, Issue 3, 2014, Pages 6612-6617, ISSN 1474-6670, ISBN 9783902823625, https://doi.org/10.3182/20140824-6-ZA-1003.00286.

[33] Zheng Chen, Simin Wu, Shiquan Shen, Yonggang Liu, Fengxiang Guo, Yuanjian Zhang, Co-optimization of velocity planning and energy management for autonomous plug-in hybrid electric vehicles in urban driving scenarios, Energy, Volume 263, Part F, 2023, 126060, ISSN 0360-5442, https://doi.org/10.1016/j.energy.2022.126060.

[34] G. Li, D. Görges and M. Wang, "Online Optimization of Gear Shift and Velocity for Eco-Driving Using Adaptive Dynamic Programming," in *IEEE Transactions on Intelligent Vehicles*, vol. 7, no. 1, pp. 123-132, March 2022, doi: 10.1109/TIV.2021.3111037.

[35] D. Chen, Y. Kim, M. Huang and A. Stefanopoulou, "An Iterative and Hierarchical Approach to Co-optimizing the Velocity Profile and Power-split of Plug-in Hybrid Electric Vehicles," *2020 American Control Conference (ACC)*, Denver, CO, USA, 2020, pp. 3059-3064, doi: 10.23919/ACC45564.2020.9147804.

[36] G. Ma, M. Ghasemi and X. Song, "Integrated Powertrain Energy Management and Vehicle Coordination for Multiple Connected Hybrid Electric Vehicles," in *IEEE*

Transactions on Vehicular Technology, vol. 67, no. 4, pp. 2893-2899, April 2018, doi: 10.1109/TVT.2017.2780268.

[37] Gupta, Shobhit. "Perturbed Optimal Control for Connected and Automated Vehicles." Doctoral dissertation, Ohio State University, 2022. http://rave.ohiolink.edu/etdc/view?acc_num=osu166992705806715

[38] Chen, Bo, Robinette, Darrell, Shahbakhti, Mahdi, Zhang, Kuilin, Naber, Jeff, Worm, Jeremy, Pinnow, Christopher, and Morgan, Christopher. Fri . "Connected Vehicles and Powertrain Optimization". United States. https://doi.org/10.1115/1.2017-Sep-5. https://www.osti.gov/servlets/purl/1572158.

[39] M. R. Amini, X. Gong, Y. Feng, H. Wang, I. Kolmanovsky and J. Sun, "Sequential optimization of speed, thermal load, and power split in connected HEVs," *2019 American Control Conference (ACC)*, Philadelphia, PA, USA, 2019, pp. 4614-4620, doi: 10.23919/ACC.2019.8815158.

[40] Deshpande, S. R., Gupta, S., Gupta, A., and Canova, M. (January 25, 2022). "Real-Time Ecodriving Control in Electrified Connected and Autonomous Vehicles Using Approximate Dynamic Programing." ASME. *J. Dyn. Sys., Meas., Control*. January 2022; 144(1): 011111. https://doi.org/10.1115/1.4053292

[41] Chen, D., Huang, M., Stefanopoulou, A. G., and Kim, Y. (December 27, 2021). "Co-Optimization of Velocity and Charge-Depletion for Plug-In Hybrid Electric Vehicles: Accounting for Acceleration and Jerk Constraints." ASME. *J. Dyn. Sys., Meas., Control*. January 2022; 144(1): 011107. https://doi.org/10.1115/1.4053139

[42] A. Meshginqalam and J. Bauman, "Integrated Convex Speed Planning and Energy Management for Autonomous Fuel Cell Hybrid Electric Vehicles," in *IEEE Transactions on Transportation Electrification*, vol. 9, no. 1, pp. 1072-1086, March 2023, doi: 10.1109/TTE.2022.3200013.

[43] Chen, J., Qian, L.-J., Xuan, L., Chen, C.: Hierarchical eco-driving control strategy for hybrid electric vehicle platoon at signalized intersections under partially connected and automated vehicle environment. *IET Intell. Transp. Syst.* 00, 1– 19 (2022). https://doi.org/10.1049/itr2.12325

[44] L. Serrao, S. Onori and G. Rizzoni, "ECMS as a realization of Pontryagin's minimum principle for HEV control," *2009 American Control Conference*, St. Louis, MO, USA, 2009, pp. 3964-3969, doi: 10.1109/ACC.2009.5160628.

[45] M. Ghasemi and X. Song, "Powertrain Energy Management for Autonomous Hybrid Electric Vehicles With Flexible Driveline Power Demand," in *IEEE Transactions on Control Systems Technology*, vol. 27, no. 5, pp. 2229-2236, Sept. 2019, doi: 10.1109/TCST.2018.2838555.

[46] Hao, Peng, Boriboonsomsin, Kanok, Wu, Guoyuan, Gao, Zhiming, Laclair, Tim, and Barth, Matthew. 2019. "Deeply Integrated Vehicle Dynamic and Powertrain Operation for Efficient Plug-in Hybrid Electric Bus". United States. https://www.osti.gov/servlets/purl/1560399.

[47] Onori S, Serrao L, Rizzoni G. *Hybrid Electric Vehicles [electronic Resource] : Energy Management Strategies / by Simona Onori, Lorenzo Serrao, Giorgio Rizzoni.* 1st ed. 2016. Springer London; 2016. doi:10.1007/978-1-4471-6781-5

[48] G. P. Padilla, S. Weiland and M. C. F. Donkers, "A Global Optimal Solution to the Eco-Driving Problem," in *IEEE Control Systems Letters*, vol. 2, no. 4, pp. 599-604, Oct. 2018, doi: 10.1109/LCSYS.2018.2846182.

[49] Bellman, Richard. “Dynamic Programming.” *Science* 153, no. 3731 (1966): 34–37. http://www.jstor.org/stable/1719695.

[50] Martin L. Puterman, Chapter 8 Markov decision processes, Handbooks in Operations Research and Management Science, Elsevier, Volume 2, 1990, Pages 331-434, ISSN 0927-0507,ISBN 9780444874733, https://doi.org/10.1016/S0927-0507(05)80172-0.

[51] Kia, Solmaz. “Lecture Notes for MAE 274 (Optimal Control) Mechanical and Aerospace Eng. Dept., University of California Irvine.”

[52] C. Lin, J. Kang, J. Grizzle, and H. Peng, “Energy management strategy for a parallel hybrid electric truck,” Proceedings of the 2001 American Control Conference, vol. 4, pp. 2878–2883, 2001.

[53] L. Pérez, G. Bossio, D. Moitre, and G. García, “Optimization of power management in an hybrid electric vehicle using dynamic programming,” Mathematics and Computers in Simulation, vol. 73, no. 1-4, pp. 244–254, 2006

[54] A. Sciarretta, M. Back, and L. Guzzella, “Optimal control of parallel hybrid electric vehicles,” IEEE Transactions on Control Systems Technology, vol. 12, no. 3, pp. 352–363, 2004.

[55] Bellman, Richard. "The theory of dynamic programming." *Bulletin of the American Mathematical Society* 60, no. 6 (1954): 503-515.

[56] Wang, Rui, and Srdjan M. Lukic. "Dynamic programming technique in hybrid electric vehicle optimization." In *2012 IEEE international electric vehicle conference*, pp. 1-8. IEEE, 2012.

[57] Serrao, L., 2009, “A Comparative Analysis of Energy Management Strategies for Hybrid Electric Vehicles,” Ph.D. thesis, The Ohio State University, Columbus, OH.

[58] Plötz, Patrick & Moll, Cornelius & Bieker, Georg & Mock, Peter. (2021). From lab-to-road: Real-world fuel consumption and CO 2 emissions of plug-in-hybrid electric vehicles. Environmental Research Letters. 16. 10.1088/1748-9326/abef8c.

[59] Yanbo Ge, Don MacKenzie, David R. Keith, Gas anxiety and the charging choices of plug-in hybrid electric vehicle drivers, Transportation Research Part D: Transport and Environment, Volume 64, 2018, Pages 111-121, ISSN 1361-9209, https://doi.org/10.1016/j.trd.2017.08.021.

[60] Jing Dong, Zhenhong Lin, Within-day recharge of plug-in hybrid electric vehicles: Energy impact of public charging infrastructure, Transportation Research Part D: Transport and Environment, Volume 17, Issue 5, 2012, Pages 405-412, ISSN 1361-9209, https://doi.org/10.1016/j.trd.2012.04.003.

[61] Zoepf, S., MacKenzie, D., Keith, D., & Chernicoff, W. (2013). Charging Choices and Fuel Displacement in a Large-Scale Demonstration of Plug-In Hybrid Electric Vehicles. Transportation Research Record, 2385(1), 1–10. https://doi.org/10.3141/2385-01

[62] B. Adornato, R. Patil, Z. Filipi, Z. Baraket and T. Gordon, "Characterizing naturalistic driving patterns for Plug-in Hybrid Electric Vehicle analysis," *2009 IEEE Vehicle Power and Propulsion Conference*, 2009, pp. 655-660, doi: 10.1109/VPPC.2009.5289786.

[63] Plötz P, Moll. C, Bieker G, Mock P and Li Y 2020 Real-world usage of plug-in hybrid electric vehicles: fuel consumption, electric driving, and CO2 emissions International Council on Clean transportation (ICCT) White paper, September 2020

[64] Tal G, Raghavan S, Karanam V, Favetti M, Sutton K, Lee J H and Turrentine T 2020 Advanced plug-in electric vehicle travel and charging behavior—final report California Air Resources Board Contract pp 12–319

[65] Scherrer, A., Burghard, U., Wietschel, M. & Dütshcke, E. (2019). Early Adopter von E-Fahrzeugen: Ladeleistungen, Eigenerzeugung und Einstellungen zum Lademanagement. [Early Adopter of Electric Vehicles: charging power, PV installations, and attitudes towards demand side management]. Energiewirtschaftliche Tagesfragen 69 (11), 23-26

[66] NPM (National Plattform Future of Mobility). (2020). Task force optimierter Nutzungsgrad von Plug-in-Hybridfahrzeugen (PHEV). [Task force optimised usage of plug-in hybrid electric vehicles]. Internal Presentation, July 2020

[67] Chakraborty, Debapriya, Scott Hardman, and Gil Tal. “Why Do Some Consumers Not Charge Their Plug-in Hybrid Vehicles? Evidence from Californian Plug-in Hybrid Owners - IOPscience.” Why do some consumers not charge their plug-in hybrid vehicles? Evidence from Californian plug-in hybrid owners - IOPscience, August 5, 2020. https://doi.org/10.1088/1748-9326/ab8ca5.

[68] International Council on Clean Transportation. “Real World Usage of Plug-in Hybrid Vehicles in the United States - International Council on Clean Transportation,” n.d. https://theicct.org/publication/real-world-phev-us-dec22/.

[69] S. Midlam-Mohler, S. Ewing, V. Marano, Y. Guezennec and G. Rizzoni, "PHEV fleet data collection and analysis," *2009 IEEE Vehicle Power and Propulsion Conference*, Dearborn, MI, USA, 2009, pp. 1205-1210, doi: 10.1109/VPPC.2009.5289712.

[70] Pittel, M. and Martin, D., “eFlite Dedicated Hybrid Transmission for Chrysler Pacifica,” SAE Technical Paper 2018-01-0396, 2018, doi:10.4271/2018-01-0396

[71] “2017 Chrysler Pacifica Hybrid.” Car and Driver. Car and Driver, November 29, 2021. https://www.caranddriver.com/reviews/a15093447/2017-chrysler-pacifica-hybrid-test-review/.

[72] EPA. Environmental Protection Agency. Accessed January 17, 2023. https://www.epa.gov/fueleconomy.

[73] J. Wu, J. Ruan, N. Zhang and P. D. Walker, "An Optimized Real-Time Energy Management Strategy for the Power-Split Hybrid Electric Vehicles," in *IEEE Transactions on Control Systems Technology*, vol. 27, no. 3, pp. 1194-1202, May 2019, doi: 10.1109/TCST.2018.2796551.

[74] Morteza Montazeri-Gh, Mehdi Mahmoodi-k, Development a new power management strategy for power split hybrid electric vehicles, Transportation Research Part D: Transport and Environment, Volume 37, 2015, Pages 79-96, ISSN 1361-9209, https://doi.org/10.1016/j.trd.2015.04.024.

[75] Maguire, J. M., Peng, H., & Bai, S. (2013). *Dynamic analysis and control system design of automatic transmissions*. SAE International.

[76] A. Kahraman, D.R. Hilty, A. Singh, An experimental investigation of spin power losses of a planetary gear set, Mechanism and Machine Theory, Volume 86, 2015, Pages 48-61, ISSN 0094-114X, https://doi.org/10.1016/j.mechmachtheory.2014.12.003.

[77] Charles Nutakor, Adam Kłodowski, Jussi Sopanen, Aki Mikkola, José I. Pedrero, Planetary gear sets power loss modeling: Application to wind turbines, Tribology International, Volume 105, 2017, Pages 42-54, ISSN 0301-679X, https://doi.org/10.1016/j.triboint.2016.09.029.

[78] Tugan Eritenel, Robert G. Parker, An investigation of tooth mesh nonlinearity and partial contact loss in gear pairs using a lumped-parameter model, Mechanism and Machine Theory, Volume 56, 2012, Pages 28-51, ISSN 0094-114X, https://doi.org/10.1016/j.mechmachtheory.2012.05.002.

[79] P. Fajri, R. Ahmadi and M. Ferdowsi, "Equivalent vehicle rotational inertia used for electric vehicle test bench dynamic studies," *IECON 2012 - 38th Annual Conference on IEEE Industrial Electronics Society*, Montreal, QC, Canada, 2012, pp. 4115-4120, doi: 10.1109/IECON.2012.6389231.

[80] Gupta, S. (2019). Look-Ahead Optimization of a Connected and Automated 48V Mild-Hybrid Electric Vehicle. Master thesis, The Ohio State University, USA.

[81] Shobhit Gupta, Shreshta R. Deshpande, Punit Tulpule, Marcello Canova, Giorgio Rizzoni, An Enhanced Driver Model for Evaluating Fuel Economy on Real-World Routes, IFAC-PapersOnLine, Volume 52, Issue 5, 2019, Pages 574-579, ISSN 2405-8963, https://doi.org/10.1016/j.ifacol.2019.09.091.

[82] Sohrab Bazm, Pedro Lima, Somayeh Nemati, Analysis of the Euler and trapezoidal discretization methods for the numerical solution of nonlinear functional Volterra integral equations of Urysohn type, Journal of Computational and Applied Mathematics, Volume 398, 2021, 113628, ISSN 0377-0427, https://doi.org/10.1016/j.cam.2021.113628.

[83] C. Lin, J. Kang, J. Grizzle, and H. Peng, “Energy management strategy for a parallel hybrid electric truck,” Proceedings of the 2001 American Control Conference, vol. 4, pp. 2878–2883, 2001.

[84] Shobhit Gupta, Shreshta R. Deshpande, Punit Tulpule, Marcello Canova, Giorgio Rizzoni, An Enhanced Driver Model for Evaluating Fuel Economy on Real-World Routes, IFAC-PapersOnLine, Volume 52, Issue 5, 2019, Pages 574-579, ISSN 2405-8963, https://doi.org/10.1016/j.ifacol.2019.09.091.

[85] Plötz P, Moll. C, Bieker G, MockP and Li Y 2020 Real-world usage of plug-in hybrid electric vehicles: fuel consumption, electric driving, and CO2 emissions International Council on Clean transportation (ICCT) White paper, September 2020

[86] Tefft, B.C. (2022). American Driving Survey: 2020–2021 (Research Brief). Washington, D.C.: AAA Foundation for Traffic Safety

[87] Google Maps.

[88] OpenStreetMap. OSM History Dump © OpenStreetMap Contributors. Available online: https://planet.openstreetmap.org/planet/full-history/

[89] Tal G, Raghavan S, Karanam V, Favetti M, Sutton K, Lee J H and Turrentine T 2020 Advanced plug-in electric vehicle travel and charging behavior—final report California Air Resources Board Contract pp 12–319

[90] Scherrer, A., Burghard, U., Wietschel, M. & Dütshcke, E. (2019). Early Adopter von E-Fahrzeugen: Ladeleistungen, Eigenerzeugung und Einstellungen zum Lademanagement. [Early Adopter of Electric Vehicles: charging power, PV

installations, and attitudes towards demand side management]. Energiewirtschaftliche Tagesfragen 69 (11), 23-26

[91] NPM (National Plattform Future of Mobility). (2020). Task force optimierter Nutzungsgrad von Plug-in-Hybridfahrzeugen (PHEV). [Task force optimised usage of plug-in hybrid electric vehicles]. Internal Presentation, July 2020

[92] Chakraborty, Debapriya, Scott Hardman, and Gil Tal. “Why Do Some Consumers Not Charge Their Plug-in Hybrid Vehicles? Evidence from Californian Plug-in Hybrid Owners - IOPscience.” Why do some consumers not charge their plug-in hybrid vehicles? Evidence from Californian plug-in hybrid owners - IOPscience, August 5, 2020. https://doi.org/10.1088/1748-9326/ab8ca5.

[93] Aronoff, Eyal, and Nathan Taft. "IS THE GASOLINE GALLON EQUIVALENT AN ACCURATE MEASURE OF MILEAGE FOR ETHANOL AND METHANOL FUEL BLENDS?." (2013).

[94] US EPA. “Greenhouse Gases Equivalencies Calculator - Calculations and References | US EPA,” August 10, 2015. https://www.epa.gov/energy/greenhouse-gases-equivalencies-calculator-calculations-and-references.

[95] Gupta, Shobhit. "Perturbed Optimal Control for Connected and Automated Vehicles." Doctoral dissertation, Ohio State University, 2022. http://rave.ohiolink.edu/etdc/view?acc_num=osu166992705806715

[96] D Bertsekas. Rollout algorithms for constrained dynamic programming. *Lab. for Information and Decision Systems Report,* 2646, 2005

Appendix A: Simulation Campaign Results

The additional analysis is completed as an intermediate step in Chapter 5. An in-depth investigation into two specific variations is performed: variation 83 which has two charging events and variation 22 which has eight charging events. Variation 83 is shown in Figure A.1 and the recorded energy consumption, travel time, and ending SoC for each region between charging events is shown in Table A.1. This variation clearly exhibits the difference between the R by R CD-CS strategy and the grouped blended strategy. The blended strategy depletes the battery briefly then sustains the charge around 45-50% SoC until the battery is fully depleted before a charging event. Since the grouped run begins by sustaining the charge before the R by R run fully depletes the battery, the cumulative energy consumption early in the route is higher for the grouped run. The R by R energy consumption increases significantly during the charge sustaining portion, exceeding the grouped run's consumption before the charging event occurs. Similar to the sample in Chapter 4, the total energy consumption and travel time is lower for the grouped run for both of the regions in between charging events.

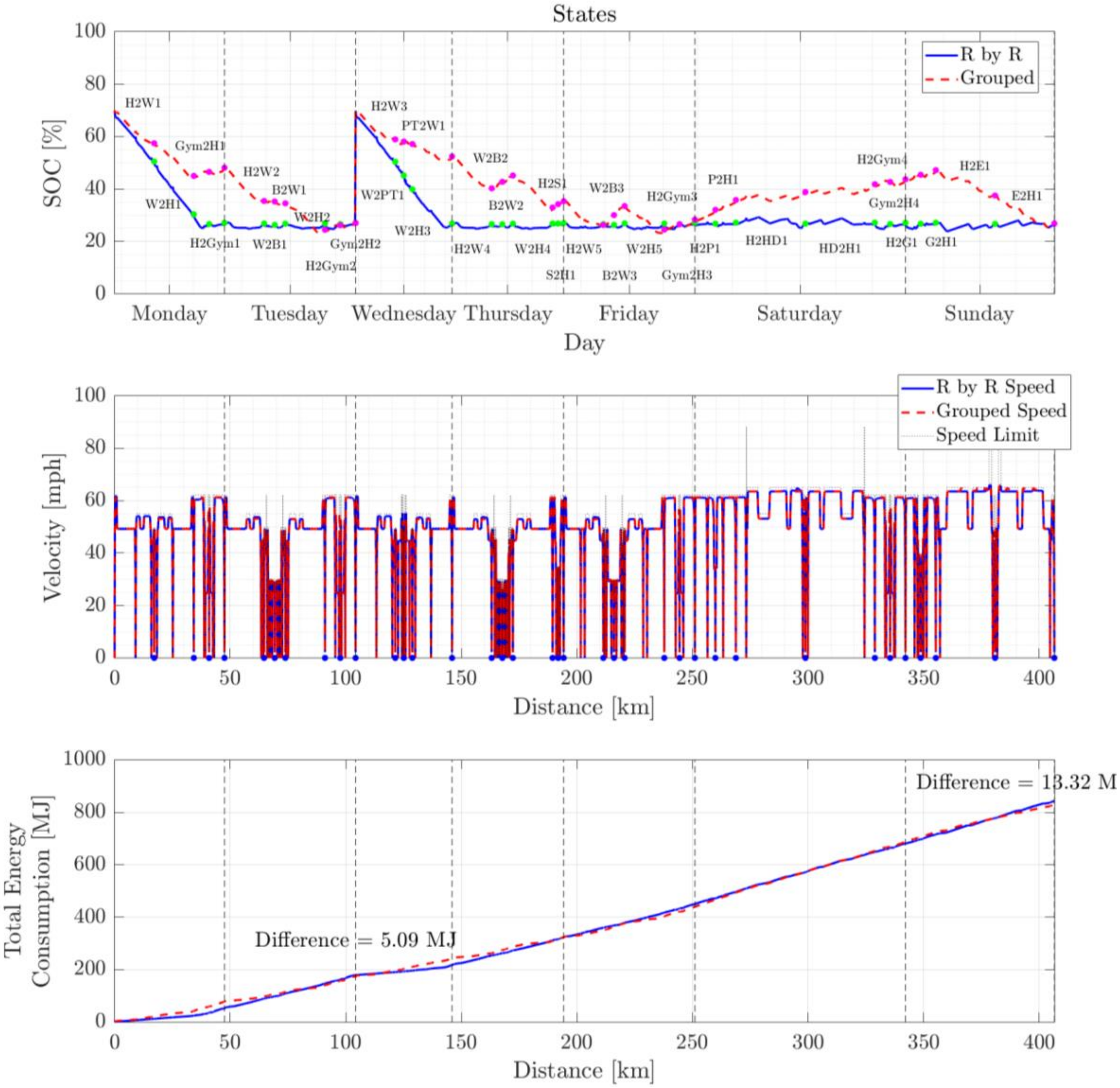

Figure A.1: Variation 83 Results

Table A.1: Variation 83 Summary

Variation 83	Total Energy Consumed [MJ]		Travel Time [s]		Ending SoC [%]	
	R by R	Grouped	R by R	Grouped	R by R	Grouped
From Start of Week to Charge 1	178.1	173.0	5307	5278	27.1	27.1
From Charge 1 to End of Week	663.4	655.1	14129	14042	26.9	26.9

Variation 22 represents a typical charging behavior where the vehicle is charged eight times a week. The portion of the route that spans Saturday is significant in that the energy consumption difference between the two runs is less than 1 MJ, yet the grouped run is 23 seconds faster than the R by R run. The ending SoC is very similar for both runs which suggests that the grouped run strategically uses the engine in certain parts of the route to optimize the travel time and maximize the amount of regeneration in the vehicle.

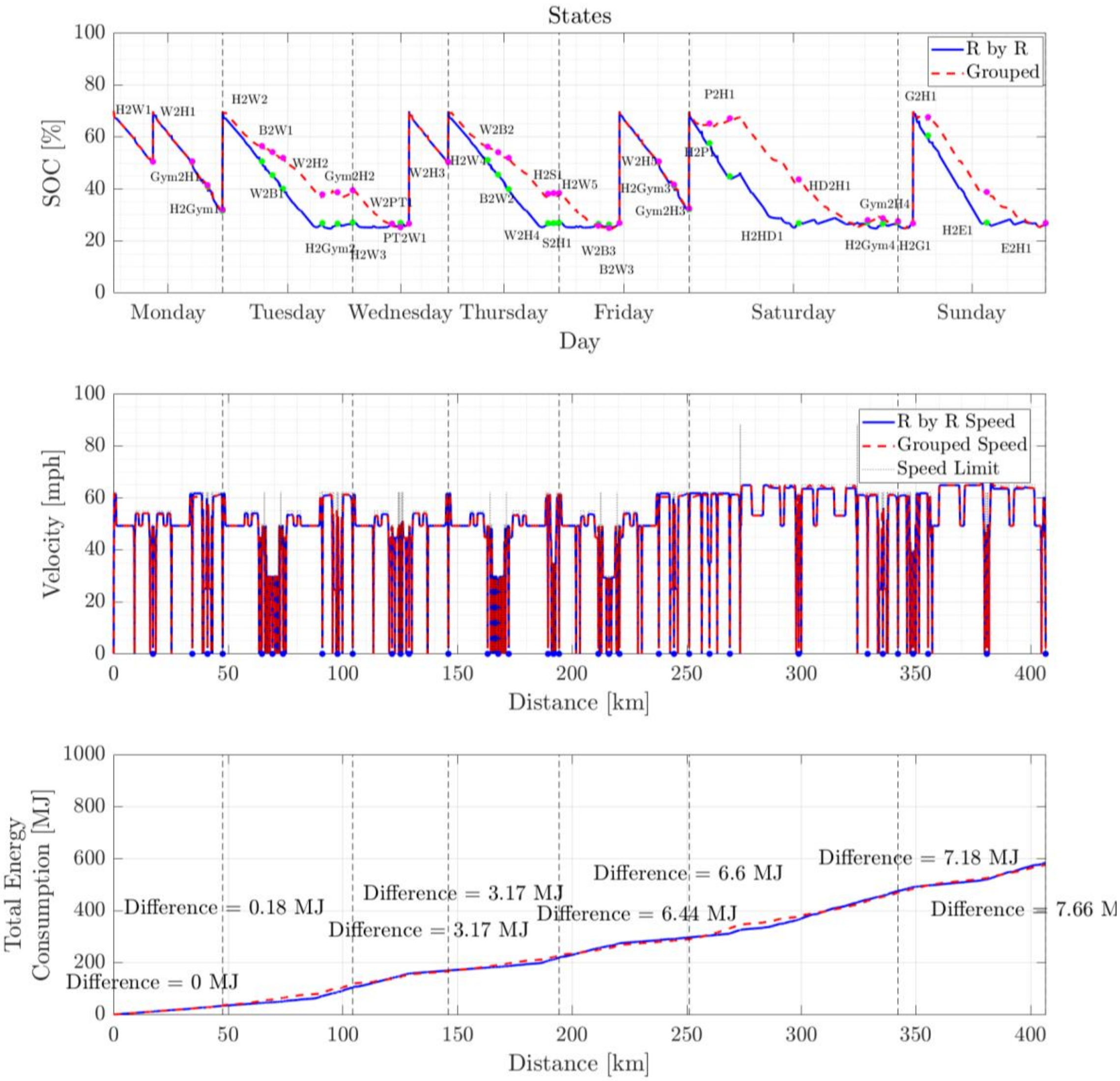

Figure A.2: Variation 22 Results

Table A.2: Variation 22 Summary

Variation 22	Total Energy Consumed [MJ]		Travel Time [s]		Ending SoC [%]	
	R by R	Grouped	R by R	Grouped	R by R	Grouped
From Start of Week to Charge 1	11.6	11.6	793	793	50.5	50.5
From Charge 1 to Charge 2	21.9	21.7	1489	1490	31.7	32.1
From Charge 2 to Charge 3	124.4	121.4	4262	4243	26.7	26.7
From Charge 3 to Charge 4	11.6	11.6	803	803	50.4	50.4
From Charge 4 to Charge 5	105.2	101.9	4099	4088	26.9	26.9
From Charge 5 to Charge 6	21.8	21.6	1459	1460	32.2	32.5
From Charge 6 to Charge 7	194.4	193.8	4105	4082	26.7	26.8
From Charge 7 to End of Week	93.2	92.7	2357	2351	26.9	26.9

Appendix B: Large Scale Extended Study Results

Additional graphs representing the extended study have been generated and support the arguments made in Chapter 5. The weekly battery energy in Figure B.1 and the fuel consumption in Figure B.2 both agree with the trend shown for the realistic charging behaviors in Figure 5.3 and Figure 5.4. Both battery energy and fuel consumption converge around 32 charges per week.

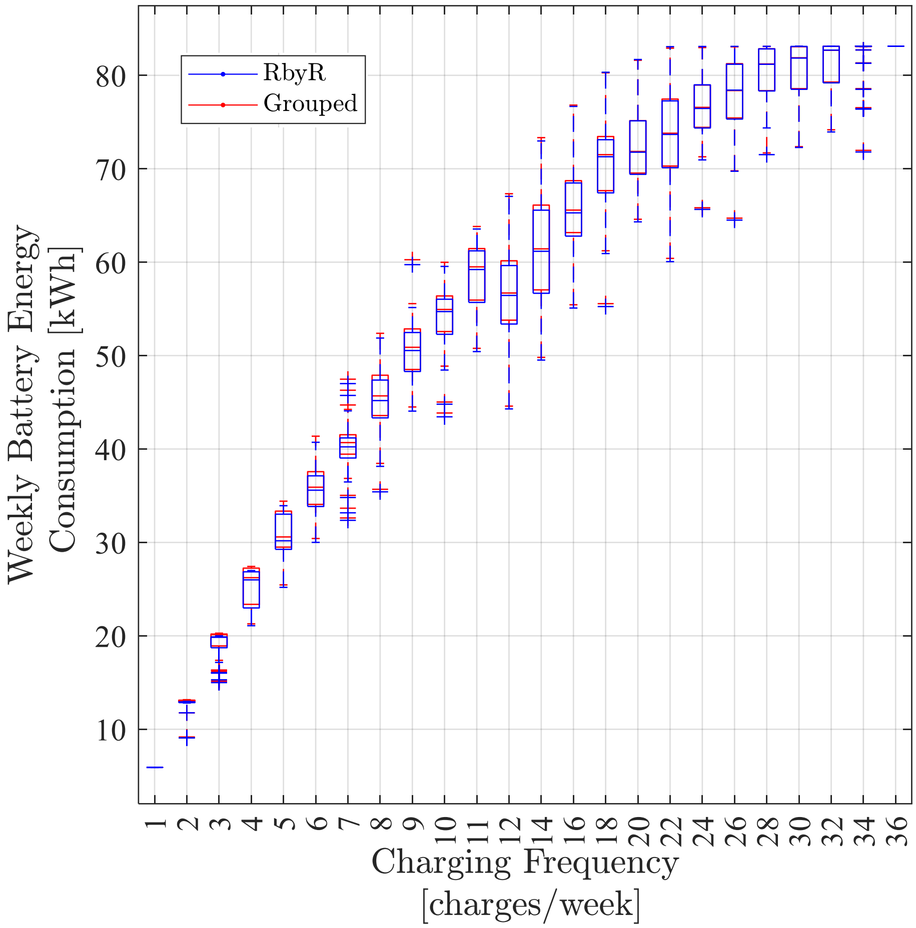

Figure B.1: Weekly Battery Energy Consumption

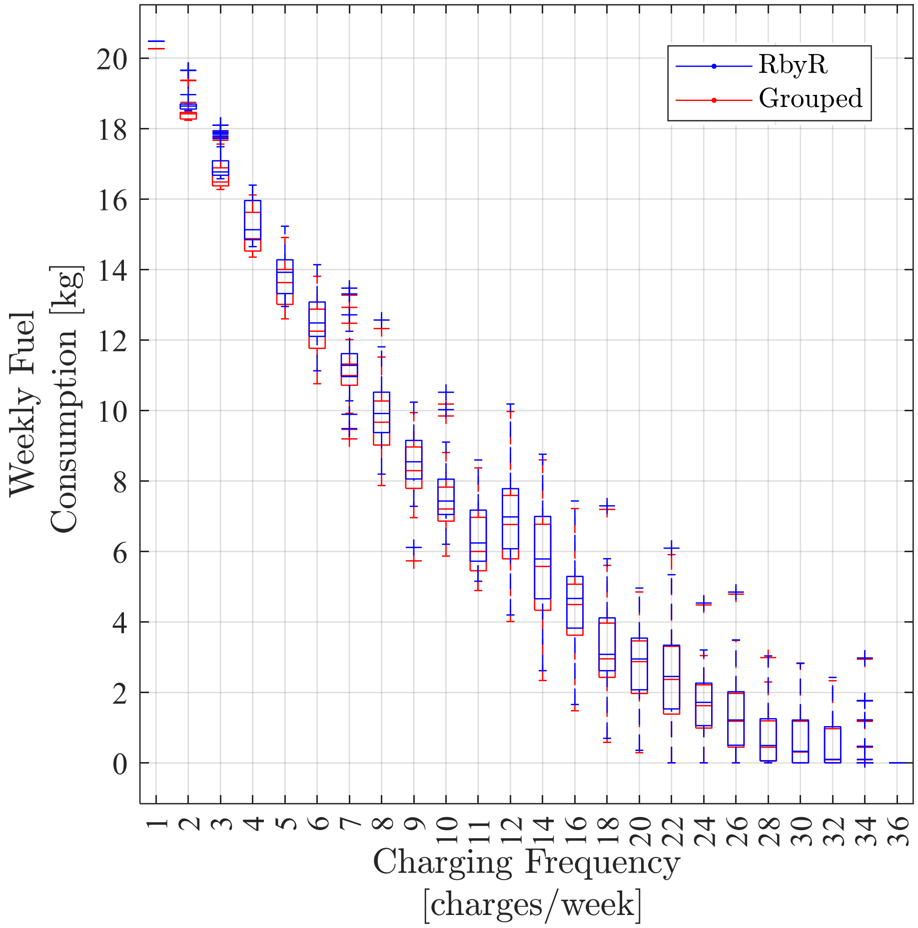

Figure B.2: Weekly Fuel Consumption

In Figure B.3, the allocation of charging events is represented by the standard deviation of the distances in between charging events for each variation. If the standard deviation for a weekly variation is very small, the charging events are more evenly spaced. A variation with a high standard deviation has an uneven allocation of charging events. It is important to note that more evenly spaced charging events are also correlated with a higher charging frequency. The exponential trend implies that a higher utility factor corresponds to more evenly spaced charging events. There is a large spread in the middle of the plot, where a standard deviation of 50 km could indicate a utility factor of anywhere between 15-65%. The charging frequency is the driving factor in whether a driver operates at the lower bound or higher bound. This is because a higher charging frequency for a similar standard deviation has more instances of shorter regions between charging events.

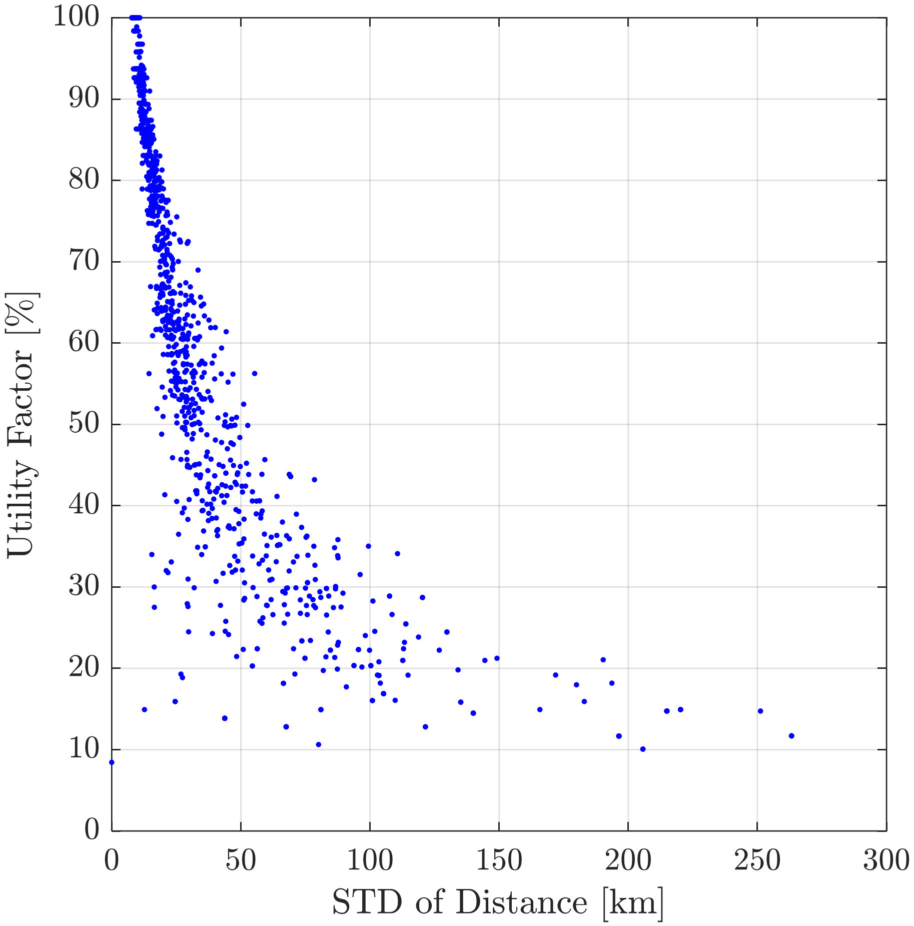

Figure B.3: Effect of Charging Allocation on the Utility Factor